Title
Cluster Observations with the South Pole Telescope

Author
Plagge, Thomas Jeffrey

Publication Date
2009

Cluster Observations with the South Pole Telescope

by

Thomas Jeffrey Plagge

A dissertation submitted in partial satisfaction
of the requirements for the degree of

Doctor of Philosophy

in

Physics

in the

Graduate Division

of the

University of California, Berkeley

Committee in charge:

Professor William Holzapfel, Chair
Professor Steven Boggs
Professor Chung-Pei Ma

Fall 2009

The dissertation of Thomas Jeffrey Plagge is approved.

Chair Date

Date

Date

University of California, Berkeley

Fall 2009

Cluster Observations with the South Pole Telescope

by

Thomas Jeffrey Plagge

Abstract

Cluster Observations with the South Pole Telescope

by

Thomas Jeffrey Plagge

Doctor of Philosophy in Physics

University of California, Berkeley

Professor William Holzapfel, Chair

The South Pole Telescope (SPT) is an instrument designed to survey galaxy clusters using the Sunyaev-Zel'dovich effect. In this thesis I describe the telescope, its first-generation receiver, and its readout and control systems. I also present Sunyaev-Zel'dovich measurements of 15 massive X-ray selected galaxy clusters obtained with the SPT. The cluster signals are measured at 150 GHz, and concurrent 220 GHz data are used to reduce astrophysical contamination. Radial profiles are computed using a technique that takes into account the effects of the beams and filtering. In several clusters, significant SZ decrements are detected out to a substantial fraction of the virial radius. The profiles are fit to the β-model and to a generalized NFW pressure profile, and are scaled and stacked to probe their average behavior. The best-fit model parameters are consistent with previous studies: $\beta = 0.86$ and $r_{\rm core}/r_{500} = 0.20$ for the β-model, and $(\alpha_{\rm n}, \beta_{\rm n}, \gamma_{\rm n}, c_{500})$=$(1.0, 5.5, 0.5, 1.0)$ for the generalized NFW model. Both models fit the SPT data comparably well, and both are consistent with the average SZ profile out to the virial radius. The integrated Compton-y parameter Y_{SZ} is computed for each cluster using both model-dependent and model-independent techniques, and the results are compared to X-ray estimates of cluster parameters. Y_{SZ} is found to scale with Y_X and gas mass with low scatter. Since these observables have been found to scale

with total mass, these results point to a tight mass-observable relation for the SPT cluster survey.

To Heather, without whose encouragement and patience this would not have been possible.

Contents

List of Figures

List of Tables

Acknowledgements

This thesis would not have been possible without the love and support of my wife Heather, nor without the guidance of my parents.

I have been privileged to work with an impressive group of people at Berkeley, starting with my advisor Bill Holzapfel. It was from him, along with past and present postdocs Bradford Benson, Nils Halverson, Matt Dobbs, and Christian Reichardt, that I learned virtually everything I know about experimental physics and cosmology. I owe a debt of gratitude to the entire Berkeley group for making graduate school an enjoyable and enriching experience.

The South Pole Telescope collaboration has more than its share of brilliant minds and strong personalities, and it has been a pleasure to be a part of it. I would particularly like to acknowledge John Carlstrom for providing us with the resources to make the experiment possible, and the South Pole crew for three memorable deployments.

Finally, I would like to acknowledge my friend and colleague Huan Tran. He will be missed.

Chapter 1

Introduction

1.1 Overview

Cosmology, the study of the universe at the largest scales, has been a subject of human fascination throughout recorded history. Over the last few decades, advances in observational techniques have allowed the composition, structure, and history of the universe to be studied quantitatively. Remarkably, a simple model has emerged that is consistent with all observed phenomena.

The standard cosmological model describes a universe with a flat Euclidean geometry. It began in a state of high density and temperature, from which it expanded exponentially during a period of inflation, in the process acquiring small inhomogeneities that became the seeds for structure formation. At the end of the inflationary era, the universe remained hot and dense, with baryonic matter[1] ionized and tightly coupled to radiation in a baryon-photon plasma. As the universe continued to expand and cool, the matter and radiation underwent oscillations as gravitational attraction toward overdense regions competed with radiation pressure. After about 400,000 years, the universe had cooled to 3000 K, at which point neutral matter was able to form and persist. This broke the coupling between the matter and radiation, allowing the radiation to stream freely through the universe, and the matter to form structure like stars and galaxies.

The universe is still expanding and cooling today—in fact, the expansion is accelerating, fueled by a hypothesized form of energy called "dark energy." The simplest conception of dark energy consistent with observations was proposed by Einstein, in the form of a vacuum energy density that enters the field equations of general relativity as a constant term Λ. He later repudiated this idea, but surprising data gathered in recent years suggest that he did so in error. Observational evidence also strongly suggests the existance of an unseen form of matter—cold dark matter (CDM)—that interacts via gravity but not via the electromagnetic or strong nuclear forces. Both dark matter and dark energy play a central role in the standard, or ΛCDM, cosmological model.

Evidence for this model comes from a variety of sources:

- Light element abundances largely comport with models of big bang nucleosynthesis.

---

[1] Cosmologists use this term to refer to all non-relativistic "normal matter" like protons and electrons.

- Light curves from Type Ia supernovae can be used to infer the evolution of the expansion rate of the universe, with results that are consistent with a ΛCDM cosmology.

- Large-scale galaxy and galaxy cluster surveys can be used to test models of structure growth, which depend strongly on cosmology. Once again, the results match expectations.

- The Cosmic Microwave Background (CMB), a nearly uniform bath of photons that has pervaded the universe since matter and radiation decoupled, is essentially a snapshot of the early universe. This radiation has small but measureable anisotropies, and the ΛCDM model makes specific predictions about the form that they should take. Competing cosmologies, such as those in which the universe persists in a steady state or in which structure is generated in other ways, would result in a CMB that looked vastly different if it existed at all. Measurements have consistently favored the standard model.

Within the ΛCDM framework, however, there remain a number of open questions. In particular, the nature of dark energy remains a mystery, and its behavior is not strongly constrained by existing data. Increasingly precise measurements of the CMB provide one path forward.

1.2 Historical Context

Nearly twenty years after its prediction [Gamow, 1946], the CMB was discovered serendipitously by Penzias and Wilson [Penzias and Wilson, 1965], who estimated its temperature to be approximately 3.5 K. A long campaign to measure its spectrum ensued [Woody and Richards, 1979, for example], culminating with with the Far-Infrared Absolute Spectrophotometer (FIRAS) instrument on the Cosmic Background Explorer (COBE) satellite, which measured a spectrum consistent with that of a black body at $T_{\mathrm{CMB}} = 2.725 \pm 0.002$ K [Mather et al., 1999] (see Figure 1.1). The agreement is so precise that the CMB is believed to have the most perfect blackbody spectrum in nature.

Disregarding the dipole moment due to the motion of the earth relative to the CMB reference frame, temperature anisotropies in the CMB are at the level of one part in 10^5. Measuring such a tiny signal requires a sensitive instrument with tight control over systematic errors. Once again, an instrument on the COBE satellite—the Differential Microwave Radiometer (DMR)—was the first to make a definitive measurement, detecting anisotropies across the sky down to angular scales of $\sim 7°$ [Smoot et al., 1992].

Variance in the CMB at the large angular scales probed by the DMR arose from primordial inhomogeneities; at smaller angular scales, the dynamics of the baryon-photon plasma led to anisotropies with a structure that depends strongly on several cosmological parameters. Measurements at degree and sub-degree scales can be performed by instruments with less sky coverage than COBE, and a number of groups took up the challenge. The instruments they used fell into two general classes: coherent receivers, which respond to electric field strength and require low-noise amplifiers such as those based on high electron mobility transistors

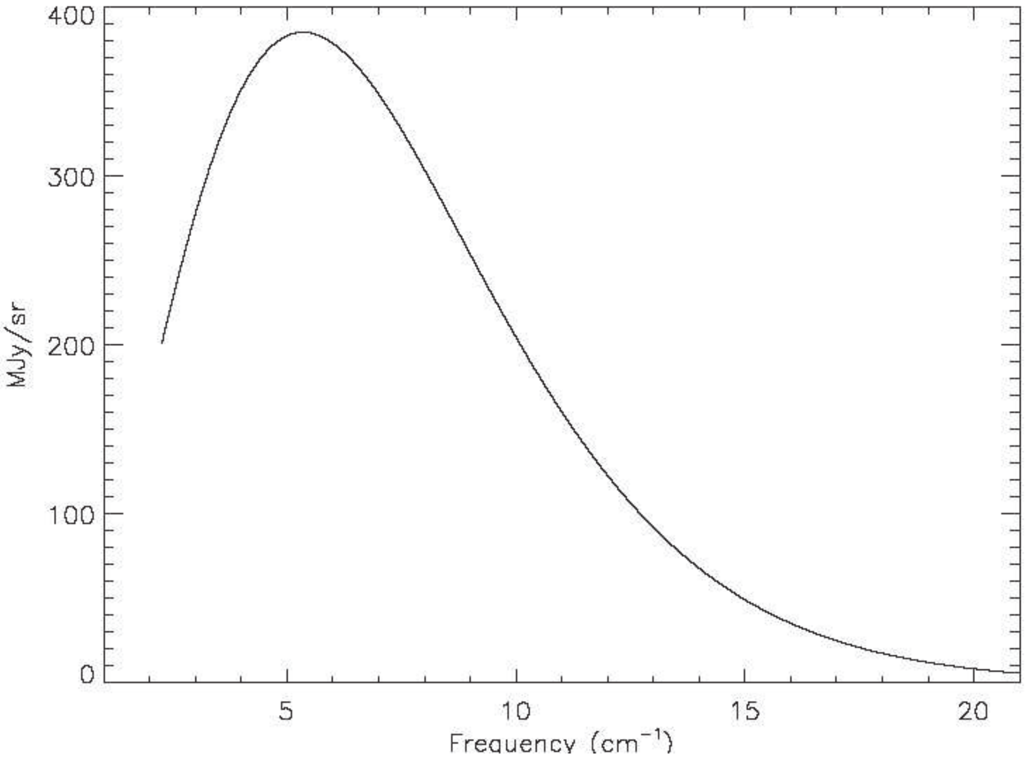

Figure 1.1. CMB emission spectrum and fit to blackbody spectrum, from the FIRAS instrument on the COBE satellite. Uncertainties are a fraction of the line width [Fixsen et al., 1996].

(HEMTs); and incoherent receivers, which measure incident power and require sensitive detectors such as bolometers (discussed in Chapter 4). In the early part of this decade, two balloon-borne bolometric instruments (MAXIMA [Hanany et al., 2000, Lee et al., 2001] and BOOMERANG [Netterfield et al., 2002]) and a ground-based interferometer (DASI [Halverson et al., 2002]) measured anisotropies at degree scales. Subsequently, another satellite mission (the Wilkinson Microwave Anisotropy Probe (WMAP) [Hinshaw et al., 2003, 2009]) made pristine measurements down to tens of arcminutes, while two ground-based instruments (bolometer-based ACBAR [Kuo et al., 2004, Reichardt et al., 2009] and HEMT-based CBI [Padin et al., 2001, Mason et al., 2003]) pushed down to still smaller angular scales.

The CMB temperature anisotropies with origins in the early universe—the so-called primary anisotropies—have now been measured in exquisite detail. Further efforts are underway to probe the polarization of the CMB, which was first detected by DASI [Kovac et al., 2002] and has now been measured by a number of instruments [Pryke and the QUaD Collaboration, 2009, Page et al., 2007, Chiang et al., 2009]. Attention has also been focused on secondary temperature anisotropies, those which originated after the decoupling of matter and radiation. Since both incoherent and coherent detectors are approaching their fundamental sensitivity limits, a new generation of instruments has emerged to tackle these increasingly challenging measurements. A common approach has been to employ large arrays of bolometric detectors, which increases the efficiency with which the CMB can be mapped while building on existing technology. The South Pole Telescope (SPT) is one such instrument. First deployed to the geographic South Pole in the austral summer of 2006-2007, the SPT has now gathered almost three years of data, with the primary goal of identifying and studying galaxy clusters via their effect on the CMB.

1.3 Thesis Outline

In Chapter 2, I will provide an overview of the standard cosmological model, and will discuss the motivation for studying clusters by way of the CMB. Chapter 3 will describe the SPT instrument, focusing in particular on optics and cryogenics. The dectector array will be discussed in Chapter 4, and the multiplexed readout system in Chapter 5. Chapter 6 will cover operational aspects of the instrument, and on the software developed to control and monitor the receiver and readout. Finally, Chapter 7 will describe in detail the analysis of a series of targeted cluster observations performed by the SPT in the austral winter of 2008.

1.4 Personal Contributions

The SPT was developed over many years by a large team of individuals. Some aspects of the experiment that I will include in this thesis are ones to which I did not directly contribute, but which are necessary to discuss in order to provide a coherent description of the project. The work that I contributed to the SPT includes the development of significant portions of the readout and control software, the testing and characterization of the bolometers and receiver cryostat, and the tuning and optimization of the instrument on the sky. I also assisted in the development of the data analysis pipeline, undertook a study of the targeted cluster observations discussed in Chapter 7, and assisted in three deployments to the South Pole.

I also worked on various aspects of the APEX-SZ experiment, a pathfinder instrument for the SPT and a powerful CMB receiver in its own right; much of this work applied directly or indirectly to the SPT. I designed portions of the APEX-SZ receiver cryostat and optics, assisted in the design and characterization of its cryogenic system, worked on many aspects of the multiplexed readout electronics and software, and helped to characterize and optimize the detector arrays. I also assisted in the deployment of the instrument for its initial engineering run. I will not seperately describe the APEX-SZ experiment, but when appropriate, I will discuss some of my work as it relates to the SPT.

Chapter 2

Cosmology

In this chapter, I will provide a broad overview of the standard cosmological model. I will then discuss galaxy clusters—the largest gravitationally bound objects in the universe—and a method of measuring them using anisotropies in the Cosmic Microwave Background. Finally, I will discuss ways in which such measurements can be used to extend our knowledge of cluster physics and cosmology.

2.1 The Standard Cosmological Model

The physics of the universe on large scales is described by the ΛCDM model, which was briefly discussed in Chapter 1. This model is part of a class of cosmologies which take as their starting point the Cosmological Principle: the universe must be homogeneous and isotropic on large scales. Observational evidence strongly suggests that this is indeed the case. From this starting point, one can derive the Friedmann equations, which describe the dynamics of a universe comprised of a perfect fluid. The inhomogeneities that give rise to the structure we see today can then be treated in the context of the expanding universe described by this formalism.

2.1.1 The Friedmann Equations

The Friedmann equations are derived from the Einstein field equations of General Relativity, which relate the energy-momentum tensor to the spacetime metric. In a homogeneous and isotropic universe, the energy-momentum tensor is that of a perfect fluid with energy density ρ and pressure p, and the metric is that of Friedmann-Robertson-Walker (FRW):

$$ds^2 = -dt^2 + a^2(t)\left(\frac{dr^2}{1-kr^2} + r^2 d\theta^2 + r^2\sin^2(\theta)d\phi^2\right) \tag{2.1}$$

where ds is the space-time interval, dt is the time interval, (r, θ, ϕ) are the spherical polar spatial coordinates, k is the curvature parameter, $a(t)$ is the time-dependent scale factor, and the units are chosen such that the speed of light $c = 1$. The curvature parameter sets the geometry of the universe: $k = 0$ corresponds with a Euclidean or flat geometry, $k < 0$ with a hyperbolic or open geometry, and $k > 0$ with a spherical or closed geometry. The scale factor $a(t)$ encodes the expansion or contraction of the universe, with increasing values corresponding to expansion.

When the energy-momentum tensor and the metric take these forms, the ten Einstein field equations simplify to the Friedmann equations:

$$\left(\frac{\dot{a}}{a}\right)^2 = \frac{8\pi G}{3}\rho - \frac{k}{a^2} + \frac{\Lambda}{3} \tag{2.2}$$

$$\frac{\ddot{a}}{a} = -\frac{4\pi G}{3}\left(\rho + 3p\right) + \frac{\Lambda}{3} \tag{2.3}$$

where a dot denotes a derivative with respect to t, G is the gravitational constant, and Λ is the cosmological constant. Note that there exists a critical density, $\rho_{\rm cr} \equiv 3(\dot{a}/a)^2/8\pi G$, for which $k = 0$ in a $\Lambda = 0$ universe.

The clear implication of these equations is that the universe can expand and contract. Einstein was originally motivated to introduce the cosmological constant by his belief that the universe should be static. A few years after he made this proposal, however, astronomer Edwin Hubble made a discovery that caused Einstein reconsider [Hubble, 1929]. Using measurements of distance and redshift $z = (1-a)/a$ for a sample of galaxies, Hubble showed that galaxies were (on average) receeding at a rate proportional to their distance from us. The proportionality constant H between velocity and distance, known as the Hubble parameter, is related to the scale factor by $H = \dot{a}/a$. Evaluated at the present time t_0, it is given by $H_0 = 100h$ km/s/Mpc where $h = 0.719^{+.026}_{-.027}$ [Komatsu et al., 2009]. As the Friedmann equations show, H can change as a function of time depending upon the geometry and energy content of the univese.

Radiation and Matter

The energy density term ρ in the Friedmann equations includes contributions from both nonrelativistic and relativistic matter. In the ΛCDM model, only a small portion of the nonrelativistic matter density is made up of normal matter such as protons and electrons; the remainder is made up of CDM, particles that interact gravitationally but not electromagnetically. While the composition of CDM remains unknown, observational evidence for its existence is very strong, and its behavior is well-understood. The matter density is often expressed in terms of the critical density as $\Omega_m \equiv \rho_m/\rho_{\rm cr}$. The relativistic matter density, primarily comprised of photons and neutrinos, is expressed analogously as Ω_r.

In a flat universe with $\Lambda = 0$, the first Friedmann equation can be solved trivially if one form of energy dominates over the others. Nonrelativistic matter density is inversely proportional to volume, and thus scales as a^{-3}. Radiation density, which is inversely proportional to wavelength as well as volume, scales as a^{-4}. In the early universe, when a was very small, the energy density of the universe was dominated by radiation; thus the expansion rate was approximately given by $a \propto t^{1/2}$. Expansion gradually redshifted the radiation, eventually causing matter to take over, at which point $a \propto t^{2/3}$. As the universe further expanded, the matter density dropped below that due to Λ, and we entered the era of dark energy domination.

Dark Energy

Hubble's discovery that the universe was expanding caused Einstein to abandon the cosmological constant, but it staged a surprising comeback in the latter part of the last decade. Two groups working in parallel essentially redid Hubble's experiment, but using Type Ia supernovae instead of galaxies. These supernovae can be observed out to great distances, and have peak absolute magnitudes that are approximately constant. Therefore, by measuring their light curves and inferring their peak brightness, Riess et al. [1998] and Perlmutter et al. [1999] were able to extend the distance-redshift relation and measure a long stretch of the universe's expansion history. Their results showed that the expansion of the universe is accelerating, implying that of some "dark energy" must be driving the expansion.

This discovery dovetailed nicely with theoretical and observational indications that the universe should have a flat $k = 0$ geometry. Since the combined density of radiation and matter $\Omega_r + \Omega_m$ is much smaller than one, some additional unseen energy is necessary to form a coherent picture. A cosmological constant Λ with a density such that $\Omega_r + \Omega_m + \Omega_\Lambda = 1$ is the simplest form of dark energy that fits the evidence.

More complicated forms, however, have not been ruled out. One way of characterizing the behavior of dark energy is by its equation of state, which relates its pressure to its energy density via $p = w\rho$. For relativistic and nonrelativistic matter, $w = 1/3$ and 0, respectively. Dark energy has the unique property that the pressure it exerts is negative. For a cosmological constant, $w = -1$, while other forms can have different equations of state—w need not even be a constant with respect to time. One of the major ongoing efforts in observational cosmology is to constrain w and discern the nature of dark energy.

2.1.2 Inhomogeneities

The dark energy-dominated era is not the first in which the universe has undergone accelerating expansion. The theory of inflation suggests that a small region of the early universe exponentially expanded by at least 60 e-foldings. This provides a way around a problem with the idea that the universe is homogeneous and isotropic: straightforward calculations indicate that prior to decoupling, light was unable to travel the breadth of the presently-observable universe. Distant regions of space were never in causal contact, so there is no apparent reason why, for example, the CMB should be so uniform. Inflation provides a way around this "horizon problem" by positing a pre-inflation universe where these regions were able to equilibrate. If the region that underwent this expansion were locally flat, then inflation would also resolve the so-called flatness problem of why we live in a universe that seems to be tuned to have $\Omega_r + \Omega_m + \Omega_\Lambda = 1$.

A simple model of inflation invokes a high-temperature scalar field called the inflaton field, which drives the exponential expansion until it decays to form matter and radiation. Quantum fluctuations in this field generate a scale-invariant spectrum of fluctuations in the gravitational potential of the early universe, the seeds of structure formation. They are still visible today in the form of large-scale anisotropies in the Cosmic Microwave Background.

The Cosmic Microwave Background

In the early universe, normal matter was ionized and tightly coupled to radiation by the electromagnetic interaction. At decoupling, which occurred at $z \sim 1100$, the photon mean free path became long and scattering essentially ceased. The primordial radiation has since been redshifted to microwave frequencies, and is therefore known as the Cosmic Microwave Background (CMB). It is nearly a direct snapshot of the early universe, and is consequently a powerful tool for observational cosmology.

Anisotropies in the CMB are usually quantified in terms of the angular power spectrum. Decomposing the temperature fluctuation field $\Delta T(\hat{\mathbf{n}})$ into its multipole moments

$$T_{\ell m} = \int d\hat{\mathbf{n}} Y^*_{\ell m}(\hat{\mathbf{n}}) T(\hat{\mathbf{n}}), \tag{2.4}$$

where $Y_{\ell m}$ is the (ℓ, m) spherical harmonic, the power spectrum is given by

$$\langle T^*_{\ell m} T_{\ell' m'} \rangle = \delta_{\ell \ell'} \delta_{m m'} C_\ell. \tag{2.5}$$

Note that ℓ is inversely proportional to spatial scale; $\ell \sim 100$ corresponds to degree-scale anisotropies.

Figure 2.1 shows the power spectrum as measured by several recent experiments. The quantity plotted is $\ell(\ell+1)C_\ell/(2\pi)$, in which form anisotropies that correspond to scale-invariant fluctuations—such as those predicted by the self-similar process of exponential inflation—appear as a flat line. The variance at very low ℓ is over scales too large for interactions to have taken place prior to decoupling, and must therefore be a direct result of primordial fluctuations. The most prominent features at intermediate ℓ are the so-called acoustic peaks, which arose from pressure oscillations in the tightly coupled baryon-photon plasma. At the time of decoupling, these oscillations abruptly ceased, leaving some modes at their maximum compression or rarefaction. Excess power is visible on angular scales corresponding to these modes, and the height and scale of these peaks can be used to constrain the geometry and composition of the early universe. At high ℓ, where the spatial scales become comparable to the damping scale set by the photon mean free path, the acoustic peaks die away.

The power does not go to zero at small angular scales, however, due in part to secondary anisotropies imparted to the CMB after the decoupling time. One important type of secondary anisotropy is due to the Sunyaev-Zel'dovich (SZ) effect, which occurs when CMB photons scatter off hot gas in the potential wells of galaxy clusters, and which is discussed in detail in Section 2.2.

Matter inhomogeneities

Inhomogeneities in the matter distribution also arose from the gravitational potential fluctuations imparted by inflation. Dark matter was unaffected by the physics of the baryon-photon plasma, and immediately began clumping near primordial overdensities, joined by normal matter after decoupling. Once the overdensity in a given region grew large enough for local gravity to overcome the expansion of the universe, the matter in the region underwent gravitational collapse, becoming increasingly compact until it could support itself by angular momentum or pressure. Simulations indicate that CDM, upon undergoing collapse, forms dark matter halos with a universal density profile that can be modelled as

$$\rho(r) = \frac{\rho_0}{\frac{r}{r_s}\left(1 + \frac{r}{r_s}\right)^2}, \tag{2.6}$$

the NFW profile [Navarro et al., 1996]. In the ΛCDM model, structure is formed hierarchically: smaller dark matter halos form first, and gradually merge to form larger ones.

On large scales, structure growth remains linear, and so the spectrum of inhomogeneities on these scales remains Gaussian and is characterized by its power spectrum. Knowledge of the initial spectrum and its normalization, and of the linear evolution of the gravitational potential, are sufficient to determine the present-day structure of these inhomogeneities. On smaller scales, structures virialize and the process becomes non-linear. The dividing line between linear and non-linear structure growth is at scales of ~ 10 Mpc. Galaxy clusters, which are megaparsecs in extent, are thus the largest and most recently formed virialized objects in the universe.

For this reason, the distribution of clusters depends very little on the complex physics of gas dynamics and feedback, and is instead determined by gravitational processes. One approximate approach to predicting the distribution of clusters is that of Press and Schechter [Press and Schechter, 1974], in which the purely linear density function is smoothed at various scales to flag regions dense enough to undergo collapse. The Press-Schechter formula gives the number density of clusters of mass M at redshift z as

$$\frac{dn}{dM}(z, M) = \sqrt{\frac{2}{\pi}}\frac{\rho_0}{M}\frac{\delta_c}{D_z\sigma_M^2}\frac{d\sigma_M}{dM}\exp\left(\frac{-\delta_c^2}{2D_z^2\sigma_M^2}\right), \tag{2.7}$$

where ρ_0 is the present-day density, D_z is a function that determines the linear growth of structure, $\delta_c \sim 1.68$ is the overdensity threshold (so that regions with $\rho > \delta_c\rho_0$ are considered collapsed), and σ_M is the r.m.s. density fluctuation at mass M in the present-day linear power spectrum. This somewhat ad-hoc distribution function is found to be roughly consistent with the results of n-body simulations, and is very widely used.

Galaxy cluster surveys generally seek to identify objects within some solid angle Ω which have masses greater than $M_{min}(z)$. The observable quantity is thus

$$\frac{dN}{dzd\Omega}(z) = \left(\frac{dV}{dzd\Omega}(z)\int_{M_{min}(z)}^{\infty} dM\frac{dn}{dM}\right). \tag{2.8}$$

The volume element $dV/dzd\Omega$ depends upon the expansion of the universe, while dn/dM depends on the growth of structure. This makes the abundance of clusters another useful probe of cosmology, which can be used as both a cross-check and a way of breaking degeneracies in cosmological models.

2.2 Galaxy Clusters and the Sunyaev-Zel'dovich Effect

2.2.1 Galaxy Clusters

Galaxy clusters formed relatively recently on cosmological scales, generally at redshifts less than 3. Typical clusters have radii of order 1 MPc and masses of 10^{14} to 10^{15} times the mass of the sun $M_\odot$. The bulk of the mass is in the form of dark matter; the stars in the 50 to 1000 constituent galaxies contribute of order 1% of the mass, while another $\sim 10\%$ is comprised of intergalactic gas known as the intracluster medium (ICM). The gas in the ICM is heated to temperatures of 10^7-10^8 Kelvin, or $k_BT \sim 1 - 10$ keV, and thus emits X-rays via bremsstrahlung.

Clusters can be observed in a variety of different ways. In the X-ray band, a cluster appears as a bright source with a flux given by

$$S_X = \frac{1}{4\pi(1+z)^4} \int n_e^2 \Lambda_{ee} dl, \tag{2.9}$$

where n_e is the electron density of the ICM, Λ_{ee} is the X-ray cooling function, and the integral is along the line of sight. X-ray spectra also yield estimates of the temperature and metallicity (the proportion of heavy elements) of the ICM. In the optical and infrared bands, a cluster appears as a concentration of galaxies. Redshifts can be estimated using spectroscopic or photometric techniques, and masses can be inferred using the velocity dispersion of the member galaxies. Optical and infrared measurements of background galaxies can be used to probe the total mass of clusters (including dark matter), since the deep potential well of the cluster acts as a gravitational lens. Each of these techniques has its own challenges and limitations, and data gathered from a variety of sources provides the most complete picture.

The CMB provides yet another powerful and complementary way of studying clusters. Since the ICM is heated to high temperatures, a CMB photon scattering off an ICM electron will be upscattered in energy by $\Delta E/E = k_BT/m_ec^2 \sim 10^{-2}$. The optical depth of the ICM is $\tau = n_e\sigma_T R \sim 10^{-2}$, where n_e is the electron number density, σ_T the Thomson cross section, and R the effective radius. Therefore, approximately 1% of the CMB photons incident upon a cluster will be upscattered in energy by 1%. This results in an overall change in the CMB brightness temperature in the direction of the cluster by about one part in 10^4, in a process known as the Sunyaev-Zel'dovich Effect [Sunyaev and Zeldovich, 1970a,b].

2.2.2 The Sunyaev-Zel'dovich Effect

The physics of the Sunyaev-Zel'dovich (SZ) effect are described in detail in a number of works; here I follow the treatment of Birkinshaw [1999].

The scattering of a photon with energy E by an electron at rest is described by the Compton scattering formula:

$$E' = \frac{E}{1 + \frac{E}{m_e}} \left(1 - \cos\Delta\theta\right), \tag{2.10}$$

where m_e is the electron mass, where $\Delta\theta$ is the angle by which the photon is deflected, and where we again adopt units where $c = 1$. We wish to determine the effect of this scattering on the frequency of the CMB photons. In the limit appropriate for ICM electrons, the probability of a scattering at incident angle θ is given by

$$P_\theta(\theta) d\cos\theta = \left(2\gamma^4(1 - v_e\cos\theta)^3\right)^{-1} d\cos\theta, \tag{2.11}$$

where v_e is the final electron velocity and $\gamma = (1 - v_e^2)^{-1/2}$. The probability of a photon scattering from θ to θ' is

$$P_{\theta'}(\theta'|\theta) d\cos\theta' = \frac{3}{8}\left(1 + \cos^2\theta\cos^2\theta' + \frac{1}{2}(1 - \cos^2\theta)(1 - \cos^2\theta')\right) d\cos\theta', \tag{2.12}$$

causing the scattered photon to appear with frequency

$$\nu' = \nu(1 + v_e\cos\theta')(1 - v_e\cos\theta)^{-1}. \tag{2.13}$$

The probability of a resulting logarithmic frequency shift $s = \log(\nu'/\nu)$ given v_e is then

$$P_s(s|v_e) = \int P_\theta(\theta) d\cos\theta P_{\theta'}(\theta'|\theta)\frac{d\cos\theta'}{ds} ds, \tag{2.14}$$

where P_θ and $P_{\theta'}$ are given above, and where $\cos\theta' = (e^s(1 - v_e\cos\theta) - 1)/(v_e)$.

This gives us the frequency shift of the incident photons once we know the distribution of the electron velocities. In the ICM, the velocities in the rest frame of the cluster are distributed according to the relativistic Maxwell distribution with temperature T_e,

$$P_{v_e}(v_e)dv_e = \frac{\gamma^5 v_e^2 e^{-\gamma m_e/k_B T_e} dv_e}{(k_B T_e/m_e)K_2(m_e/k_B T_e)}, \tag{2.15}$$

where K_2 is the second order modified Bessel function of the second kind and k_B is the Boltzmann constant. The spectral shift due to this thermal component of the electron velocities is referred to as the thermal SZ effect. The probability of a logarithmic frequency shift s from a single scattering P_1 can be found by integrating $P_s P_{v_e}$ over velocity, and the probability of s due to multiple scatterings can be found by repeated convolution of P_1. Along with knowledge of the CMB frequency spectrum, these tedious calculations yield the form of the spectral distortion due to the thermal SZ effect.

In order to get a more intuitive sense of the effect, it is useful to consider the scattering process in the non-relativistic limit, and to add in a correction factor after the fact. The process can then be described by the Kompaneets equation:

$$\frac{\partial n}{\partial y} = \frac{1}{x^2}\frac{\partial}{\partial x}\left(x^4\left(\frac{\partial n}{\partial x} + n + n^2\right)\right), \tag{2.16}$$

where $n(\nu)$ is the occupation number at frequency ν, x is the dimensionless frequency given by

$$x = \frac{h\nu}{k_B T_e}, \tag{2.17}$$

h is the Planck constant, and y is the Comptonization parameter or Compton-y. The Comptonization for radiation passing through a cloud of electrons is given by

$$y = \int n_e \sigma_T \frac{k_B T_e}{m_e} dl, \tag{2.18}$$

where σ_T is the Thompson cross-section, n_e is the electron number density, and the integral is along the line of sight.

If $h\nu << k_B T_e$, which is the case for CMB photons and ICM electrons, then x is small and Equation 2.16 simplifies further to

$$\frac{\partial n}{\partial y} = \frac{1}{x^2}\frac{\partial}{\partial x}x^4\frac{\partial n}{\partial x}. \tag{2.19}$$

In this case, the change in the CMB occupation number takes a particularly simple form:

$$\Delta n = xy\frac{e^x}{(e^x-1)^2}\left(x\coth(x/2)-4\right), \tag{2.20}$$

and the change in intensity at dimensionless frequency x is given by $\Delta I/I_0 = x^3\Delta n(x)$. This is the widely-used non-relativistic formula for the thermal SZ spectrum. Note that in contrast to the X-ray flux, the redshift of the cluster does not enter into this equation: the SZ effect is independent of redshift, and can thus be used to measure galaxy clusters out to the epoch of their intial formation.

The spectral distortion due to the SZ effect is shown in Figure 2.2. At ~ 218 GHz, the change in intensity is zero. At higher frequencies, in the Wein tail of the CMB black body spectrum, the intensity is increased. At lower frequencies, in the Rayleigh-Jeans region of the spectrum, the SZ effect manifests itself as a decrement in intensity due to lower-energy photons getting upscattered into the Wein tail. The amplitude of the distortion depends on the Comptonization, and is thus a measure of the integrated pressure along the line of sight.

For large, hot clusters, the amplitude of the SZ signal can be comparable to, or even larger than, primary CMB anisotropies in amplitude. Their characteristic spatial scale, however, is much smaller: ~ 1 arcminute, versus about $0.5°$ for the largest CMB acoustic peak.

This treatment of the SZ effect neglects some important features. First, as mentioned above, the Kompaneets equation is non-relativistic. Relativistic effects can be of order 10% for particularly high electron temperatures; an approximate correction factor is provided by Itoh et al. [2000]. It is observationally convenient to express the thermal SZ effect as a change in the CMB temperature T_{CMB}:

$$\frac{\Delta T}{T_{\mathrm{CMB}}} = f(x)y, \tag{2.21}$$

where $f(x)$ is the frequency dependence derived above plus the relativistic correction δ_{SZ}:

$$f(x) = \left(x\frac{e^x+1}{e^x-1}-4\right)(1+\delta_{SZ}(x,T_e)). \tag{2.22}$$

Non-thermal electron velocities can also lead to measurable effects. The kinetic SZ effect, which results from bulk electron velocities relative to the CMB reference frame, imparts a temperature change to the CMB given by

$$\frac{\Delta T}{T_{\mathrm{CMB}}} \sim -\tau_e\frac{v_{\mathrm{pec}}}{c}, \tag{2.23}$$

where v_{pec} is the electron peculiar velocity (the non-Hubble component of the line-of-sight velocity) and $\tau_e = \int n_e\sigma_T dl$ is the optical depth. In most frequency bands, the kinetic effect is much smaller for typical values of the optical depth and the peculiar velocity (< 1000 km/sec). The kinetic effect also lacks the distinctive spectral signature of the thermal effect, making it difficult to separate from primary CMB anisotropy signals. However, at frequencies near the $\sim$ 218 GHz thermal SZ null, it may be possible to detect the effect if competing signals can be removed successfully.

2.3 Cosmology and Cluster Physics with the SZ Effect

In combination with other observables such as X-ray flux, SZ measurements can be used to explore the structure and composition of the ICM. Moreover, dependency of the distribution of clusters upon cosmology can be used to place constraints on models, and in particular on the behavior of dark energy.

2.3.1 The Structure of the ICM

The thermal SZ effect probes the integrated pressure of the electron gas, $\propto n_e T_e$. Since X-ray flux goes as $n_e^2 \Lambda_{ee}$, X-ray and SZ data are complementary, and can be combined to separately measure the density and temperature. The density profiles of the ICM for different galaxy clusters are expected to be approximately self-similar. If the dark matter distribution is given by the NFW profile (Equation 2.6), Navarro et al. [1996] find that the ICM in hydrostatic equilibrium has a profile that can be approximated by the isothermal $\beta-$model [Cavaliere and Fusco-Femiano, 1976, Cavaliere and Fusco-Femiano, 1978], which parameterizes the 3-dimensional electron number density as

$$n_e(\boldsymbol{r}) = n_{\mathrm{e}_0} \left(1 + \frac{r^2}{r_{\mathrm{core}}^2}\right)^{3\beta/2}, \tag{2.24}$$

where n_{e} is the electron number density, n_{e_0} is the number density at the cluster center, r is the radius from the cluster center, r_{core} is the core radius of the gas distribution, and β is the power law index at large radii.

X-ray and/or SZ measurements can be used to find the best-fit $\beta-$model parameters for a given cluster, which can then be integrated to estimate the cluster gas mass M_{gas}. The total mass of the cluster, M_{tot}, can also be found by assuming hydrostatic equilibrium. Alternatively, M_{tot} can be estimated using optical or infrared measurements of gravitational lensing or velocity dispersion. The ratio of M_{gas} to M_{tot} is a lower limit on the ratio of the baryon density to matter density in the universe, and can also be used to constrain dark energy [Rapetti et al., 2008].

Thermal Structure

The use of the $\beta-$model in the SZ context makes the implicit assumption that the ICM is isothermal. Heirarchical structure growth, however, does not cease upon the initial formation of clusters: mergers are common, and generally result in temperature structure such as shocks. Moreover, some clusters—referred to as cooling core clusters—have dense cores with central cooling times significantly smaller than their age, resulting in cooling flows partially balanced by feedback from active galactic nuclei (AGN). Thus the ICM generally is not isothermal, and an accurate model must take this into account.

Nevertheless, much of the work on cluster structure has used the $\beta-$model as a convenient fitting function [e.g., Grego et al., 2000, Reese et al., 2002, Benson et al., 2004, Halverson et al., 2008]. It has the advantage of simplicity: using the density profile from Equation 2.24 and assuming isothermality, Equation 2.21 yields an analytic formula for the SZ decrement,

$$\Delta T_{\rm SZ} = \Delta T_0 \left(1 + \frac{\theta^2}{\theta^2_{\rm core}}\right)^{(1-3\beta)/2}. \tag{2.25}$$

Here θ is the angular distance from the cluster center, given by $\theta = r/D_A$ where D_A is the angular diameter distance (which implicitly defines D_A). ΔT_0 is the central temperature decrement, and $\theta_{\rm core}$ is the angle corresponding to $r_{\rm core}$. Note that the use of the $\beta-$model as a fitting function does not necessarily imply isothermality unless the same values of β and $r_{\rm core}$ are assumed to hold for both density and $\Delta T_{\rm SZ}$. While the $\beta-$model tends to do a decent job of modelling clusters at intermediate radii, measurements and simulations indicate that it breaks down in the cluster core and beyond about r_{2500} (the radius at which the cluster matter density drops to 2500 times the critical density of the universe) [Vikhlinin et al., 2005, Piffaretti et al., 2005].

Nagai et al. [2007] have proposed, and Mroczkowski et al. [2009] have investigated, a generalization of the NFW model that directly parameterizes pressure rather than density:

$$P_{\rm e}(\boldsymbol{r}) = \frac{P_{\rm e_0}}{(r/r_{\rm s})^{\gamma_{\rm n}}\left(1 + (r/r_{\rm s})^{\alpha_{\rm n}}\right)^{(\beta_{\rm n}-\gamma_{\rm n})/\alpha_{\rm n}}}, \tag{2.26}$$

where P_e is the electron pressure; P_{e_0} is the pressure at the cluster center; r is the radius from the cluster center; $r_s = r_{500}/c_{500}$ is a scaling radius set by r_{500}, the radius at which the total cluster density falls to 500 times the critical density of the universe at the cluster redshift, and c_{500}, a parameter characterizing the gas concentration; and $\alpha_{\rm n}$, $\beta_{\rm n}$, and $\gamma_{\rm n}$ set the slope at intermediate ($r \sim r_{\rm s}$), large ($r > r_{\rm s}$), and small ($r < r_{\rm s}$) radii, respectively. The structure parameters $(\alpha_{\rm n}, \beta_{\rm n}, \gamma_{\rm n}, c_{500})$ can be estimated using simulations or measurements; for example, $(0.9, 5.0, 0.4, 1.3)$ are the parameters found to be the best fit to observed *Chandra* X-ray cluster profiles[1]. As the SZ effect is directly proportional to integrated pressure, $\Delta T_{\rm SZ}$ for this model can be found by integrating the above function along the line of sight. Sufficiently sensitive and high-resolution SZ measurements will be able to determine whether this parameterization is more appropriate than the $\beta-$model, and thus whether it can be used to compute more accurate estimates of cluster properties.

2.3.2 SZ Cluster Surveys

The fact that the SZ effect is independent of redshift makes SZ cluster surveys a promising technique for constraining cosmological models. The observable quantity is the differential number density of clusters above a given mass limit $M_{\rm min}$, $dN/dzd\Omega$, defined in Equation 2.8. Since the cluster abundance in the nearby universe is well known, the number density is

---

[1] These values are given in Mroczkowski et al. [2009] as an update of the results in Nagai et al. [2007].

fixed at the low-redshift end. The distribution at higher redshifts then depends on cosmology in two ways: via the evolution of the volume element with redshift, and via the growth of structure with redshift. If expansion is faster, then the differential volume at higher redshifts is smaller relative to today, and the number density of clusters drops accordingly. And if structure growth proceeds more rapidly, then the cluster number density will be lower at high redshifts relative to today.

The exact dependence of cluster abundance on cosmology can be determined using numerical simulations or approximations such as the Press-Schechter formula (Equation 2.7). Figure 2.3.2 shows the results of simulations using three different values of the dark energy equation of state, and demonstrates the utility of a redshift-independent survey technique: the differential number density varies much more rapidly with w at high z.

An SZ survey alone, however, cannot determine $dN/dMdz$. At the very least, redshift information must be obtained from follow-up optical observations. The efficiency with which the survey is able to identify clusters as a function of mass—the selection function—is also crucial, and can be determined from follow-up observations or measurements of clusters with masses determined by other means. However, it is expected that the Compton-y parameter integrated over the cluster, a quantity proportional to the total thermal energy of the system, is a low scatter estimate of the mass [da Silva, 2004, Nagai, 2006, Motl et al., 2005, Kravtsov et al., 2006]. This offers the hope that the selection function might be determined from the survey data itself, with external data used as a cross-check.

The SZ Power Spectrum

An SZ cluster survey of sufficient breadth and depth will also contain enough information to estimate the high-ℓ CMB power spectrum. Anisotropies due to the SZ effect add power at arcminute scales, a range in which the primary anisotropies are damped. The SZ signal is expected to be the largest contributor to the variance at high ℓ once astrophysical contamination is removed. The amplitude of the SZ power spectrum depends strongly upon the amplitude of the matter power spectrum; defining σ_8 as the matter fluctuation on 8 Mpc h^{-1} scales, $C_{\ell,SZ}$ goes as $\sim \sigma_8^7$ Holder et al. [2007].

2.3.3 Requirements for an SZ Survey Instrument

An instrument capable of performing an SZ survey over a large patch of the sky must meet several requirements:

- It must be sensitive to radiation in bands where the SZ signal is significant, generally from 15 to 300 GHz.
- It must have good control of noise and systematic errors in order to recover the small amplitude SZ signals.
- Its resolution must be matched to cluster scales.
- It should be able to map clusters efficiently, which generally implies high sensitivity over a wide field of view.

- It should be able to observe in multiple bands in order to separate the thermal SZ signal from primary CMB anisotropies and astrophysical contamination.

These requirements drove the design of the South Pole Telescope and its SZ receiver.

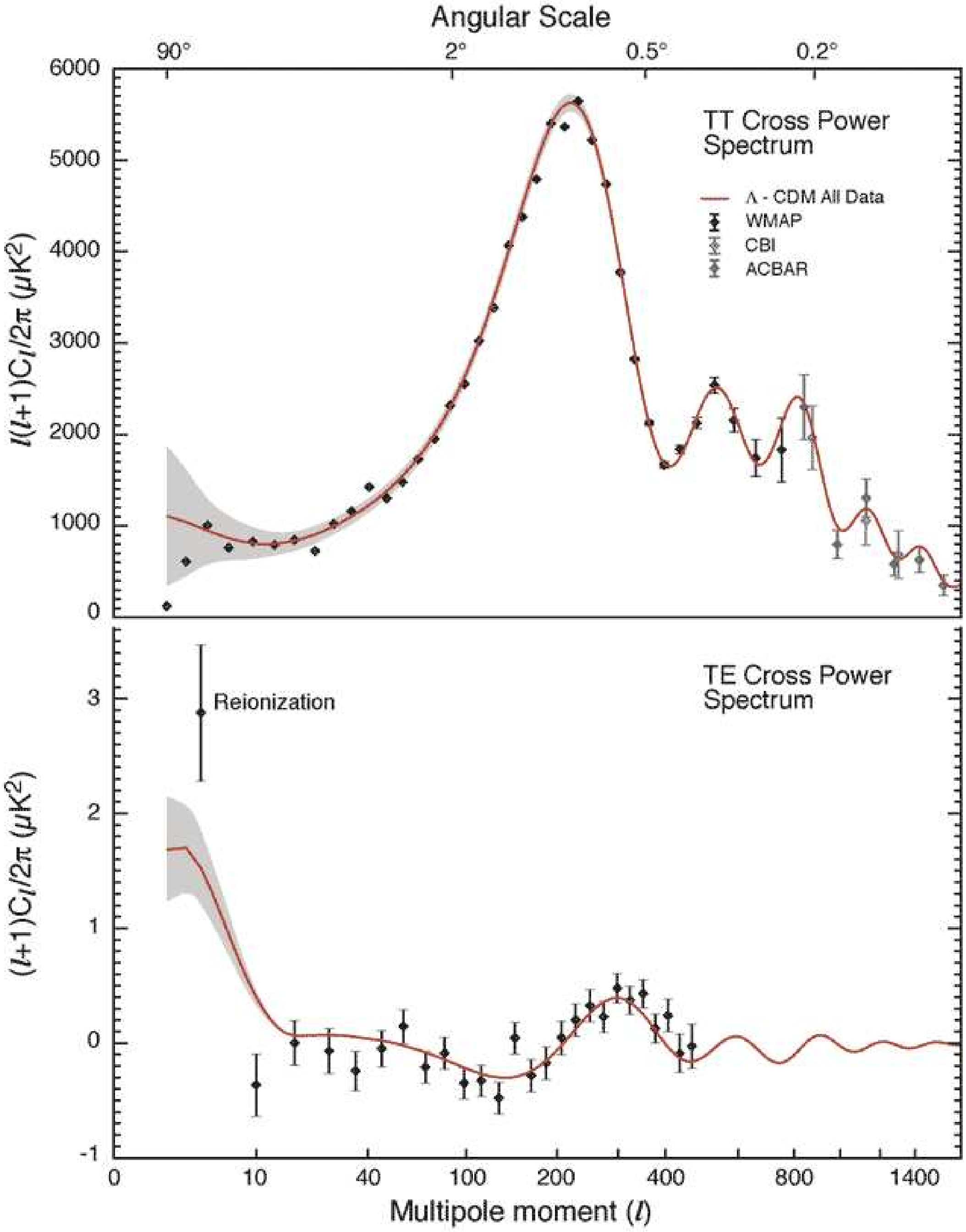

Figure 2.1. Recent measurements of the CMB power spectrum, courtesy the WMAP science team [Komatsu et al., 2009].

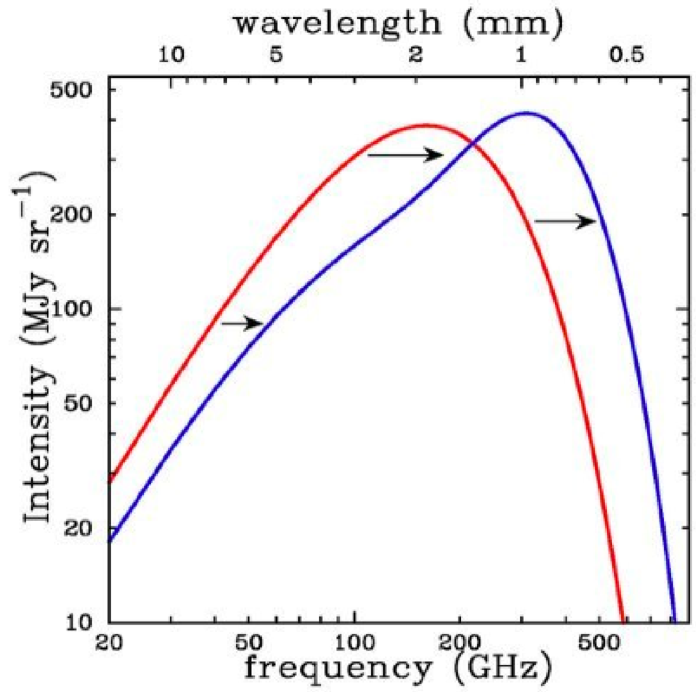

Figure 2.2. The change in intensity of the CMB due to the Sunyaev-Zel'dovich effect. The effect is exaggerated to show the important features. Figure courtesy Carlstrom et al. [2002].

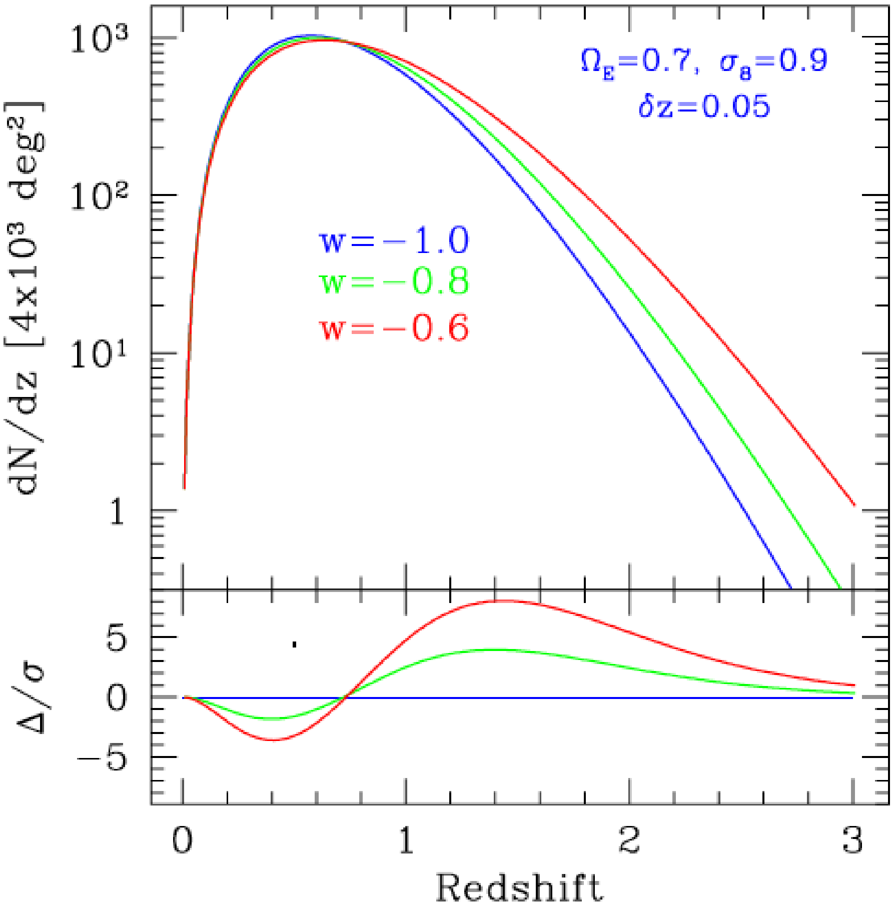

Figure 2.3. Cluster redshift distribution for three values of the dark energy equation of state. Figure from Mohr [2004].

Chapter 3

The South Pole Telescope

The SPT, pictured in Figure 3.1, is a telescope constructed for wide-field observations with large bolometer arrays. Its initial project is a multi-band millimeter wavelength survey of galaxy clusters via the SZ effect using a kilopixel bolometeric receiver. Subsequent projects will include polarization measurements of the CMB and sub-millimeter observations of protostars and protogalaxies.

These scientific objectives led to the design of an off-axis Gregorian telescope with a 10-meter diameter dish and a 1 $\deg^2$ field of view, and to the choice of an observing site at the South Pole. An overview of the telescope is given in [Carlstrom et al., 2009]. In this chapter, I will motivate the use of the South Pole for millimeter astronomy. I will then describe the mechanical, optical, and cryogenic design of the SPT, reserving discussion of the detectors and readout system for subsequent chapters.

3.1 Observing Site

Water absorbs microwave radiation and is poorly mixed in the atmosphere, so turbulent flows can wreak havoc for instruments like the SPT. A good millimeter-wavelength observing site therefore needs to have a low level of precipitable water vapor, and atmospheric conditions that are very stable. The South Pole is arguably the best such site in the world. During the austral winter, temperatures at the South Pole range from -40° to -80° C, so most water is frozen out of the atmosphere. Snowfall is only about 150 mm per year. A light katabatic wind of ~ 5 m/s blows in from East Antarctica and dominates the winter weather pattern; higher winds are rare. The site is at an elevation of 2847 m, but due to the earth's rotation, the atmosphere is even thinner than this altitude would suggest. The uninterrupted darkness of the winter months, in addition to allowing around-the-clock observation, helps maintain constant temperatures. The result is a site with low precipitable water vapor (see Figure 3.2), low opacities ($\tau \sim 0.03$ at zenith), and superb stability.

The site does have one rather obvious drawback: it is extremely remote. This is largely mitigated by the excellent logistics support provided by the United States Antarctic Program at the Amundsen-Scott South Pole Station. The Air National Guard provides flights to the station during the austral summer; during the other eight months of the year, the site is inaccessible, and the SPT is managed by its capable winterovers (Steve Padin and Zak

Figure 3.1. The South Pole Telescope during the last stages of construction, in the austral summer of 2006-2007. The large dish is the primary mirror, and the slightly elevated structure is the receiver cabin. During servicing and installation, the telescope is positioned so that the receiver cabin mates with the roof of the control room (right). The comoving ground shields were not yet installed when this picture was taken.

Staniszewski in 2007, Keith Vanderlinde and Dana Hrubes in 2008, and Erik Shirokoff and Ross Williamson in 2009). The ∼300,000 kg of components that comprise the SPT were flown to the South Pole on LC130 aircraft, and were assembled in the austral summer of 2006-2007.

3.2 Mechanical Design

The SPT is located approximately 1 km from the main South Pole Station. It sits on a thick pad of ice, which was formed by using a bulldozer to progressively add layers of compressed snow and was then left to harden over the course of a year. The weight of the structure is distributed by a hexagonal wooden raft, above which the telescope is raised on a 5.2 m high steel tower. This further distributes the load and, in a feature the SPT shares with most other buildings at the Pole, positions it above ground level to allow snow to blow underneath. The mount is an azimuth-elevation (AZ-EL) fork with both axes balanced to minimize deflections.

The telescope is supported by an L-shaped frame, with the 10 m diameter primary mirror

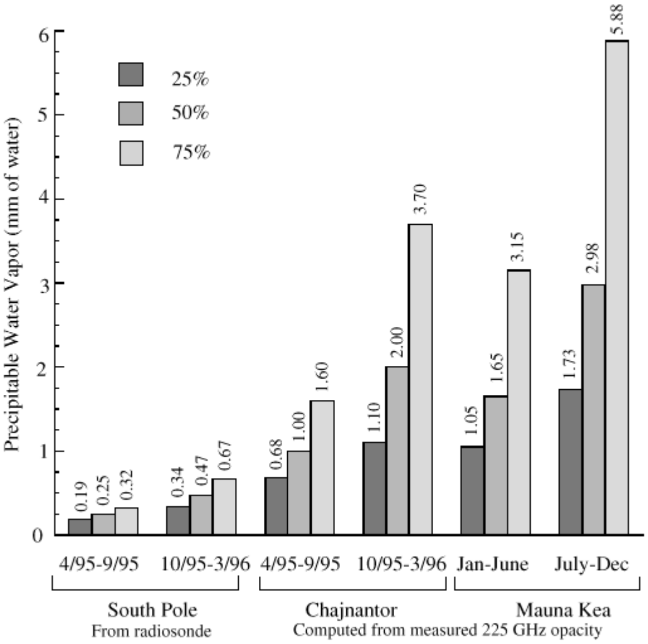

Figure 3.2. Precipitable water vapor at the South Pole relative to two other millimeter wavelength observing sites, Mauna Kea and the Atacama desert. Figure is from [Lane, 1998].

on one leg and the receiver cabin—which contains the secondary mirror, the receiver, and the readout electronics—on the other. The receiver cabin moves along with the primary mirror, and can be lowered and sealed to the roof of the control room for servicing and installation (see Figure 3.1). A 12 mm thick window of Zotefoam PPA30 allows light into the cabin. Comoving ground shields made of foam-core aluminum panels are mounted along the L-frame to reflect scattered radiation to the sky.

The telescope is driven along the AZ and EL axes by eight brushless DC motors with gearboxes. Two pairs of motors are used for each axis, one of which is sufficient to operate the telescope at reduced speeds. The pairs of AZ motors are mounted on opposite sides of the fork, and engage a large external ring gear on the AZ bearing. The EL motors are mounted on each arm of the fork, and drive a sector gear mounted on the L-frame. Scanning speeds of up to 4 deg/s in AZ and 2 deg/s in EL, and accelerations of up to 4 deg/s^2, are possible if not necessarily advisable. Each axis has an optical encoder capable of reconstructing the scan path to within 1 arcsec at moderate accelerations. Three small optical telescopes and a set of temperature and displacement sensors are available for use in constructing a pointing model. The current model, developed by Ryan Keisler at the University of Chicago, is accurate to within 7 arcsec rms.

3.3 Optics

A classical Gregorian telescope consists of two concave mirrors. The parabolodical primary (conic constant $k = -1$) collects light and brings it to a focus before the secondary, which in turn brings it to the Gregory focus. In order to minimize scattering, the SPT employs an off-axis Gregorian design (see Figure 3.3). The diameter of the primary aperture D sets the resolution of the telescope at a given wavelength via $\theta \sim \lambda/D$; since SZ cluster signals are at arcminute scales, the primary mirror must be at least 8 m in diameter for observations at $\lambda = 2$ mm. The SPT has a 10 m diameter primary, though only the inner ~ 8 m portion is illuminated. The mirrors are fully specified by three additional parameters: their radii of curvature and the desired Gregory focal length f.

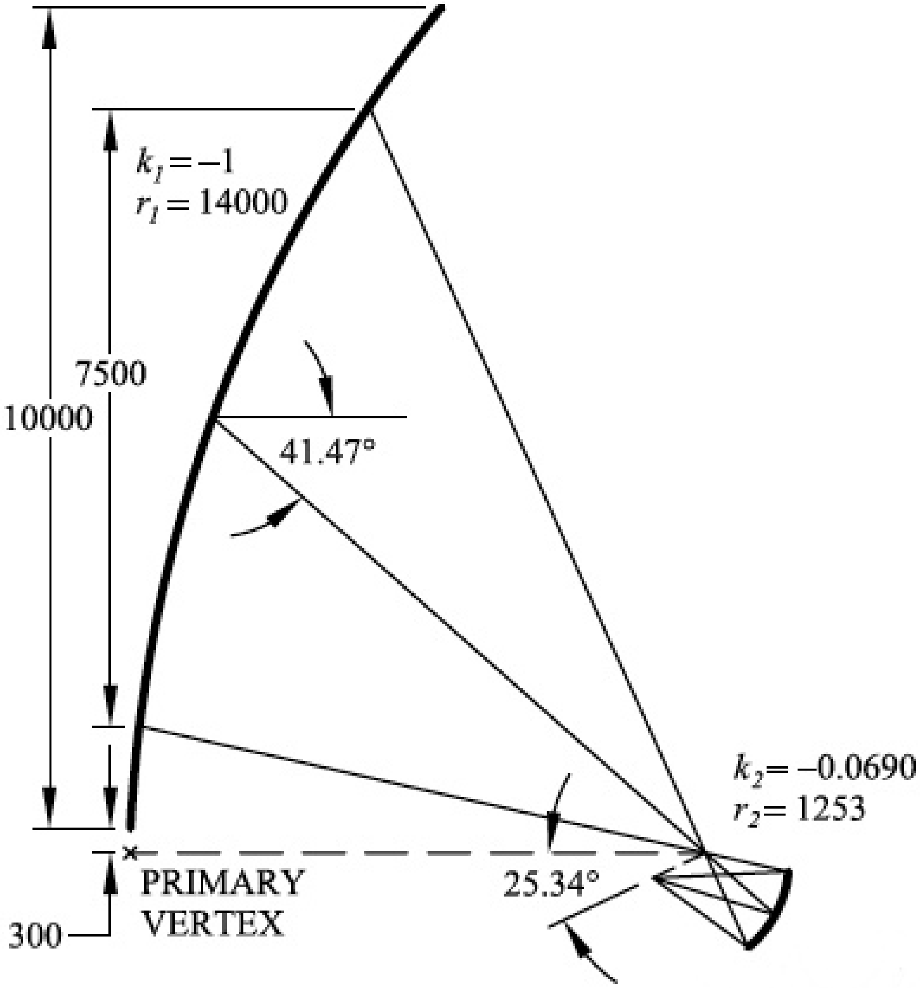

Figure 3.3. The primary and secondary SPT mirrors. k_n and r_n are the conic constant and the radius of curvature, respectively, for the primary ($n = 1$) and secondary ($n = 2$); lengths are in millimeters. The figure is taken from Padin et al. [2008].

The SPT detectors are fed by smooth-walled feedhorns, and the feedhorn diameter that maximizes efficiency for point source detection is given by $2F\lambda$, where $F = f/D$. For focal plane arrays like SPT, however, there is a balance to be struck between aperture efficiency and the number of detectors that can fit on the focal plane [Griffin et al., 2002]. The feedhorn diameter, the focal plane spacing, and the focal ratio of the telescope are therefore closely related, and must be jointly optimized. We chose to set the feedhorn diameter to 4.5 mm, slightly less than $2F\lambda$ at $\lambda = 2$ mm. This, in turn, fixed the focal ratio of the instrument to 1.3—a relatively fast optical system, although the final focal ratio is decreased slightly by the meniscus lens discussed below—which fed into the design of the secondary mirror. The remaining mirror parameters are set by clearances and other practical constraints.

3.3.1 Mirrors

The primary mirror is made up of 218 machined aluminum segments $\sim$0.5 m^2 by 60 mm thick, each with a surface accuracy of 5-10 μm. The panels are mounted on carbon-fiber-reinforced plastic supports, and each is seperately adjustable; from an initial surface profile error of 240 μm, photogrametry and holography measurements were used to refine the surface to within the design specification of 20 μm. The gaps between the panels were covered with strips of BeCu. A resistive de-icing system keeps the primary slightly above ambient temperatures.

In one of the more unique aspects of the SPT optical design, the ellpsoidal secondary mirror is cooled to $\sim$10 K, and is surrounded by cold HR-10 microwave absorber that serves as the stop. This helps to minimize scattering and reduce the loading on the detectors. The secondary mirror itself is 1 m in diameter, small enough to be machined from an aluminum billet. The structure is 50 mm thick, but has been lightweighted (20 kg) by cutting triangular pockets into the back, leaving a facesheet of 4 mm. Immediately after machining, it had a surface accuracy of 11 μm. Upon cooling, however, the surface error increased to 50 μm—still sufficient for millimeter wavelength observation, but sub-optimal.

The SPT secondary is similar to two of the mirrors in the APEX-SZ tertiary optics, which I helped to design and deploy. One of these two elements is nearly the same size as the SPT secondary, and the other is actually 50% larger. Since these mirrors were not cooled, the constraints on their mass and size were less severe, and they are consequently more robust in their design. For the 1.5 m diameter APEX-SZ tertiary, for example, the surface is 6.35 mm thick and is backed by two complementary sets of triangular ribbing (see Figure 3.4). The cost of this extra mechanical support is a considerable increase in mass: the larger mirror is 52 kg, and the smaller is 30 kg.

3.3.2 Lens

In between the secondary mirror and the focal plane is a thin meniscus lens which makes the final focus telecentric (i.e. the lens has an exit pupil at infinity, so that the focal plane is flat and the coupling to the feedhorns is improved). The lens also centers the beams on the secondary to reduce spillover, and helps fix a tight clearance by speeding up the final focus. It is made of High Density Polyethylene (HDPE), which has an index of refraction n of 1.567 in the millimeter band at 4 K [Lamb, 1996]. Without an anti-reflection coating, just under 10% of the light incident on the lens would be reflected at normal incidence, which is not an inconsiderable loss. For a single band receiver, a quarter wavelength coating

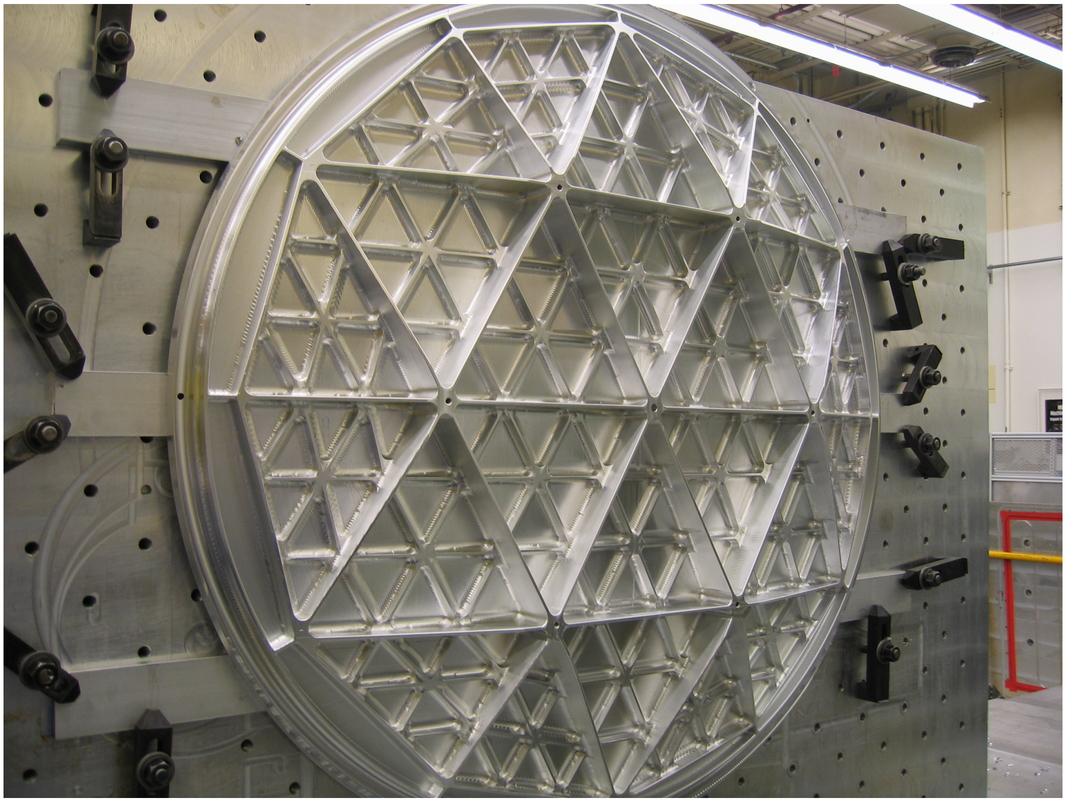

Figure 3.4. The backing structure of the APEX-SZ tertiary mirror. It is mechanically similar to the SPT secondary, but with an additional level of bracing.

would suffice to make the reflections negligible; for plastic lenses, this is often achieved by cutting square profile grooves in the surface. The SPT, however, observes concurrently in three bands, necessitating a coating that is effective across a wide range of frequencies.

Antireflection Coating

For both the SPT and APEX-SZ, I addressed this problem by using a graded refractive index antireflection coating. In this scheme, the index of refraction of the material is gradually varied from that of free space to that of the lens material, which we achieve by cutting grooves with a tapered profile. As long as the groove pitch is less than a wavelength, normally incident radiation at location z along the optical axis will see an effective index of refraction $n_{\mathrm{eff}} = \sqrt{(1-f(z))n_l^2 + f(z)}$, where $f(z)$ is the filling factor for the tapered groove at location z, and where n_l is the index of refraction of the lens material. Light coming in at other angles will see a different effective index function, but function will still be smooth as long as the angle of incidence is less than the angle of the taper. Note that this design is birefringent, and thus is potentially problematic for instruments that are sensitive to polarization.

In order to model the behavior of the tapered grooves, it is useful to consider the general problem of a plane wave travelling through a material with index of refraction n. The electric field can be written as a sum of leftgoing and rightgoing plane waves:

$$E(z) = E_r e^{ik_0 nz} + E_l e^{-ik_0 nz} \tag{3.1}$$

where k_0 is the wavenumber in free space, and the magnetic field is given by

$$H(z) = -\frac{i}{nk_0}\frac{\partial E}{\partial z} = ink_0 E_r e^{ik_0 nz} - ink_0 E_l e^{-ik_0 nz}. \tag{3.2}$$

As the wave travels a distance L along the z direction, it transforms according to

$$\begin{pmatrix} E(z+L) \\ H(z+L) \end{pmatrix} = \begin{pmatrix} \cos(nk_0 L) & \frac{i}{n}\sin(nk_0 L) \\ -in\sin(nk_0 L) & \cos(nk_0 L) \end{pmatrix} \begin{pmatrix} E(z) \\ H(z) \end{pmatrix}. \tag{3.3}$$

The matrix relating the fields at z and $z+L$ is called the transfer matrix, which I will denote as $M(n, L)$. Since the fields must be continuous across a boundary between materials of different indices of refraction, the transfer matrix of a series of sheets with indices n_i and thicknesses L_i is given by the matrix product $\Pi M(n_i, L_i)$. A taper defined by the function $n(z)$ can be modelled by dividing the function's domain into equal sized bins of width δ centered at $z_0, z_1, \ldots$, and computing the product $\Pi M(n(z_i), \delta)$.

The figure of merit for the groove design is the intensity transmission coefficient for the lens plus the antireflection layers on each side. We can find the amplitude transmission and reflection coefficients t and r by writing the electric field in free space before the lens as $E_0 e^{ik_0 z} + rE_0 e^{-ik_0 z}$, and after the lens as $tE_0 e^{ik_0 z}$. If the transfer matrix for the entire system is

$$M_s = \begin{pmatrix} A & B \\ C & D \end{pmatrix}, \tag{3.4}$$

then we must solve

$$\begin{pmatrix} t \\ n_0 t \end{pmatrix} = \begin{pmatrix} A & B \\ C & D \end{pmatrix} \begin{pmatrix} 1+r \\ n_0 - n_0 r \end{pmatrix}, \tag{3.5}$$

where $n_0 = 1$ is the index of refraction of free space (left in so that the equation can easily be generalized) and the common factors have been cancelled. By taking advantage of the symmetries of M, we can write the solution as

$$t = 2\frac{AD - BC}{A + Bn_0 + C/n_0 + D}. \tag{3.6}$$

The intensity transmission coefficient is then given by t^2.

As one might intuitively expect, t^2 is highest when the grooves are smoothly-tapered and deep. We are constrained, however, by the requirement that the groove pitch be $< \lambda$: grooves that are narrow and deep are both flimsy and difficult to machine. We therefore adopted a compromise design that falls within the practical constraints and has acceptable performance across all bands. The groove spacing is 0.622 mm, $\sim \lambda/2$ for the highest-frequency band. The depth is 0.635 mm, since an aspect ratio of $\sim 1:1$ eases the tooling requirements and yields grooves that are mechanically robust in HDPE. A gap of 0.08 mm, the same as the radius of the tip of the tool, was left between each groove; if the gap were much smaller, the narrow ridge of HDPE between grooves would deform during the machining process. The same grooves were cut into both sides of the lens, giving the lens a transmission coefficient of better than 97% at the center of each band (see Figure 3.5).

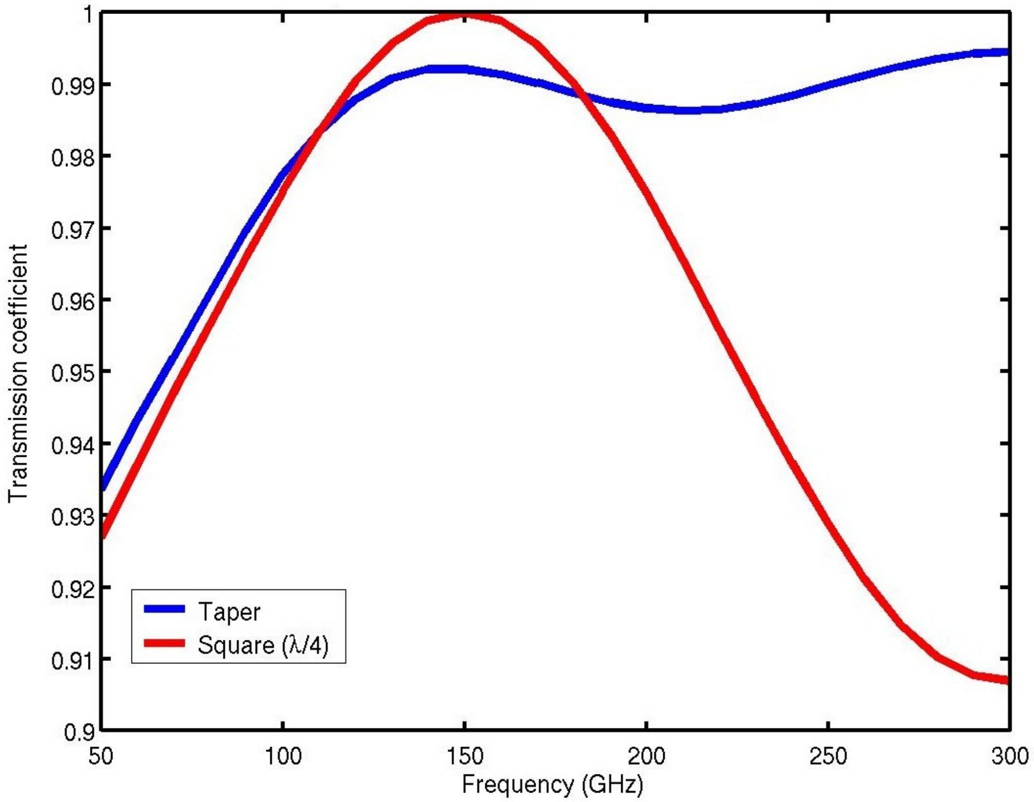

Figure 3.5. The transmission coefficient for the SPT tapered groove antireflection coating (both front and back), compared with a antireflection coating of square grooves tuned to $\lambda/4$ at 150 GHz. Performance is degraded only slightly at 150 GHz, is somewhat improved at 95 GHz, and is significantly improved at 220 GHz. A deeper coating would further improve performance, but would present practical challenges in its construction.

3.3.3 Band-defining Elements

In order to separate the SZ signal from primary CMB anisotropies and sources of astrophysical contamination, we designed the SPT to be sensitive to radiation within three frequency bands centered at 95, 150, and 220 GHz. Bolometers are intrinsically broadband devices, so the bands are defined by waveguides and filters. The focal plane optics are shown in Figure 3.6. The waveguides, whose cutoff frequency defines the low end of the band, sit directly in front of the integrating cavities of the detectors. Simulations by Jared Mehl [Mehl, 2009] showed that a conical flare between the waveguide and the integrating cavity improves the coupling at the low end of the band, so this feature was added for the the 2008 and 2009 observing seasons. The waveguides feed into smooth-walled conical horns, which (thinking of the system in transmission) broadcast approximately single-moded Gaussian beams out toward the lens and mirrors. The same horn diameter—4.5 mm–is used for all three bands, slightly reducing the performance but easing fabrication. Directly on top of the horns are capacitive mesh filters that define the upper end of the band. Filters further along in the optical chain block harmonic leaks, as does the vacuum window of the cryostat.

The mesh filters are provided by the Astronomy Instrumentation Group at Cardiff University. They are constructed by layering photolithographed metal grids with supporting sheets of polypropylene. The geometry of the mesh sets the frequency cutoff, and harmonic leaks are blocked by layering multiple filters. For the 2009 observing season, two high-cutoff filters and one filter with a 12 cm^{-1} cutoff are cooled to 50 K to prevent high frequency radiation from reaching the colder stages. Two more filters, one with a cutoff of 9 cm^{-1} at $\sim$10 K and another 12 cm^{-1} filter at 4 K, further protect from blue leaks, and the bands are defined by filters on the focal plane.

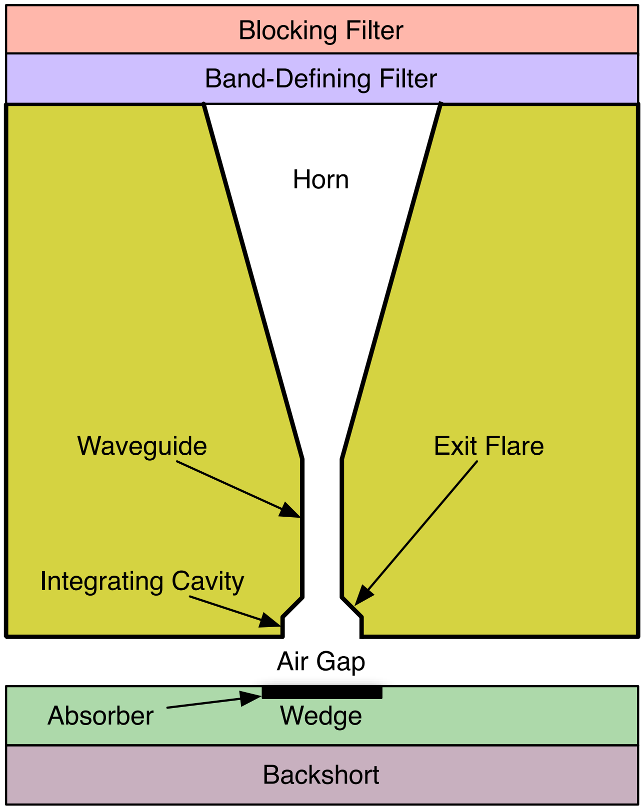

Figure 3.6. SPT focal plane optics. The capacitive mesh filters set the high pass cutoff, the feedhorn launches the beam, and the waveguide sets the low pass cutoff. The radiation not absorbed by the detector is reflected by the backshort into the integrating cavity. The exit flare was added between the waveguide and the integrating cavity for the 2008 and 2009 seasons.

The 2009 SPT bands are shown in Figure 3.7. Many detectors were measured using a Fourier Transform Spectrometer, the results were averaged over the detectors in a given band, and a smoothing kernel with a width 5 GHz was applied to remove spurious structure. The transmission weighted band centers are 98, 154, and 220 GHz, very near the design values. These bands are slightly wider than those used in 2007 and 2008, which improves the efficiency of the instrument at the cost of increased loading from the atmosphere.

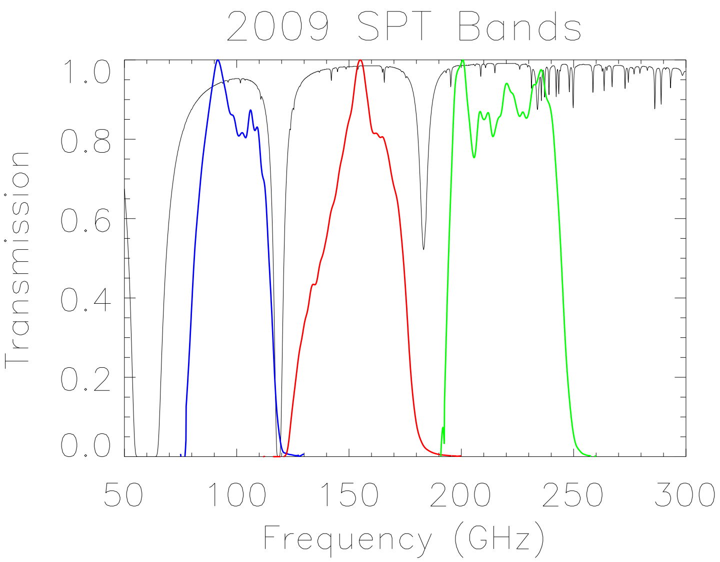

Figure 3.7. Measured 2009 SPT frequency bands. A model of the atmospheric transmission at zenith [Pardo et al., 2001] is in black, and the 95, 150, and 220 GHz bands are in blue, red, and green.

3.4 Cryogenics

The SPT focal plane must be cooled to ~ 250 mK and, as has already been discussed, several optical components must be cooled as well. Two interconnected custom cryostats were designed to meet these requirements. The larger of the two cools the secondary mirror, the cold stop surrounding the secondary mirror, and some of the blocking filters. The smaller one, the receiver cryostat, cools the focal plane, the lens, the remainder of the filters, and components of the readout system. The cryostats share a vacuum, but each has its own refrigeration system.

3.4.1 Pulse Tube Coolers

Both the optics and receiver cryostats employ pulse tube coolers, closed-cycle mechanical refrigerators that use ultra high purity (99.999%) Helium as a refrigerant. They operate by feeding pressurized Helium gas through a regenerator with high heat capacity, and then allowing the gas to expand while in contact with the cold head. A compressor is used to pressurize the gas, and an external drive motor is used to mediate the pressure cycle. The pulse tube coolers used by the optics and receiver cryostats—slightly modified versions of models PT410 and PT415, respectively—were supplied by Cryomech, Inc.[1] (The receiver pulse tube was upgraded from a PT410 after the 2007 observing season.) Since pulse tube coolers are closed-cycle refrigerators, neither cryostat must be refilled during normal operation, which is especially advantageous at the South Pole. The PT410 cools two stages to 10 K and 70 K, with cooling capacities of 10 W and 80 W. The PT415 specifications indicate

---

[1] 13 Falso Dr., Syracuse, NY 13211

1.5 W of cooling power at 4.2 K and 40 W at 45 K. Both systems are optimized for operation in a vertical orientation, and lose about 10% of their power when operated 30° from vertical. We designed the cryostats so that the pulse tubes are operating near peak efficiency when the telescope is pointed at typical observing angles of $\sim 45°$.

Pulse tube coolers were originally validated for use in bolometric instruments by Daniel Schwan at UC Berkeley; I assisted at the tail end of the process. The key question concerned the bolometer and readout sensitivity to electrical, vibrational, and thermal noise introduced by the $\sim$ 1.4 Hz pulsing. We significantly improved the electrical noise by replacing the standard motor driver, which used pulse-width modulation to generate the drive signal, with a low-noise linear motor driver[2]. We addressed vibrations by mounting the pulse tube on a bellows supplied by National Electrostatics Corp.[3], and by cooling the receiver cold heads via a flexible copper braid heat strap. Thermal noise is suppressed by the heat capacities of the cryostats. We also gain some protection against noise pickup by operating our detectors at AC frequencies. Nevertheless, some residual noise is observed in the detector signals at variable but low levels, so a notch filter at the pulse tube frequency is applied as a part of the data processing pipeline.

3.4.2 Sorption Fridge

The SPT focal plane is cooled to $\sim$ 250 mK using a three-stage Helium sorption fridge provided by Chase Research Cryogenics Ltd.[4] A schematic diagram of the refrigerator is shown in Figure 3.8. Each stage consists of a copper cold head and a heat pump filled with charcoal that acts as a helium vapor reservoir. When the heat pump is raised above 20 K, helium vapor desorbs from the pump and is condensed by an external cooling system into a liquid. Once the pump is dropped back down below 20 K, the helium slowly boils off, cooling the head to base temperature. Helium-4 is used as a refrigerant for the first stage, which is used to cycle the Helium-3 buffer stage and cold stage. The 3He buffer stage runs at $\sim$385 mK and can handle 60 μW of load, and the 3He cold stage runs at $\sim$250 mK with up to 1.4 μW of load. Additional cooling power is provided by a heat exchanger intercept.

The 3He in the buffer stage boils off after a hold time of about 36 hours. The fridge must then be cycled by heating the pumps, cooling the 4He stage, allowing the refrigerant to boil off, and then cooling the 3He stages. This process takes about three hours, and is handled automatically using hardware designed for the ACBAR experiment [Runyan et al., 2003] and software described in Chapter 6.

3.4.3 Cryostats

A cross-section of the optics and receiver cryostats is shown in Figure 3.9. There is a thermal break between the two vessels at their interface, near the focal plane end of the cold stop. By separating the cryostats in this manner, we made it possible to service and swap out receivers without having to disassemble and reassemble the optics. The drawback of this design is that it requires a light-tight thermal break in the stop and shield, which we

---

[2] `http://www.premotn.com`

[3] 7540 Graber Road, P.O. Box 620310, Middleton, WI 53562

[4] 140 Manchester Road, Sheffield, S10 5DL, UK

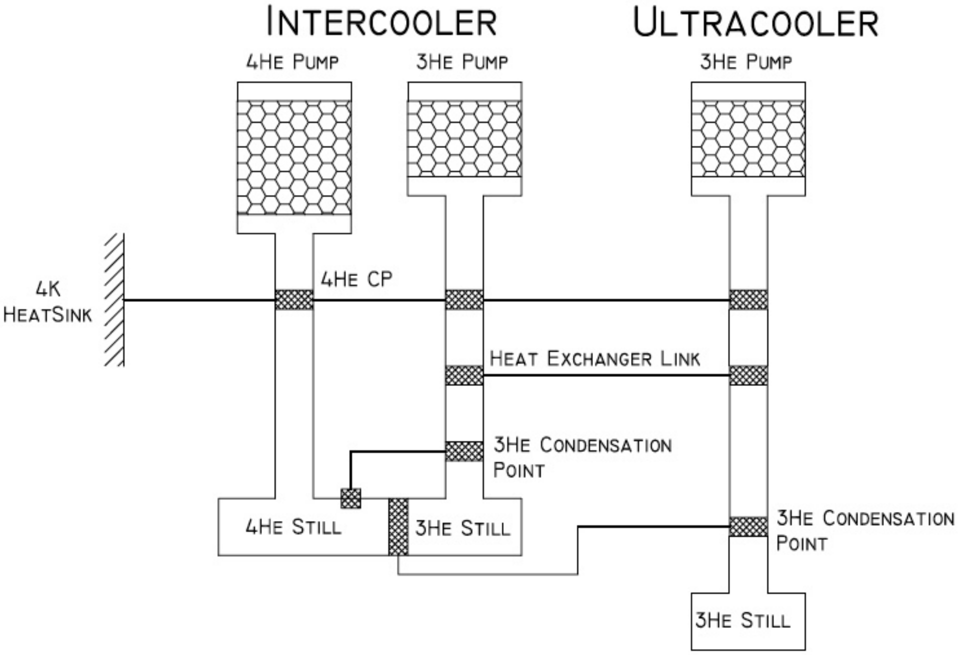

Figure 3.8. The 4He-3He-3He sorption fridge that cools the SPT focal plane. Diagram is from [Bhatia et al., 2000].

achieved by overlapping the receiver and optics cryostat shields by 20 mm, with ring baffles and aluminized-mylar skirts on the receiver end. The low-pass filters on the receiver side help block any radiation that might leak through this interface.

Optics Cryostat

The optics cryostat, designed at Case Western Reserve University, is described in detail in Padin et al. [2008]. Radiation enters the cryostat through a Zotefoam Propazote PPA-30 window with a 250 mm diameter aperture and a thickness of 100 mm. It then passes through the first set of filters, which are located near the focus of the primary mirror, and proceeds into a cavity enclosed by a shroud coated in HR-10 absorber. This absorber serves as the stop, and is cooled to 10 K by the second stage of the PT410. It is surrounded by a radiation shield cooled by the first stage; both the shroud and the shield are superinsulated. At the end of the cavity, the beam reflects off the secondary mirror toward the receiver cryostat. The mirror is supported off a back plate by a three-point mount. In the middle of the secondary is a small pipe leading to a chopped thermal source, the calibrator, which is used to assess detector liveness and relative calibrations.

The PT410 heads operate at temperatures of 5 K and 36 K, which implies heat loads of 2 W and 30 W. These loads are dominated by radiative transfer between the shroud and shield, which is given by

$$P_{\rm rad} = \sigma_b (T_1^4 - T_2^4) \left(\frac{1-\epsilon_1}{\epsilon_1 A_1} + \frac{1}{A_1} + \frac{1-\epsilon_2}{\epsilon_2 A_2} \right)^{-1}, \tag{3.7}$$

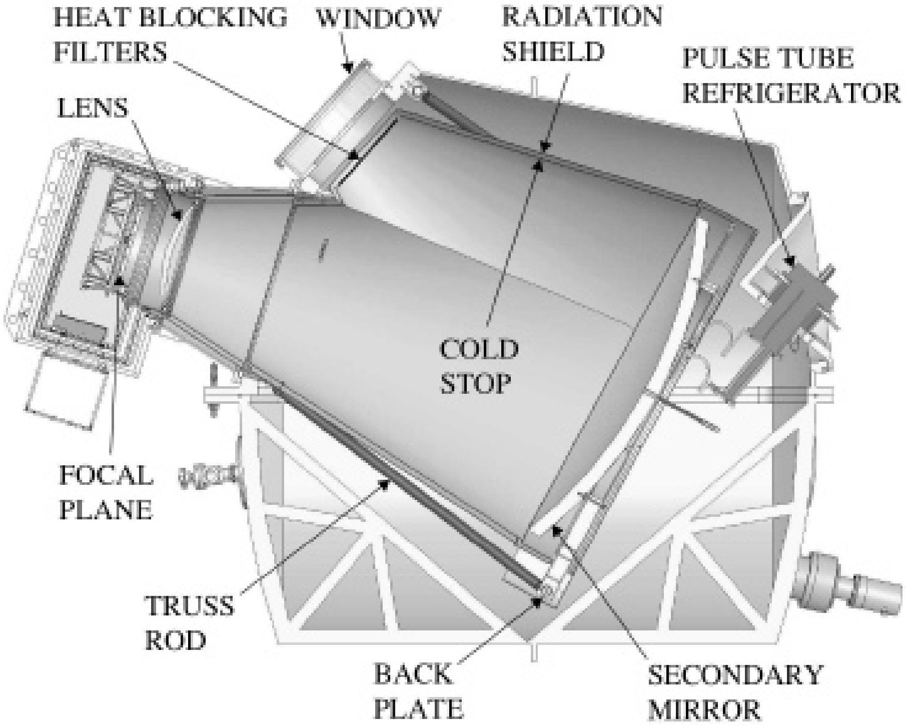

Figure 3.9. The SPT receiver cryostat (left) and optics cryostat (right). Figure from Padin et al. [2008].

where T_n, A_n, ϵ_n are the temperature, area, and emissivity of the nth surface. The shroud and shield areas are about 4 m^2, and the emissivity is about 0.05 for the shround, shield, and superinsulation. These numbers yield lower estimates for the load than we see in the field, probably due to gaps in the superinsulation.

Receiver Cryostat

The receiver cryostat was designed by Bradford Benson at UC Berkeley, who also led the team (of which I was a part) that debugged the receiver and deployed it to the South Pole. The receiver cryostat cools the lens, a series of filters, the focal plane, and a portion of the readout system. Except for a tilted surface on which the pulse tube is mounted, the sides of the dewar shell are flat and rectangular. As with the optics cryostat, the optical components are cooled to at least the temperature of the second pulse tube stage, and are surrounded by a radiation shield cooled by the first stage. The ~45 K plate that supports the radiation shield is stood off from the 300 K shell by G10 tubes, and the ~4 K main plate is stood off from the 50 K plate in a similar fashion. The main plate supports an additional set of radiation shields that cut down the radiative load on the focal plane assembly. The sorption fridge is also sunk to the main plate, which means that the sub-Kelvin cooling power

Table 3.1. Loading on receiver cryostat pulse tube stages.

Component	First stage Power (W)	Second stage Power (mW)
Radiation	6	3
G10 standoffs	3	150
Readout wiring	18	72
Housekeeping wiring	3	12
Total	30	237

depends strongly upon the main plate temperature. The wiring between the 300 K and 4 K electronics consists of 36 modules, each containing 37 0.1 mm diameter manganin wires in a nylon weave, provided by Tekdata[5]. The wiring assembly is heat sunk off the first pulse tube stage to reduce the heat load on the second stage. Another set of six wiring modules are used for thermometry and other housekeeping connections.

An estimate of the loading on the pulse tube stages is given in Table 3.1. The first stage loading is dominated by the readout wiring, and the second stage by the G10 standoffs. The loads fall below the specifications of the PT415, so temperatures below the nominal 45 K and 4.2 K are routinely achieved; the exact temperatures depend on the elevation angle at which the SPT is observing, but the second stage generally operates below 3 K.

The sub-Kelvin assembly is shown in Figure 3.10. It consists of gold-plated aluminum rings stood off in series from a 4 K ring by Vespel SP-1[6] tubes. There are three sub-Kelvin stages: one cooled by the sorption fridge heat exchanger, one cooled by the 3He buffer head, and one cooled to $\sim$ 250 mK by the 3He cold head. The first two stages are stood off from the main plate by Vespel tubes arranged in a drumhead pattern, and the last stage—the focal plane itself—is stood off from the buffer stage using vertically-oriented Vespel tubes with a larger radius. A second ring is supported off the buffer stage to heat sink a sheet of aluminized mylar that runs between the focal plane and the 4 K ring, and which serves to block any radio frequency (RF) radiation that might have leaked into the dewar.

The detectors on the focal plane are read out via pairs of wires running from the cold stage to the 4 K readout components. Over most of their length, the wires are low-inductance niobium stripline on thin kapton. On the end closest to the focal plane, the striplines are soldered to "pigtails" of 0.09 mm diameter Niobium-Titanium wire held in a Nomex[7] weave. The wiring is a significant contributor to the loading on the buffer stage, but is insignificant at the cold stage compared to the radiative load due to the emissive band-defining filters. The heat exchanger stage takes approximately 31 μW of loading and sits at $\sim$3 K, and the heat loads on the buffer stage and the cold stage are listed in Table 3.2. Note that the bolometers themselves, which will be discussed in the next chapter, contribute very little loading because of their low bias power.

---

[5] `http://www.cryoconnect.com`

[6] DuPoint, `http://www2.dupont.com/Vespel/en_US/`

[7] DuPoint, `http://www2.dupont.com/Nomex/en_US/`

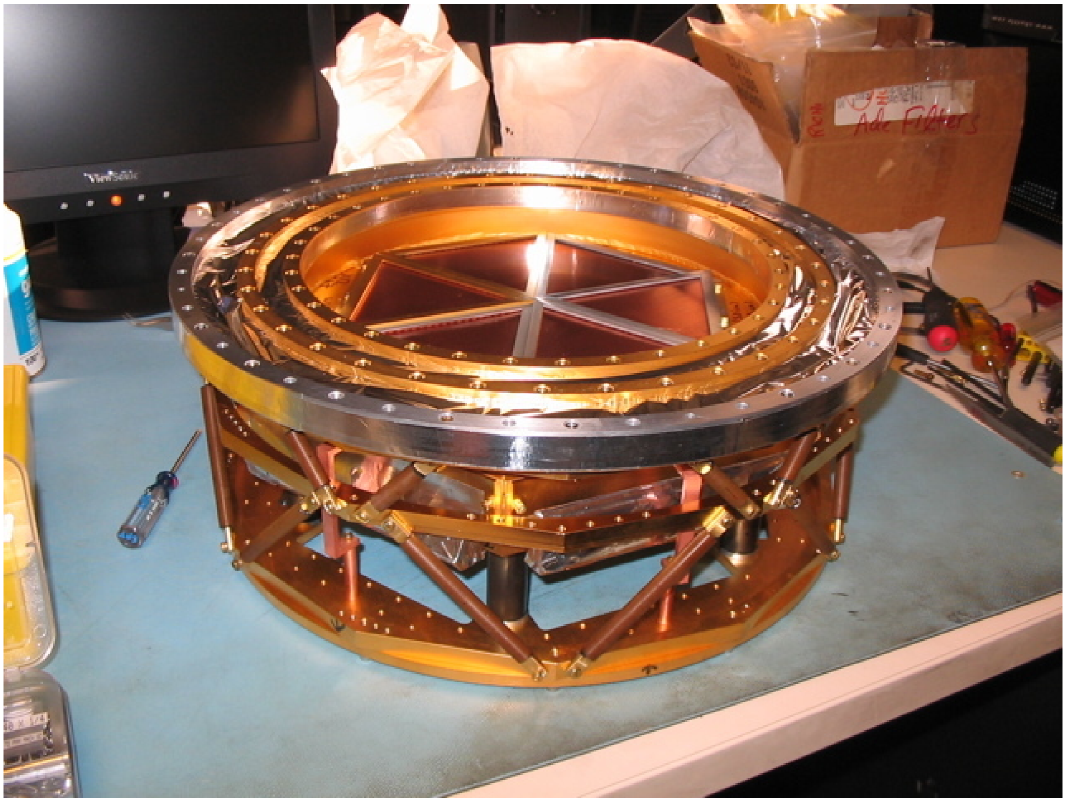

Figure 3.10. The SPT sub-Kelvin assembly. The top outermost ring (the one that is not gold-plated) mounts to the main plate. The stages cooled by the heat exchanger and the 3He buffer head, respectively, are stood off by Vespel SP-1 legs arranged in a drumhead. Finally, the focal plane is stood off from the buffer stage by the larger-radius Vespel tubes. The aluminized mylar annuli are the RF shielding.

Table 3.2. Loading on the sub-Kelvin stages.

Component	Buffer stage Power (μW)	Cold stage Power (μW)
Radiation	< 0.1	$\sim .8$
Vespel standoffs	15	.13
Readout wiring	20[a]	.01
Bolometers	-	.01
RF shielding	15	.15
Total	50	1.10

[a] Varies depending upon the temperature of the heat exchanger stage.

Chapter 4

Detector Array

A bolometer is a device that employs an electrical resitance thermometer to measure the temperature of a radiation absorber [Richards, 1994]. The detectors used in the SPT receiver are transition edge sensor (TES) bolometers fabricated in the Berkeley Microlab by Erik Shirokoff. This chapter will be devoted to the design, characterization, and optimization of these detectors. I will start by deriving the sensitivity and noise properties of a general voltage-biased bolometer. Next, I will describe the components of the SPT detectors and the process by which they were characterized and tested. I will end by assessing the performance of the detectors used in each of the first three SPT observing seasons.

4.1 A Model Bolometer

4.1.1 Operation

The basic behavior of a bolometric detector can be illustrated by the model shown in Figure 4.1. Consider an absorber with heat capacity $C \equiv \delta Q/\partial T$ coupled to a thermistor. The absorber sees power P given by the sum of the absorbed optical power P_{optical} and the thermistor bias power $P_{\text{bias}} = VI$. It is connected to a bath at temperature T_{bath} via a heat link, which is characterized by its thermal conductance $G \equiv \partial P/\partial T$. G is a temperature-dependent quantity that varies across the heat link, so a useful quantity related to G is the average conductance, $\bar{G} \equiv P/(T - T_{\text{bath}})$.

If the total power on the detector is constant, then the steady state heat flow is zero and the absorber temperature is also constant:

$$P_{\text{optical}} + VI = \bar{G}(T - T_{\text{bath}}). \tag{4.1}$$

If the optical power is perturbed at angular frequency ω by $\delta P_{\text{optical}} \exp(i\omega t)$, then the absorber temperature changes by $\delta T \exp(i\omega t)$ and the heat flow balance is given to first order by

$$P_{\text{optical}} + \delta P_{\text{optical}} e^{i\omega t} + VI + \frac{dP_{\text{bias}}}{dT}\delta T e^{i\omega t} = \bar{G}(T - T_{\text{bath}}) + G\delta T e^{i\omega t} + i\omega C\delta T e^{i\omega t}. \tag{4.2}$$

Taking the time dependent portion of this equation and cancelling the exponential, we get

$$\delta P_{\text{optical}} + \frac{dP_{\text{bias}}}{dT}\delta T = G\delta T + i\omega C\delta T. \tag{4.3}$$

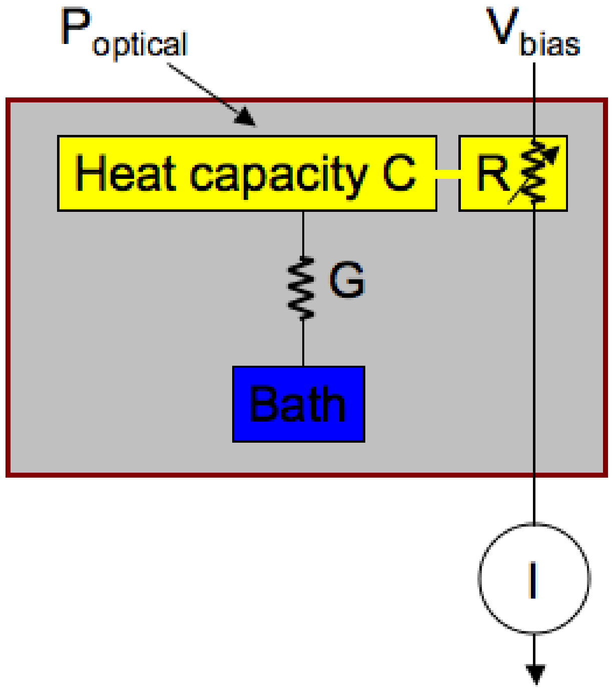

Figure 4.1. A bolometer consists of a thermal absorber with heat capacity C coupled to a bath by a heat link with thermal conductance G, and to a thermistor. The SPT detectors have spiderweb mesh absorbers coupled to a 250 mK bath, and TES thermistors biased at constant voltage V. The sum of the electrical power and the optical power $\mathrm{P}_{\mathrm{optical}}$ is held constant by feedback, thus producing a current I that depends sensitively on the optical load.

This gives us the temperature response:

$$\frac{G\delta T}{\delta P_{\mathrm{optical}}} = \frac{1}{1 + i\omega C/G + \frac{1}{G}\frac{dP_{\mathrm{bias}}}{dT}}. \tag{4.4}$$

Note that if the bias power is held constant, the bolometer will respond with an intrinsic time constant of $\tau_0 \equiv C/G$.

A detector biased at constant voltage V will operate under electrothermal feedback, wherein changes in the incident power produce changes in temperature, which in turn produce changes in the resistance of the sensor. The resulting change in bias power is given by $dP_{\mathrm{bias}}/dT = -(V^2/R^2)(dR/dT)$, which is often expressed in terms of the sharpness parameter $\alpha \equiv (T/R)(dR/dT)$. If α is positive, then the feedback is negative and will tend to push the device toward constant $P_{\mathrm{optical}} + P_{\mathrm{bias}}$. Equation 4.3 can be rearranged to give the effective thermal conductance for a voltage-biased bolometer:

$$G_{\mathrm{eff}} \equiv \frac{\delta P_{\mathrm{optical}}}{\delta T} = \left(\alpha\frac{P_{\mathrm{bias}}}{T} + G + i\omega C\right). \tag{4.5}$$

Negative electrothermal feedback therefore increases the effective thermal conductance of the device.

In analogy with negative feedback electrical amplifiers, we can define the loop gain $\mathcal{L}(\omega)$ as the response power over the incident power. Using Equation 4.5 and the fact that $\delta P = \delta P_{\text{bias}} + \delta P_{\text{optical}}$, we get

$$\mathcal{L}(\omega) \equiv -\frac{\delta P_{\text{bias}}}{\delta P} = \frac{P_{\text{bias}}\alpha}{GT(1+i\omega\tau_0)}. \tag{4.6}$$

The loop gain at zero frequency is therefore $\mathcal{L} = P_{\text{bias}}\alpha/GT$, and it rolls off at the intrinsic time constant of the bolometer. One last useful quantity is the responsivity of the detector, which we define as $S_I \equiv \delta I/\delta P_{\text{optical}}$. Substituting in our expressions for $I = P_{\text{bias}}/V$ and P_{optical}, we get

$$S_I = -\frac{1}{V}\frac{\mathcal{L}}{\mathcal{L}+1+i\omega\tau_0}, \tag{4.7}$$

or

$$S_I = -\frac{1}{V}\frac{\mathcal{L}}{\mathcal{L}+1}\frac{1}{1+i\omega\tau_{\text{eff}}} \tag{4.8}$$

where $\tau_{\text{eff}} = \tau_0/(\mathcal{L}+1)$. In the limit where $\mathcal{L} >> 1$, the responsivity is simply $1/V$, and the time constant of the device is reduced by feedback.

4.1.2 Noise

A voltage-biased bolometer with the right parameters can be a fast, sensitive, linear detector of radiation. In order to be useful for astronomical observations, though, it must also have good noise properties. Bolometer noise is conventionally discussed in terms of the noise equivalent power (NEP), the incident power required to obtain a signal-to-noise ratio of one in a 1 Hz bandwidth. The fundamental limit is set by NEP_γ, the shot noise of the arriving photons. An approximate expression for this noise at a single frequency ν can be obtained from the usual shot noise expression, $\langle(\Delta n)^2\rangle = n$. Since $n = P_\nu/h\nu$ where h is the Planck constant, the noise equivalent power in 1 s is given by $\text{NEP}_\gamma^2 \approx 2(h\nu)^2\langle(\Delta n)^2\rangle = 2P_\nu h\nu$, where the factor of 2 comes from the bandwidth associated with 1 s.

A more precise calculation of the photon NEP due to an emitting blackbody includes a second term due to the bosonic bunching of photons. The bunching term is larger for more coherent sources and smaller for beam-filling sources, and is difficult to compute from first principles for realistic loading scenarios. The ACBAR experiment has seen evidence for photon bunching [Runyan et al., 2003] at a level set by a "fudge factor" g of order unity which accounts for variations in source coherence. With this correction, the NEP due to photon shot noise is given by

$$\text{NEP}_\gamma = \sqrt{2\int P_\nu h\nu d\nu + \frac{1}{g}\int P_\nu^2 d\nu}. \tag{4.9}$$

Here, P_ν is the power spectral density for one dual-polarization mode

$$P_\nu = \frac{2\epsilon'\eta h\nu}{e^{h\nu/kT'}-1}, \tag{4.10}$$

where ϵ' and T' are the emissivity and temperature of the optical emitter and η is the efficiency with which the detector absorbs radiaton.

Once the bandwidth and optical load are set, the fundamental limit on NEP is fixed by Equation 4.9, and the goal is to design a device so that other noise sources are subdominant. Two significant noise sources are the Johnson noise of the thermistor, and thermal fluctuations across the heat link. The former goes as the usual Johnson noise expression reduced by electrothermal feedback [Lee et al., 1998]:

$$\mathrm{NEP}_J^2 = \frac{4kT}{R}\frac{1}{|S_I|^2}\left(\frac{\tau_{\mathrm{eff}}}{\tau_0}\right)^2\left(\frac{1+\omega^2\tau_0^2}{1+\omega^2\tau_{\mathrm{eff}}^2}\right) \tag{4.11}$$

where R is the termistor resistance and T is its temperature. The latter is discussed in detail by Mather [1982], and is given by $\mathrm{NEP}_G^2 = \gamma_T 4kT^2G$ where γ_T is an order unity factor that depends on the thermal conductivity of the heat link as a function of temperature. The noise in a representative SPT detector is discussed further in Section 4.2.2.

4.2 SPT Detectors

The SPT detectors are voltage-biased bolometers with TES thermistors and gold spiderweb mesh absorbers. I will describe the major components of the detectors, and will then discuss the process by which they were tested and characterized.

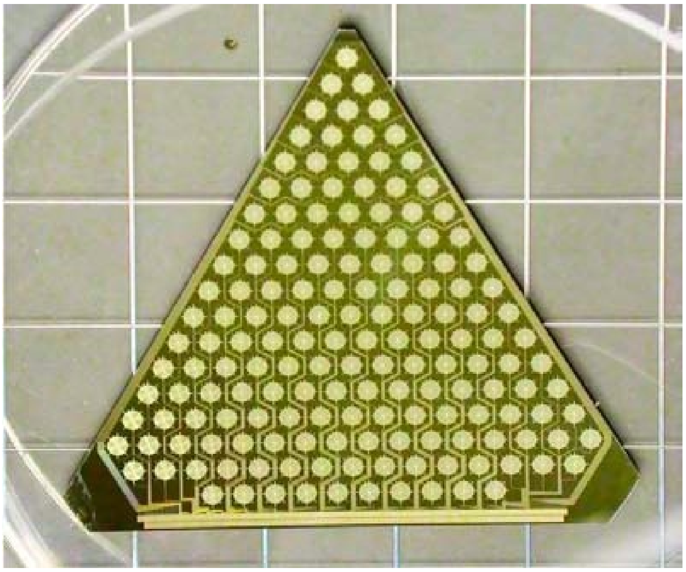

Figure 4.2. One of the six "wedges" of bolometers that comprise the SPT focal plane. The 161 3 mm diameter circular elements are the spiderweb absorbers. The TES thermistors are near the middle of the absorbers, and have leads running to wire bond pads on the bottom of the wedge.

4.2.1 Detector design

The SPT bolometers are fabricated on 100 mm diameter silicon wafers cut down into triangular "wedges." Six wedges make up the focal plane, and each is housed in a separate enclosure. This modular design allows detectors to be swapped and the band configuration of the receiver to be changed with relative ease. One of the six wedges that comprise the SPT focal plane is shown in Figure 4.2. The 161 circular features are the spiderweb mesh absorbers, in the middle of which are the TES thermistors. Each bolometer is coupled to the 250 mK bath by a gold heat link, and has two electrical leads running to wire bond pads on the edge of the wafer. The spacing of the detectors is determined by the layout of the feedhorns, which are organized in a hexagonal close-packed array and which have diameters of 4.5 mm. The wafer thickness is set to provide a $\lambda/4$ backshort between the absorber and the metallized back in the desired band, which maximizes absorption in the web.

Spiderweb Absorber

The spiderweb mesh absorber of an SPT detector is shown in Figure 4.3. The webs are made of 1 μm thick suspended silicon nitride, on top of which is deposited a thin layer of gold with a sheet resistance of $\sim 250\Omega/\Box$. By suspending the gold on a thermally isolated structure, we ensure that the connection to the bath is set by a heat link over which we have control. The diameter of the mesh is 3 mm, and the features are on scales much smaller than a wavelength. The mesh has its own time constant for absorption, referred to as the optical time constant τ_{opt}, that is generally slower than the time constant of the bolometer under feedback; for SPT detectors, τ_{opt} ~15 ms.

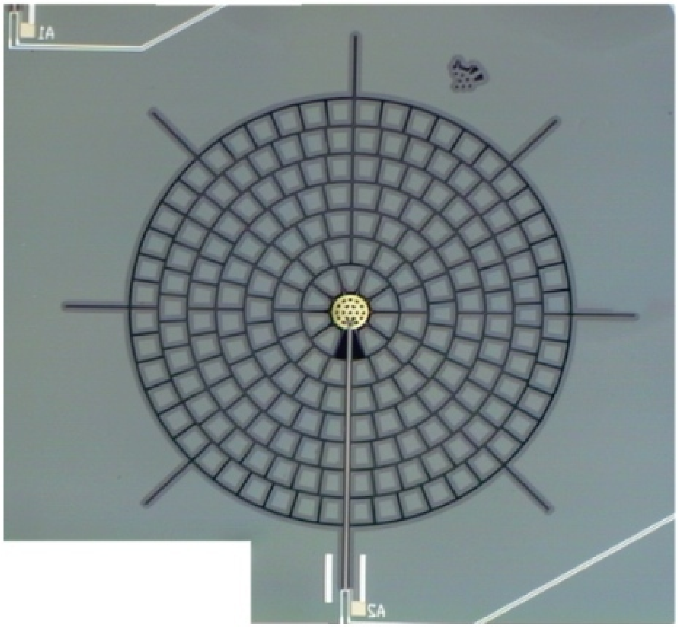

Figure 4.3. A spiderweb mesh absorber. The thermistor is located near the center of the web.

Since the intrinsic time constant of the bolometer is given by C/G, and since the specification for G is driven by our noise and loading requirements, adjusting the heat capacity of the absorber is the primary way by which we can set the thermal response time of the detectors. If the detector can respond on time scales faster than the bias power is able to compensate, then oscillations and instability will result. It can be shown that the time constant of the bias circuit τ_{bias} and the time constant of the TES τ must meet the criterion $\tau_{\text{bias}} \leq \tau/5.8$ [Irwin et al., 1998], where $\tau = \tau_0/(\mathcal{L}+1)$. In order to stay within this constraint, we slow the bolometers down by adding heat capacity to the absorber. This is done by depositing a thick layer of gold in the center of the web (Figure 4.4), which we refer to as "bling."

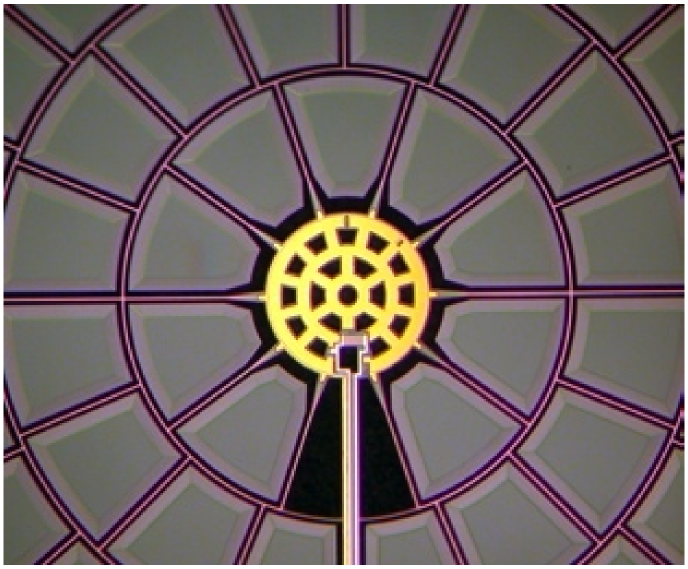

Figure 4.4. Heat capacity is added to the absorber by depositing a thick layer of gold in the center of the spiderweb.

TES Thermistor

The thermistor on each SPT detector is a TES, a superconductor held at its transition temperature. We chose an Aluminum-Titanium bilayer as our TES material in order to achieve a transition temperature T_c of about 550 mK, which is set by the proximity effect to a temperature between the T_cs of the two materials of the bilayer. The resistance of the bilayer drops rapidly from its normal resistance $R_n \sim 1\Omega$ to zero at T_c (Figure 4.5). The TES is coupled to the absorber through the bling, which is deposited on top of a region of the bilayer material. The heat capacity added by the bling raises the intrinsic thermal time constant from that of the TES itself, about 50 μs, to tens of milliseconds. This is slow enough for the detectors to be operated at loop gains of $\gtrsim 10$ without compromising stability in the current implementation of the AC readout.

Heat Link and Leads

Each bolometer requires two electrical leads and one thermal connection. The electrical leads are made of Aluminum, which is superconducting at the operating temperature. The

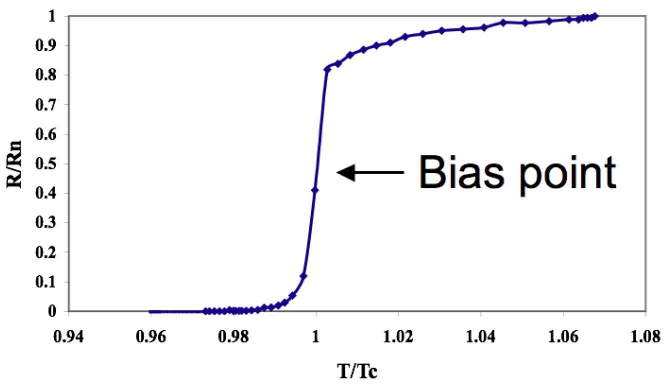

Figure 4.5. Resistance versus temperature for a TES. The bias power is set so that the temperature sits near T_c, which is ∼550 mK for the SPT devices.

heat link is made of gold with a thickness tuned to provide the appropriate G and $\bar{G}$. G values that are too high can lead to excess thermal carrier noise, while $\bar{G}$ values that are too low can cause the detectors to be saturated ($P_{\mathrm{optical}} > \bar{G}\Delta T$). The relationship between G and $\bar{G}$ is determined by the nature of the heat link. Assume that the link has a thermal conductivity of $k = k_0 T^n$, where $n \approx 1$ for conduction by electrons in cold normal metals and $n \approx 3$ for semiconductors and superconductors. The power flowing through the heat link is given by

$$P = A k_0 T^n \frac{dT}{dx} \tag{4.12}$$

where A is the cross-sectional area of the link. Integrating over the length l of the heat link, we see that the power is given by

$$P = \frac{A k_0}{l} \frac{1}{n+1} \left(T^{n+1} - T_{\mathrm{bath}}^{n+1} \right). \tag{4.13}$$

Thus, $G = \partial P / \partial T$ is related to $\bar{G} = \Delta P / \Delta T$ by

$$G = \bar{G}(n+1) \left(\frac{T - T_{\mathrm{bath}}}{T^{n+1} - T_{\mathrm{bath}}^{n+1}} \right) T^n. \tag{4.14}$$

Typical 150 GHz SPT detectors have values of $\bar{G}$ near 100 pW/K, so that approximately 30 pW of combined optical and electrical power are required to keep them at their operating temperature. For such a detector operating at $T_c \approx 550$ mK, with a heat link dominated by electron conduction in gold, $G \approx 140$ pW/K.

4.2.2 Testing and characterization

Since the Berkeley Microlab is a shared facility, fabrication conditions are not always completely repeatable. Consequently, it is often the case that several wedges must be fabricated and tested for every one viable wedge that is produced. In order for a wedge to be viable, it must have a high detector yield and good uniformity of properties across the wafer. It must also have detector G and T_c values within specifications, C/G time constants that meet the stability requirement, strong optical coupling, and acceptably fast optical time constants. A battery of tests was developed to evaluate whether new wedges met these criteria. In this section, I will provide a description of these diagnostics, most of which are automated using the SPT receiver control software discussed in Chapter 6.

1. Warm checks and preparation

After a new wedge was fabricated, a basic visual inspection was performed to check for damaged absorbers or leads. The wedge was then wire bonded and the continuity of each detector was checked. For reasons to be discussed in the next chapter, only seven out of every set of eight detectors can be read out using the current SPT readout system; therefore, if all of a given set of eight detectors passed the continuity check, one was tentatively chosen for omission. The wedge was then prepared for cooling in one of several testbed cryostats.

For the 2007-2009 seasons, SPT wedges were usually characterized in the lab with no optical loading on the detectors. This was mostly done because appropriate controlled loads were not readily available. A controlled load has since been built and installed in one of the test cryostats, but the next several diagnostics I will discuss do not require any optical power.

2. Network analysis

The SPT bolometers are wired in series with an inductor and a capacitor, and seven (or fewer) bolometers are biased and read out in parallel, each at the resonant frequency of its respective RLC resonator. Once the wedge was cooled to $\sim$ 700 mK in a test cryostat, cold enough for the bolometer leads to be superconducting ($T_c \sim 1$ K) but warm enough for the sensors themselves to be normal ($T_c \sim 500$ mK), the AC bias frequencies of the detectors were determined by performing a network analysis. This entailed sweeping an AC signal across each chain, varying the frequency of the signal from the bottom to the top of the readout bandwidth. The resonances observed in the network analysis output represented potentially viable bolometers, and the width of the resonances yielded an estimate of the detector's normal resistance. These values were stored in a configuration file, and a bias voltage was then provided to each bolometer at the appropriate frequency.

3. Transition temperatures

The bias frequencies having been set, a sample of detectors—at most one at a time from each parallel readout chain—was chosen for a measurement of transition temperature T_c. This test too was performed starting with the cold stage heated to $\sim$ 700 mK. The SPT readout system requires that a small bias voltage be placed across a detector in order for its current to be read out, so the smallest acceptable voltage was placed across the test pixels. The remainder of the detectors were biased at $\sim 1\mu$V: enough to keep them from superconducting at the temperatures of interest, but not enough to leak significant current into the test pixels. We then slowly lowered the cold stage temperature by adjusting the sorption fridge heat pump currents, recording the resistance of the test pixels in the process, until all of the test pixels were superconducting.

4. I-V curves

Once the transition temperatures had been estimated, the bolometers were biased at a high voltage, the stage was cooled to base temperature, and the I-V characteristics of the detectors were measured. The current-voltage (I-V) curve of a TES bolometer takes the distinctive form shown in Figure 4.6. As the bias voltage is lowered from the starting value, the current decreases until the bias power is just sufficient to hold the bolometer in its transition. Up until that point, the I-V curve is approximately ohmic with resistance R_n. When the transition is approached, electrothermal feedback begins to act, and a minimum current is reached at voltage V_{turn}. As the bias voltage is further reduced, the resistance drops to compensate, keeping the power across the bolometer approximately constant. Finally, once the voltage has been lowered far enough, one of two conditions will be met: the loop gain will increase to the point where the stability criterion is violated, or the bias power on the bolometer will be insufficient to offset a typical temperature fluctuation given the parasitic impedance in the system. In either case, the bolometer will quickly fall below T_c and will begin to superconduct.

It can be shown that

$$\mathcal{L} = \frac{1 - \frac{dI}{dV}R}{1 + \frac{dI}{dV}R} \tag{4.15}$$

(see, for example, [Irwin et al., 1998]), so the IV curve gives an estimate of the bolometer loop gain as a function of bias voltage. At the turnaround voltage ($dI/dV = 0$), the loop gain is one; at bias voltages well within the transition, a well-behaved bolometer will have a loop gain of $\gtrsim 10$. The I-V curve of the bolometer also gives an estimate of the saturation power, the amount of optical power beyond which the bolometer is unable to cool to its transition even with $P_{\text{bias}} = 0$. Finally, if the voltage is lowered all the way to the point where the TES begins to superconduct, then the I-V curve also gives us the limit on the loop gain beyond which the bolometer is unstable. Because the I-V curve provides such a wealth of information, this data was generally gathered for as many bolometers as possible.

5. Thermal time constants

The thermal time constants were also measured in a dark cryostat. The time constant depends on the loop gain, and we were generally interested in the intrinsic time constant (the loop gain having been estimated from the I-V curve), so we began by biasing a sample of detectors at their turnaround voltages. This was convenient because $\mathcal{L} = 1$ at the turnaround, making it straightforward to infer the intrinsic C/G. Once the detectors were biased, the readout system was configured to place a small AC signal across each of them[1]. This excitation frequency was swept at constant amplitude across the signal bandwidth of the detector, and the current response was recorded at each point.

For a typical SPT detector, the inferred intrinsic time constant was ~ 50 ms, speeding up to ~ 5 ms or faster in the transition. This τ corresponds to the TES and the bling moving together in temperature. There is a small thermal impedance between the TES and the bling, however, so the TES can respond independently at a reduced amplitude above its

---

[1] Since the SPT readout system runs the bolometers off AC bias signals, we actually placed the excitation signal in the sidelobes, using a clever scheme devised by Martin Lueker [Lueker et al., 2009].

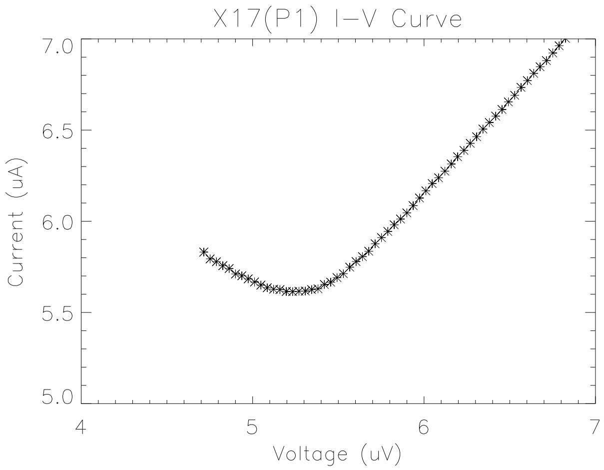

Figure 4.6. Bolometer I-V curve for a representative SPT bolometer. The bolometer behaves as a resistor at high biases, enters its transition, and then follows a curve such that $V \times I$ ∼constant.

initial single pole rolloff. At very high frequencies, there is another rolloff in the bolometer response that corresponds to the C/G of the TES decoupled from the bling (see Figure 4.7).

6. Dark Noise

Certain aspects of the detector noise can also be characterized in the lab. In a dark cryostat, the major contributors to the NEP will be thermal fluctuation noise and Johnson noise. Earlier generations of Berkeley TES detectors sometimes showed excess noise [Gildemeister et al., 2001], but when problems arose in the SPT dark noise measurements, it was consistently the fault of the test setup rather than the detectors. The notable exceptions to this rule were several of the early SPT wedges—including those deployed in 2007—which were marginally unstable at typical bias levels. One of the ways this manifested itself was as elevated noise due to oscillations. Dark noise measurements were therefore a useful diagnostic for identifying potentially problematic wedges.

Once a wedge had been characterized in a dark system, the poorly-performing detectors were deactivated by removing their wire bonds. If possible, the previously-omitted bolometer in a given set of eight was used to substitute for a deactivated detector. We then proceeded with follow-up tests in an optical cryostat. Due to time constraints during the 2007-2009 deployments, this testing often took place in the SPT receiver itself, where the calibrator served as the controlled optical load. The network analyses and bolometer I-V curves were redone in the new configuration, and a set of optical diagnostics were performed.

7. Optical time constants

One important characteristic that cannot be determined in a dark system is the the time constant at which a detector responds to optical signals. This time constant was measured by chopping or otherwise varying an optical source at a range of frequencies. In the SPT

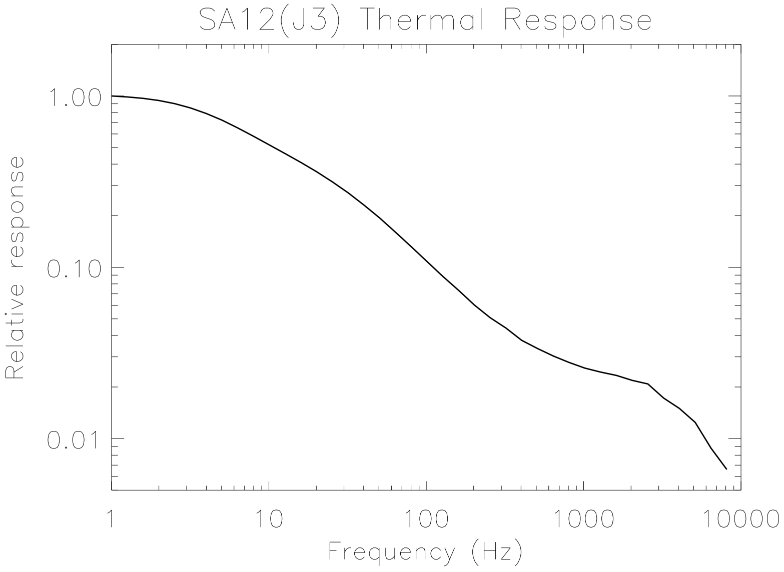

Figure 4.7. The response of a typical SPT bolometer to thermal fluctuations. The single pole rolloff at low frequency is due to the C/G of the detector plus the bling. The high-frequency rolloff corresponds to the C/G of the TES itself, after the bling has decoupled.

receiver, we chopped the calibrator starting at 5 Hz and ranging up to frequencies where the optical response was significantly rolled off. The chopper phase was accessible to the readout, so the measurement was performed with the readout system acting as a lock-in amplifier. The optical response of a typical bolometer is shown in Figure 4.8. It is approximately a single pole rolloff at $\tau \sim 15$ ms, with small additional structure due to the fact that some of the absorber heat capacity is distributed across the spiderweb mesh.

8. Noise

The bolometer noise performance was also assessed with photon noise contributing at realistic levels. For the 2009 SPT detectors, photon noise is dominant (or nearly so); for the 2007 wedges and some of the 2008 wedges, readout noise and thermal fluctuations across the heat link contributed at higher levels. The main culprit was that the G values for most of the 2007 and some of the 2008 wedges were larger than optimal given their optical efficiencies. Therefore, they required high levels of bias power that compromised the low-frequency noise performance, and had high white noise levels due to thermal fluctuations across the heat link ($\propto \sqrt{G}$).

Figure 4.9 shows a noise power spectrum for a typical detector on one of the 2008 wedges. This wedge was between the two extremes—its G values were slightly above optimal, but it was not nearly as compromised as the 2007 wedges. All of the main contributors to the noise are visible. The white noise for this detector, which was due to thermal fluctuations in the heat link and Johnson noise in the TES, is 410 $\mathrm{aW}^2/\mathrm{Hz}$. This level was decreased in later detectors by reducing the thermal conductivity of the heat link. A $1/f$ component from the readout system, which will be discussed in the next chapter, is also present at

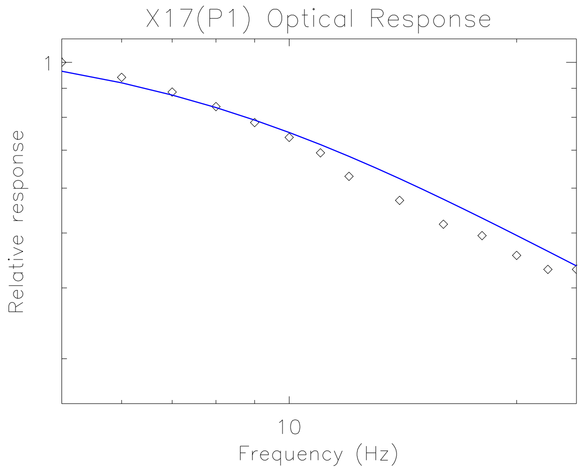

Figure 4.8. The optical response of a typical SPT bolometer, measured by sweeping the calibrator over a range of frequencies. The rolloff does not exactly follow the single-pole fit (blue) because the spiderweb mesh is a distributed heat capacity.

a level of 600 aW^2/Hz at 1 Hz; this component was made subdominant in later detectors by decreasing the required bias power. A $1/f^\alpha$ term due to atmospheric noise becomes important at very low frequencies, and is the dominant low frequency noise term in the 2009 detectors—for atmospheric noise with a Kolmogorov spectrum, $\alpha \sim 11/3$ [Bussmann et al., 2005]. The amplitude of this noise term depends on the observing frequency (higher for higher frequency bands) and on the atmospheric conditions at the time of the observation. Photon noise, rolled off by the optical time constant of the detector, is present at a level of 300 aW^2/Hz and represents the fundamental noise limit within the signal bandwidth. All of these contributions are at or near the expected levels, and their sum is a good fit to the measured noise power spectrum.

9. Optical efficiency, NET, and Mapping Speed

The final step in the process of validating a set of detectors is to determine how efficiently they couple to incoming radiation. There are two ways to approach this problem. The first is to place a calibrated load inside the cryostat, with relatively few optical elements in between the source and the detector; the second is to estimate the efficiency of the entire system by installing the detectors in the receiver and looking at an astronomical source with known flux.

In the former scheme, the measurement of the ratio of the measured incident power to the expected incident power is the product of the efficiencies of the bolometer and the integrating cavity, $\eta_{\mathrm{bolo}} \times \eta_{\mathrm{cavity}}$. Since most of the SPT detectors have not been tested in this configuration, the best estimates come from simulations described in Mehl [2009]. These suggest that the bolometers themselves have a thermal efficiency—the percentage of the power absorbed by the spiderweb mesh that is detected by the TES—of $\eta_{\mathrm{bolo}} \sim 0.84$. The cavity efficiency, which quantifies the amount of radiation entering the feedhorn that is reflected or radiated away, depends on the wedge thickness and the cavity geometry. In

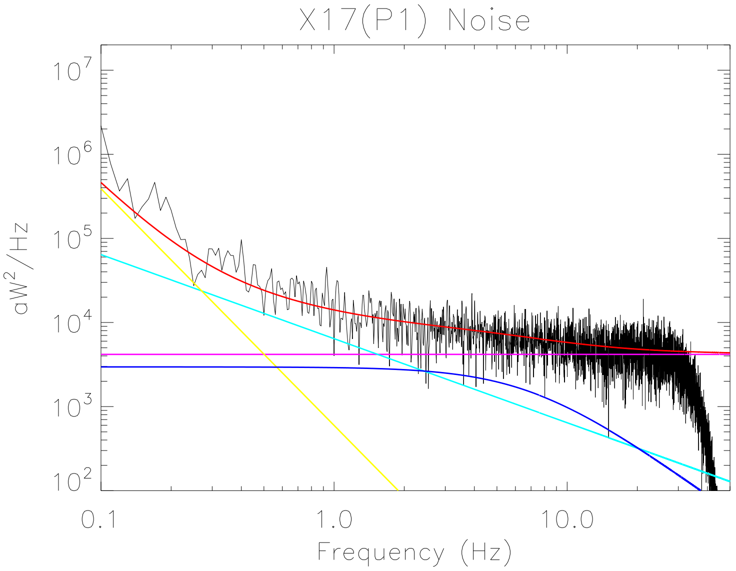

Figure 4.9. Typical detector noise in 2008, and a fit to a four-component noise model. The purple line is the white noise level due to thermal fluctuations in the heat link and Johnson noise in the detector. The blue line is photon noise. The aqua line is $1/f$ noise due to the readout system, which varies depending on the bias level and is subdominant for all 2009 wedges. The yellow line is $1/f^{\alpha}$ noise due to the atmosphere, where $\alpha \sim 11/3$. The red line is the sum of the contributions.

the 2008 and 2009 receivers, we expect η_{cavity} to be about 0.70, 0.79, and 0.75 at 95, 150, and 220 GHz. Therefore, we expect radiation that actually makes it to the feedhorns to be detected with an efficiency of about $0.79 \times 0.84 = 0.66$.

The efficiency measured in the second scheme is the ratio of the measured and expected power from an astronomical source. This includes losses incurred through the entire optical chain—the filters, mirrors, lenses, windows, and stop. It is difficult to estimate the expected efficiency from first principles, but the measured value is of great practical interest, since it bears directly on the speed at which the detectors in question will be able to map the sky. In order to quantify our expectations, we use a scheme laid out by Nils Halverson, in which the efficiencies of all elements in the optical system are estimated and multiplied—the mirrors using the Ruze scattering formula, the lens using the characteristics of the antireflection coating, and so on. By also keeping track of the temperature and emissivity of each element, we can calculate the expected optical load in the same process. A representative calculation, in this case for the 2009 150 GHz detectors, is shown in Table 4.1. The measured efficiency for these detectors was determined by observing of the bright HII region RCW38, and was found to be ~ 0.21, in good agreement with predictions.

Table 4.1. Efficiency and loading calculation for the 2009 150 GHz detectors. T_e is the physical temperature of the element, at which it will emit radiation depending on its emissivity ϵ. L_s is the loss due to scattering or spillover calculated using the Ruze formula for the mirrors, ZEMAX simulations for the stop, and antireflection coating simulations for the lens. T_s is the temperature of the region to which the radiation is scattered or at which it is absorbed. η is the efficiency of the element, η_{cum} is the cumulative efficiency, and P_{opt} is the optical power seen by the detector due to the element. All efficiencies are at the center of the band; the predicted band-averaged efficiency is 0.21 rather than 0.28. Excluding the design efficiency $\eta = 0.74$ of the secondary and stop, the band-averaged and peak efficiencies are 0.28 and 0.38, respectively. Table courtesy Bradford Benson.

Element	T_e	ϵ	L_s	T_s (K)	η	$\eta_{mathrmcum}$	P_{opt} (pW)
Bolometer	0.25	0.00	0.16	0.25	0.84	1.00	~ 0
Cavity	0.25	0.00	0.20	0.25	0.79	0.84	~ 0
Horn	0.25	0.00	0.00	0.25	1.00	0.66	~ 0
Band-defining Filter	0.25	0.05	0.00	0.25	0.95	0.66	~ 0
Blocking Filter	0.25	0.05	0.00	0.25	0.95	0.63	~ 0
IR Blocking Filter	4.00	0.02	0.00	4.00	0.98	0.60	0.017
4K Filter	4.00	0.05	0.00	4.00	0.95	0.59	0.042
4K IR Blocking Filter	4.00	0.02	0.00	4.00	0.98	0.56	0.016
Lens	5.00	0.02	0.02	10.0	0.96	0.55	0.099
Lens Filter	6.00	0.05	0.00	10.0	0.95	0.53	0.081
Secondary and Stop	10.0	0.20	0.06	10.0	0.74	0.50	0.854
10 K Filter	10.0	0.05	0.00	10.0	0.95	0.37	0.128
70 K IR Blocking Filter 1	70.0	0.02	0.00	70.0	0.98	0.36	0.474
70 K Filter	70.0	0.05	0.00	70.0	0.95	0.35	1.162
70 K IR Blocking Filter 2	70.0	0.02	0.00	70.0	0.98	0.33	0.442
300 K IR Blocking Filter	300	0.02	0.00	300	0.98	0.32	1.931
Window	300	0.01	0.00	300	0.98	0.32	0.947
Primary Mirror	220	0.02	0.06	9.0	0.91	0.32	1.443
Atmosphere	230	0.03	0.00	230	0.96	0.29	2.464
CMB	2.73	1.00	0.00	2.73	0.00	0.28	0.153
Total						0.28	10.2

Once the efficiency has been measured, we can combine that knowledge with the measured bands and NEP to calculate a noise-equivalent temperature (NET) for a detector: the temperature difference on the sky seen with a signal-to-noise of one in a 1 Hz bandwidth. The power detected from a source with temperature T is given by

$$P = 2kT\frac{(e^x-1)^2}{x^2e^x}\Delta\nu\frac{\nu^2}{c^2}A\Omega\eta, \tag{4.16}$$

where k and c are the Boltzmann constant and the speed of light, x is the dimensionless frequency, $\Delta\nu$ is the bandwidth, ν is the center frequency, $A\Omega$ is the throughput, and η is the efficiency. Substituting the NEP in for power, we get

$$\mathrm{NET} = \frac{\mathrm{NEP}}{2k\eta\Delta\nu}\frac{(e^x-1)^2}{x^2e^x}\frac{1}{A\Omega\nu^2/c^2}. \tag{4.17}$$

Note that in this definition, NET is in units of $T_{\mathrm{CMB}}\sqrt{\mathrm{s}}$ rather than the Rayleigh-Jeans limit ($T_{\mathrm{RJ}}\sqrt{\mathrm{s}}$). The latter is also used in the literature, and can be found by removing the $(e^x-1)^2/x^2e^x$ term from the above equation. Note also that this definition applies to extended sources; point source sensitivity must also include a term that penalizes detectors with more extended beams.

With this definition in hand, we can now determine the relative mapping speed of two competing wedges of detectors:

$$\mathrm{Speed} \propto N\frac{\Delta T^2}{\mathrm{NET}^2}, \tag{4.18}$$

where N is the number of working detectors on the wedge and ΔT is the expected signal in the given band (the same in all bands for the CMB, and different across bands for cluster SZ signals). The detectors that we chose to use for each season of SPT observations were those that maximized the mapping speed for SZ cluster signals, while simultaneously providing the component separation needed for removing astrophysical contamination.

We first went through this process before the 2007 deployment, ending up with a set of detectors with compromised performance that nevertheless yielded useful scientific and diagnostic data. An entirely new set of detectors was deployed in 2008. Five of the six 2008 wedges were vastly superior in stability and sensitivity to those deployed in 2007, with three being nearly optimal. The remaining three were swapped out for new wedges in 2009.

4.3 Focal Plane Performance

In this section, I will summarize the properties of the detectors used during each season of SPT SZ observations. The receiver has improved dramatically in sensitivity and performance over the course of its three years of operation. Since the 2009 focal plane is nearly optimal in terms of detector yield, efficiency, and NET, further improvements in the scientific capabilities of the SPT will come primarily from swapping 150 GHz sensitivity for additional 95 GHz sensitivity. The SZ signal is larger relative to the CMB signal in the 95 GHz band than in the 150 GHz band, and deeper observations at 95 GHz will also allow astrophysical contamination to be removed more effectively. We anticipate that one additional wedge will be operated at 95 GHz during the 2010 season.

4.3.1 2007

The 2007 SPT focal plane consisted of two wedges at 95 GHz, three at 150 GHz, and one at 220 GHz. These wedges had stability problems of varying degrees, and had to be biased within a narrow range to avoid the high loop gain regime while retaining sensitivity. Most of the detectors also had G values that were well above optimal, so thermal fluctuations across the heat links led to high NETs—a handful of 150 GHz detectors had NETs of $\sim 500\ \mu\mathrm{K_{CMB}}\sqrt{\mathrm{s}}$, but more typical values were 1000-2000 $\mu\mathrm{K_{CMB}}\sqrt{\mathrm{s}}$ at 95 and 150 GHz, and even higher at 220 GHz. Moreover, the wafer thicknesses were not tuned to optimize the cavity efficiency, so the optical efficiencies of the detectors were low. Nevertheless, we were able to obtain survey data that contributed to the results in Staniszewski et al. [2009], in which three previously-unknown galaxy clusters were discovered via the SZ effect. We also learned a great deal about the design and operation of the detectors, which led to significant improvements in subsequent seasons.

Due to the fact that up to seven detectors are read out in parallel, stability issues can be particularly vexing: If a single bolometer goes unstable, it compromises the performance of the entire chain. This often led to confusion, as it was not always clear which bolometer needed to be adjusted in order to return the chain back to health. In September 2007, I undertook a systematic and painstaking attempt to increase the number of useable detectors in the 2007 array. This entailed the construction of a bias schedule with entries for each detector, which was adjusted to bring unresponsive detectors lower and unstable detectors higher in their transitions. If it was unclear which detector in a given chain was exhibiting instabilities, then all of the detectors were biased above their transition and were brought back one at a time. Since re-tuning the entire array was a lengthy process (which has since been optimized), we iterated on the bias schedule only once per sorption fridge cycle.

We consider a detector to be "live" if it is biased in its transition, sees a response to the calibrator source, has acceptable noise performance, and sees a signal in response to changes in the telescope elevation angle. Once per sorption fridge cycle, we ran a suite of bolometer performance tests including a $\sim 2^\circ$ dip in elevation and an extended stationary calibrator stare. From this we determined the number of live detectors, with the results shown in Figure 4.10. The campaign to increase the detector yield paid off, with a gain of over 100 detectors between mid- and late-September. Even after these improvements, though, the 2007 focal plane never had more than about half of the theoretical maximum number of live detectors.

4.3.2 2008

During the 2007 observing season, Erik Shirokoff fabricated a new set of wedges with slower time constants, optimal wafer thicknesses, and lower G values. We characterized these detectors in the lab and identified a number of candidate wedges for the 2008 focal plane. These candidates were tested in the receiver during the austral summer of 2007-2008, and five wedges with superior sensitivity and stability were identified: three at 150 GHz and two at 220 GHz. They comprised 5/6 of the 2008 wedges. A sixth wedge at 95 GHz rounded out the focal plane, but was later found to have low yield and high variability; for the 2008

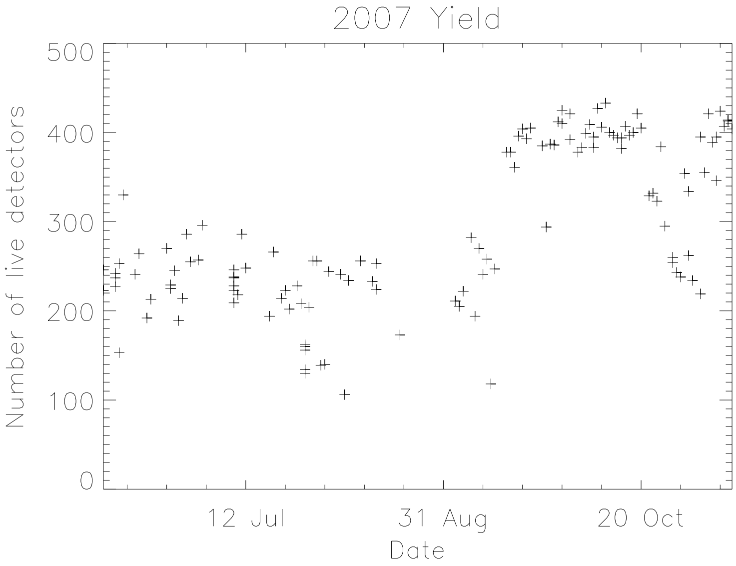

Figure 4.10. Number of live detectors during the 2007 season. Liveness was determined by response to the calibrator and to an elevation nod, and by the white noise level. A successful attempt to improve the detector yield took place in September 2007.

season, the SPT was effectively limited to the two higher-frequency bands. The focal plane optics were also changed in 2008 to increase the optical coupling.

I repeated the exercise of optimizing the detector yield, with incremental gains due to the increased stability of the bolometers. Yields of 550 to 600 bolometers were achieved on typical observing days—$\sim$ 200 at 220 GHz, $\sim$ 350 at 150 GHz, and tens of detectors at 95 GHz. Due to the lower G values and optical efficiency improvements, the NETs of the detectors were also dramatically improved, with typical values of 400-500 $\mu\mathrm{K_{CMB}}\sqrt{\mathrm{s}}$ at 150 GHz and 1000-1500 $\mu\mathrm{K_{CMB}}\sqrt{\mathrm{s}}$ at 220 GHz. One of the 150 GHz wedges had slightly higher NETs, and one of the 220 GHz wedges had slightly lower yield.

4.3.3 2009

Another set of wedges was fabricated and tested during the 2008 observing season, with the hope of replacing the defective 95 GHz wedge and potentially the sub-optimal 150 GHz and 220 GHz wedges as well. This attempt was successful: three new wedges were deployed in 2009, one at 95 GHz and two at 150 GHz. The decision was made to eliminate one of the 220 GHz wedges in order to focus on SZ measurements. As a result, the 2009 focal plane consists of about 120 live detectors at 95 GHz, 475 at 150 GHz, and 105 at 220 GHz. All wedges are stable with good noise performance. NETs are approximately 600 $\mu\mathrm{K_{CMB}}\sqrt{\mathrm{s}}$ at 95 GHz, and are at or near the best 2008 values for all 150 GHz and 220 GHz wedges.

4.3.4 Summary

The 2009 SPT receiver is an extremely powerful instrument that can efficiently map the CMB to high resolution over large fields. The advantages of the modular focal plane design have been demonstrated by a series of successful receiver upgrades, which are expected to continue in order to further optimize the SPT for SZ observations. The ~ 700 TES bolometers are stable with optical efficiencies that agree with predictions, and have well-understood noise properties. In the next chapter, I will discuss the system by which data from these bolometers are read out.

Chapter 5

Readout System

The SPT bolometers are low-noise, low-impedance devices biased at a constant voltage, and their output signal is a current proportional to the incident optical power. The readout system for these detectors must be able to measure this current to high precision over the bandwidth of the sky signal, $\sim 1 - 30$ Hz. Since the changes in the bolometer current are small relative to the typical input noise currents of room-temperature electronics, the readout must include a cold amplifier stage with a large forward gain. This amplifier must also have a low input impedance relative to the bolometer resistance ($\sim 1\Omega$) so as not to affect the current flowing through the TES. The entire system must have a noise level that is subdominant to the detector noise, which is $\sim 10\text{pA}/\sqrt{\text{Hz}}$ at the cold amplifier input. Finally, all of this must be accomplished without causing an excessive thermal load, which implies that the cold components must dissipate very little power and that the number of wires running to the cold stages must be small.

These requirements led to the design of a frequency-domain multiplexed (fMUX) readout system using series arrays of superconducting quantum interference devices (SQUIDs). A comprehensive description is provided in Lanting [2006]. The system was developed at Berkeley by a team including Helmuth Spieler, Matt Dobbs, Trevor Lanting, Martin Lueker, and others. I was involved in the characterization and troubleshooting process, and in the commissioning and deployment of the readout for the APEX-SZ and SPT receivers. In this chapter, I will give an overview of the fMUX readout system and its use in the SPT.

5.1 SQUIDs

A SQUID is a superconducting device that transduces magnetic flux to voltage. When coupled to an inductor (the "input coil") by a mutual inductance, it can act as a low-noise ammeter with a large forward gain. Feedback can be used to reduce the input impedance from the SQUID input coil to nearly zero. Since the device is superconducting, it dissipates very little power. All of these characteristics make SQUIDs particularly well-suited for reading out the SPT detectors.

5.1.1 Principles of Operation

A SQUID consists of a superconducting loop with two Josephson junctions connected in parallel[1]. A Josephson junction is a weak coupling between two superconductors through a barrier or constriction [Josephson, 1962]. The ensemble wavefunctions of the superconductors on either side of the junction overlap, and the voltage and current across the junction depend on the phase difference ϕ between the two:

$$\phi = \theta_2 - \theta_1 + \frac{2e}{\hbar}\int_1^2 \mathbf{A}(\mathbf{x},t)\cdot\mathbf{dl}, \tag{5.1}$$

where θ_1 and θ_2 are the phases on each side and $\mathbf{A}(\mathbf{x},t)$ is the vector potential. The current and voltage equations for the ideal Josephson junction are

$$I = I_c \sin\phi \tag{5.2}$$

and

$$\frac{d\phi}{dt} = \frac{2eV}{\hbar}, \tag{5.3}$$

where I_c is the critical current, a characteristic of the junction at a given temperature. The constant in the voltage equation is closely related to the magnetic flux quantum, $\Phi_0 \equiv h/2e$.

Real Josephson junctions have some parallel resistance R and capacitance C, so

$$I = I_c \sin\phi + \frac{V}{R} + C\frac{dV}{dt}. \tag{5.4}$$

This equation can be re-written in a more illuminating form:

$$\frac{\hbar C}{2e}\ddot{\phi} + \frac{\hbar}{2eR}\dot{\phi} = -\frac{d}{d\phi}(-I\phi - I_c\cos\phi) \tag{5.5}$$

where a dot denotes a derivative with respect to time. Notice that this is analogous to a particle moving in one dimension, with mass $\hbar C/2e$ and damping coefficient $\hbar/2eR$, under the influence of the potential $-I\phi - I_c\cos\phi$ (Figure 5.1). The parameters of the junctions in a SQUID are set so that the system is "over-damped"—the friction term dominates over the mass term. In this limit, the voltage-current relation for a junction is simply

$$V = R\sqrt{I^2 - I_c^2} \tag{5.6}$$

(Figure 5.2).

When two such junctions are connected in parallel with superconducting leads, the magnetic flux through the loop determines the phase differences across the two junctions ϕ_1 and ϕ_2 up to an integer factor of 2π:

$$\phi_2 - \phi_1 = 2\pi(n - \frac{\Phi}{\Phi_0}), \tag{5.7}$$

---

[1] I will limit this discussion to DC SQUIDs. A related device called the RF SQUID consists of just one Josephson junction.

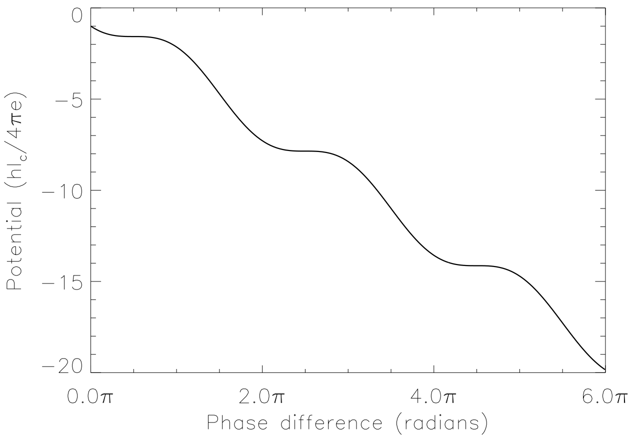

Figure 5.1. The effective potential for a Josephson junction.

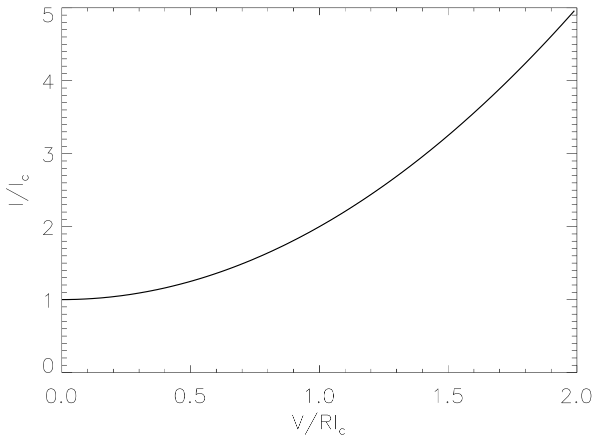

Figure 5.2. The voltage-current relation for an over-damped Josephson junction.

where $\Phi = \oint \mathbf{A} \cdot dl$ is the flux through the loop [Van Duzer and Turner, 1998]. The current through the SQUID is the sum of the currents through the individual junctions,

$$I = I_{c,1} \sin \phi_1 + I_{c,2} \sin \left(\phi_1 - \frac{2\pi\Phi}{\Phi_0} \right), \tag{5.8}$$

from which can be found the SQUID critical current,

$$I_{c,12} = \left((I_{c,1} - I_{c,2})^2 + 4 I_{c,1} I_{c,2} \cos^2 \left(\frac{2\pi\Phi}{\Phi_0} \right) \right)^{1/2}. \tag{5.9}$$

The critical current is at a maximum when the applied flux is an integer multiple of Φ_0, as shown in Figure 5.3.

If a current just above $I_{c,12}$ is applied to the SQUID, the voltage as a function of flux is periodic (Figure 5.4), oscillating between a minimum when the applied flux is an integer multiple of Φ_0 and a maximum when it is a half-integer multiple. This results in an output voltage that depends on the current applied to the input coil, which allows the SQUID to act as an ammeter.

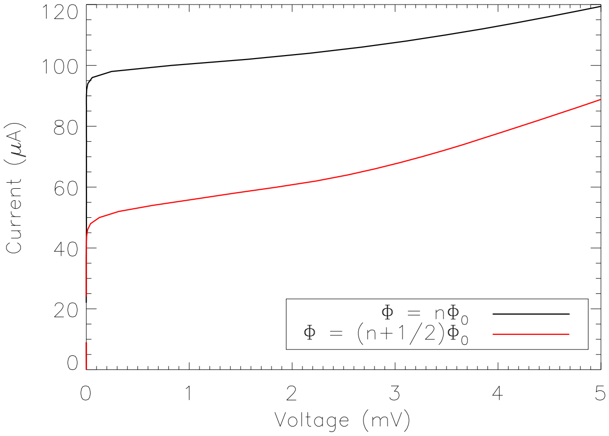

Figure 5.3. The voltage-current characteristics of an SPT SQUID array. A resistive component due to the wiring has been removed.

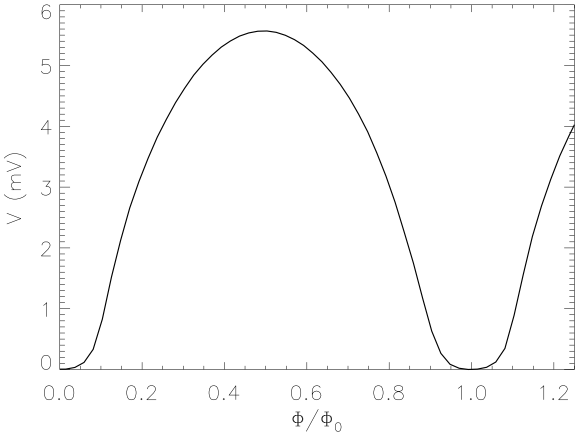

Figure 5.4. The flux-voltage characteristics of an SPT SQUID array with a current bias slightly larger than the critical current.

5.1.2 SPT SQUID arrays

The SPT readout system uses arrays of 100 SQUIDs wired in series[2]. The signals from the individual SQUIDs add coherently while their noise adds in quadrature, so the 100-element array provides a factor of 10 gain in signal-to-noise. Since all of the SQUIDs in an

---

[2] The SQUID arrays are supplied by the National Institute of Standards and Technology (NIST).

array receive the same current bias and see approximately the same magnetic flux, the array generally behaves as if it were a single SQUID. These SQUID arrays are remarkably low noise devices: their noise current is just 2.5 $\mathrm{pA}/\sqrt{\mathrm{Hz}}$, which is well below the photon limit of the bolometers.

The SQUID arrays in the SPT readout system are current biased such that the peak-to-peak voltage in the flux-voltage curve is maximized. This serves as an effective and easy-to-measure proxy for the current bias that maximizes $|\partial V/\partial\Phi|$, and thus the gain of the SQUID array, for values of flux near $\Phi_0/4$ and $3\Phi_0/4$ (see Figure 5.4). A flux bias must also be applied in order to operate the SQUIDs in this region of maximum gain, and a way must be devised to keep the flux approximately constant; otherwise, the SQUIDs will quickly lose gain and linearity when the input current changes.

This is achieved by operating the SQUIDs under "shunt feedback." In this configuration, the SQUID array output is amplified at room temperature, and an offset is applied to set the amplifier voltage output to zero at the desired flux bias point. Changes in the voltage are fed back to the input coil across a resistor. If the operating point is set to $3\Phi_0/4$, the feedback is negative, which linearizes the SQUID array and greatly increases its dynamic range—typical SPT SQUID arrays can read out currents of up to $\sim 10\ \mu\mathrm{A}_{\mathrm{rms}}$. If this level is exceeded, the SQUIDs can "flux jump" to a new stable operating point, which generally compromises the array performance.

Shunt feedback creates a virtual ground (albeit an imperfect one) at the input coil, thereby lowering the effective input impedance of the SQUIDs. This satisfies another of the requirements set out for the cold amplifier stage, leaving only the criterion that the loading on the cold stage be minimized. If one SQUID array were used to read out each of the 960 possible SPT bolometers, the load on the 3He buffer stage would be too great, and the wiring and electronics would quickly become unweildy. We must instead rely on each SQUID array to multiplex signals from several bolometers.

5.2 The fMUX Readout System

In order to read out many signals on a single line, the inputs must be multiplied by a set of orthogonal functions so that they can be disentangled at the output. One strategy that has been used for TES bolometer arrays is time-domain multiplexing, first developed at NIST [Chervenak et al., 1999], in which the orthogonal functions are square waveforms. Each of the N multiplexed detectors is connected to a SQUID switch, and the square waveforms turn the switches on and off sequentially so that the amplifier spends $1/N$th of its time reading out each detector. As long as the period of the switching waveforms is less than half the period of the fastest signals measured by the detectors, no information is lost. Another complementary method is frequency-domain multiplexing, first proposed at Berkeley [Yoon et al., 2001], in which the orthogonal functions are sinusoidal "carriers." Each multiplexed detector is biased at its own carrier frequency, and the currents are summed at the input of the readout. If the carriers are well-separated in frequency relative to the signal bandwidth, then the channels can be demodulated to base band at the output without loss of information. More elaborate schemes have also been proposed, such as time-frequency hybrids and code division multiplexing similar to that used in moble phones.

Both the time-domain and frequency-domain schemes have mature and useable implementations. The maximum number of detectors per multiplexed channel, set by typical amplifier bandwidths of 1-2 MHz, is roughly the same for each. The NIST time-domain electronics have gone through extensive revisions and have an order of magnitude less power consumption at room temperature than the Berkeley frequency-domain electronics[3]. However, we chose to read out the SPT detectors using frequency-domain multiplexing, as it offers several unique advantages. First, the Berkeley fMUX electronics require only one SQUID array per readout chain; the additional SQUIDs required for switching in the NIST time-domain electronics add considerably to the cost of the system. Second, the SQUID switches in the time-domain system dissipate a small but significant amount of power on the cold stage ($\sim$100 nW for an SPT-like focal plane), while the frequency-domain 250 mK components dissipate none. Finally, detectors biased at carrier bands are less sensitive to low-frequency noise from vibrations and amplifier gain variations. Another attractive feature of the fMUX system is that it band limits the SQUID noise, while the time-domain SQUID noise is broadband and subject to aliasing. This noise would be completely subdominant in the SPT, but it could become important in the future as multiplexing bandwidths increase.

Figure 5.5 shows a conceptual diagram of the fMUX readout system. In the SPT, seven detectors are read out by a single SQUID array. Each of the detectors is wired in series with an inductor and a capacitor, and the RLC resonator sets the carrier frequency and bandwidth. Typical bias frequencies for the SPT range from 300 kHz to 1 MHz. The resonance widths $\Delta f = R/2\pi L$ are $\lesssim 10$ kHz, which meets the stability criterion discussed in Chapter 4 for $\tau \sim$1 ms detectors, and resonances are separated in frequency by ~ 75 kHz to keep crosstalk $< 1\%$ and bias and noise leakage low. The "bias comb" is generated by seven direct digital synthesizer (DDS) chips[4]. These bias currents are summed and sent to the system ground across a 30 mΩ bias resistor at 4 K, which sets up the required voltage bias across the bolometers, and the bolometer currents are summed at 250 mK before being sent back to the 4 K SQUID array input coil. By summing the biases before the cold stage and the output currents on the cold stage, we reduce the cold wiring heat load by a factor of seven.

The SQUID array output voltage is amplified at room temperature by a high gain-bandwidth operational amplifier[5], set to roll off with a single RC pole at 1 MHz. This bandwidth, along with the required frequency separation, is what fixes the maximum number of channels to ~ 7. Signals at frequencies $>> 1$ MHz incur a significant phase shift over the 300 K-to-4 K wiring loop, and shorter wire lengths would compromise cryogenic performance. Consequently, an RC shunt (lead-lag) filter is used at the op-amp input to reduce the high-frequency gain of the amplifier chain. The op-amp output is fed back across a 10 kΩ feedback resistor to the SQUID input coil. As previously discussed, this keeps the SQUID array linear and stable while increasing its dynamic range and reducing its input impedance.

A "nulling comb" is also fed into the SQUID input coil in order to keep the input current within the dynamic range of the SQUID array. The DDS chips generate both an I and a Q output; the former is used to generate the bias comb, and the latter is mixed with the

---

[3] As discussed below, power consumption has been dramatically reduced in a subsequent generation of fMUX electronics.

[4] Analog Devices part number AD9854.

[5] Burr-Brown part number OPA847.

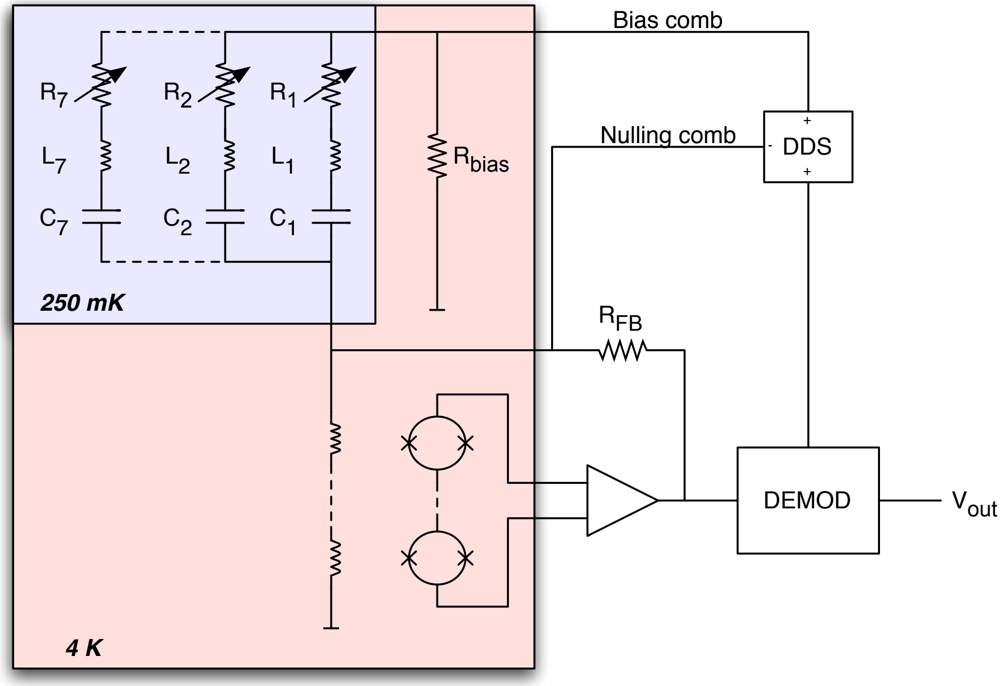

Figure 5.5. The Berkeley fMUX system. Each bolometer R_i is wired in series with an inductor L_i and a capacitor C_i. A "bias comb" of AC currents is generated by seven Direct Digital Synthesizer (DDS) chips (condensed to one unit in the diagram), and is connected to the (room temperature) system ground through the bias resistor R_{bias}. The bolometer currents are summed at 250 mK and fed through the SQUID array input coil, and the SQUID output is amplified and fed back. The DDSes are also used to generate an inverted "nulling comb" that cancels out most of the current at the input coil. Seven demodulators (again condensed to a single DEMOD unit) produce output currents at base band from the amplifier output and the DDS signals.

inverted I component to generate the nulling comb with the amplitudes and phases necessary to cancel $\sim$ 99% of the bolometer current. Without carrier nulling, 1-2 typical bolometer carriers would be enough to exceed the limits of the SQUIDs, even under shunt feedback. Since the bolometer currents stay roughly constant (except for the small perturbations that constitute the signal), the nulling comb amplitudes and phases need only be recomputed on roughly an hourly basis, barring large slews in the telescope elevation angle.

The amplifier output is brought back to base band by a set of seven custom demodulators[6]. Each demodulator is clocked by its corresponding DDS, and outputs data at 400 Hz. An active 8-pole Butterworth filter bandwidth limits the demodulated signal to avoid aliasing. The base band signals are then transfered to a computer using a high-speed digital I/O (DIO) card[7], downsampled to 100 Hz by way of a finite impulse response (FIR) filter, and stored to disk in 1 ms samples.

---

[6] Implemented with Texas Instruments part number 74CBT3253.

[7] National Instruments part number NI-PCI-6534

5.2.1 Cold Components

RLC Resonators

The 250 mK components of the fMUX system are limited to the inductors and capacitors that form the RLC resonators (Figure 5.6). Since all of the bolometers have an operating resistance of $\sim 1\Omega$, the inductors must also have the same value for every channel in order to maintain a constant width. We use 15.8 μH superconducting lithographed inductors provided by TRW[8]. Each inductor chip contains eight inductors, so twenty are required for a wedge of detectors. The resonant frequencies are set by $1/2\pi\sqrt{LC}$; we use commercially-available ceramic NP0 chip capacitors, with 1-4 components stacked in parallel to produce the required frequencies. Both the inductors and capacitors are mounted on a circuit board to which the bolometer leads are wire bonded. This board has a flexible portion that bends 180°, bringing the summed bolometer signals to connectors on the back of the focal plane. Two wires run from 250 mK for each multiplexed chain: one to the bias resistor, and one to the SQUID array input coil.

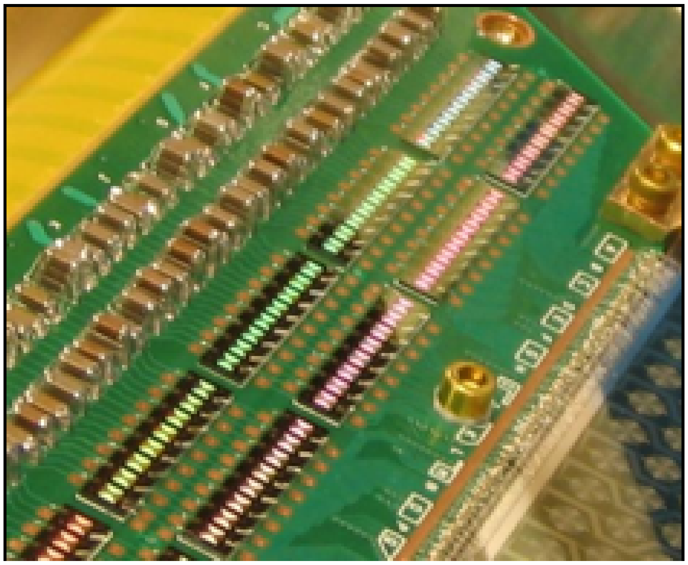

Figure 5.6. Inductors and capacitors at 250 mK. Each of the rectangular chips on the left contains eight inductors, and the stacks of surface-mount components are the capacitors. Capacitors and inductors are mounted on both the top and the bottom of the board that is wire bonded to the detector wedge.

SQUID Cards

The 250 mK wiring is connected to cards at 4 K, each of which contains eight SQUID arrays and eight 30 mΩ bias resistors (Figure 5.7). These cards are enclosed in Cryoperm[9] shields to attenuate magnetic fields. The SQUID arrays are mounted on 9 mm square pads

---

[8] Now a part of Northrop Grumman Corp.

[9] `http://www.amuneal.com`

of superconducting Niobium foil, which pins magnetic flux and thus reduces time-dependent field variations. The two shields together cut down magnetic pickup by a factor of 2.5×10^4. Since the detectors are biased at 100s of kHz, magnetic fields changing at low frequencies (due, for example, to the receiver cabin moving with respect to the earth's magnetic field) do not introduce noise as long as the SQUID performance remains nominal. I tested the shielding in the lab by applying a field with an external coil, and found that this design was sufficient to avoid adverse effects on the SQUIDs.

If the SQUID array is cooled in the presence of a non-uniform field, or if a sudden discharge drives a large current, flux can get trapped at different levels by the superconducting loops. This breaks the coherence of the array response and degrades the array performance. The SQUIDs must be heated above their transition temperature to remove trapped flux, so 100 Ω heating resistors are mounted next to each array.

The SQUID cards plug into edge connectors attached to the 12 cm wire harnesses described in Chapter 3, which run to the SQUID controller connectors on the cryostat shell.

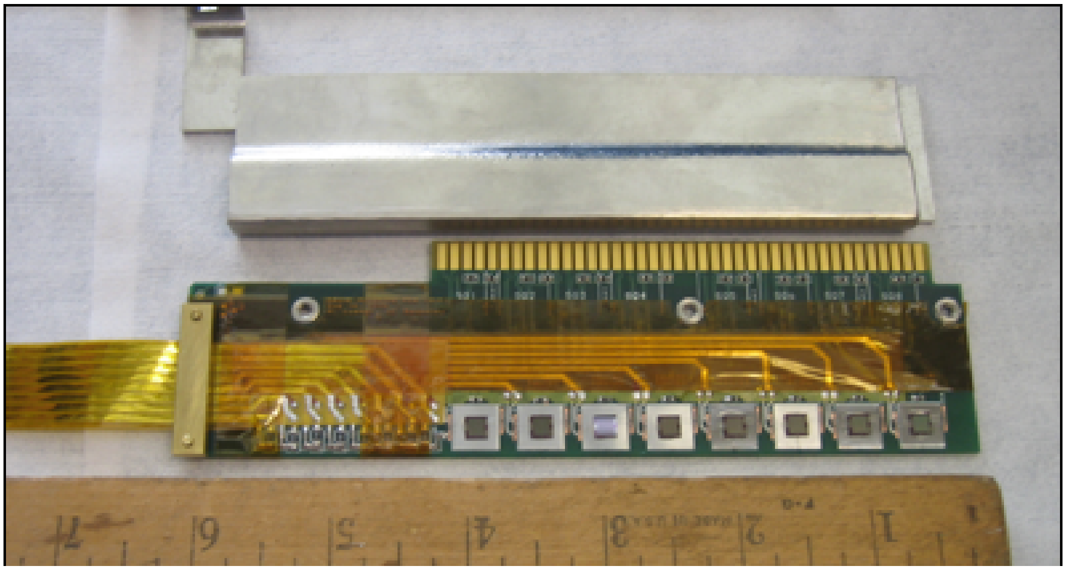

Figure 5.7. 4 K SQUID cards. Each card contains eight NIST SQUID arrays (right) and eight bias resistors (left), and is enclosed in a Cryoperm magnetic shield (top).

5.2.2 Warm Components

SQUID Controllers

The SQUID controller cards (Figure 5.8) are responsible for biasing the SQUID arrays and setting up the flux-locked loops. They plug directly into connectors on the cryostat shell, and are enclosed in RF-tight aluminum boxes to protect the highly-sensitive SQUIDS against noise pickup and trapped flux. As further precautions, all of the digital components on the board are isolated in an RF shield, and the digital and analog grounds are separated. Current biases and flux biases are provided to each SQUID array using digital to analog converters (DACs). A third set of DACs provides voltages to power the 100 Ω heaters, and a fourth set provides offset voltages to the op-amps inside the flux locked loops. The SQUID controllers also house the op-amps and feedback resistors, switches to open and close the flux locked loops and power the op-amps, and various signal-conditioning filters. A field-programmable gate array (FPGA) and associated IC's are used to command these various components.

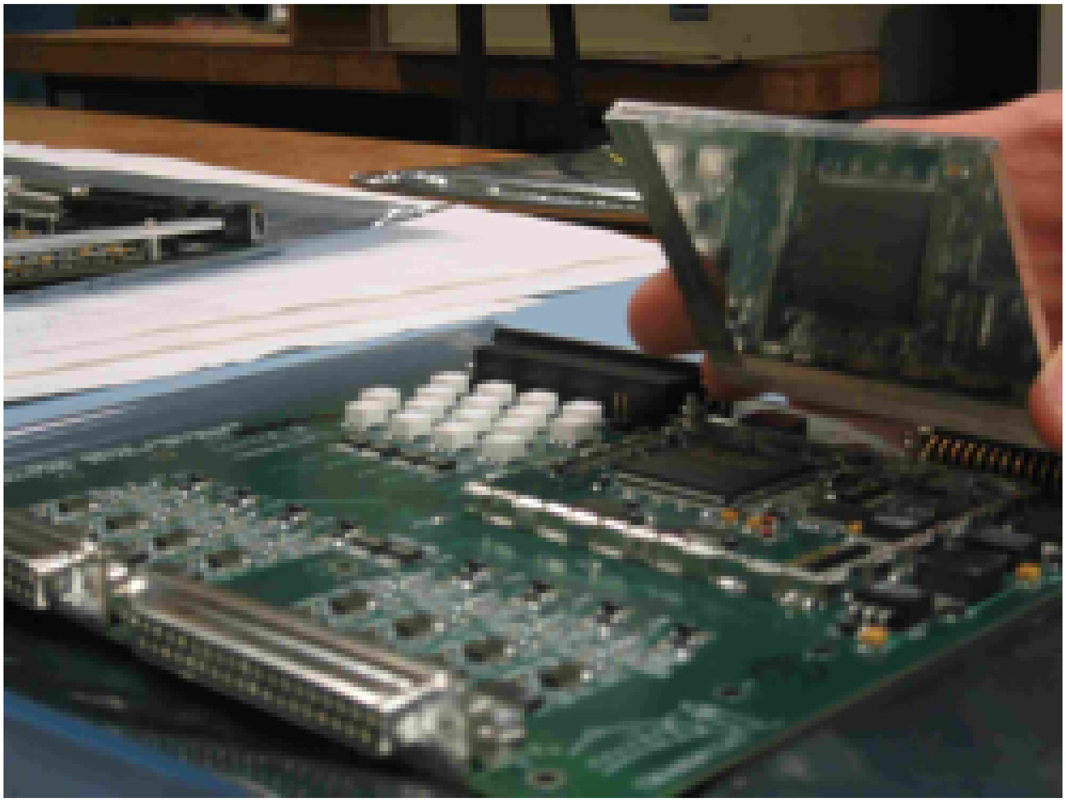

Figure 5.8. SQUID controller cards. Each SQUID controller corresponds to one SQUID card. The digital components are housed in an RF shield to avoid noise pickup by the analog components.

Oscillator-Demodulator Boards

A second set of warm readout boards is responsible for generating the bias and nulling combs, and for demodulating and digitizing the output signals. Each of the 60 oscillator-demodulator boards is responsible for 14 detectors. Since the demodulation and digitization scheme recovers only one component of the detector output, an additional oscillator-demodulator chain is provided for each set of seven to serve as an orthogonal-phase "helper channel" when necessary. Thus, 16 oscillator-demodulator chains are provided on each board.

The fMUX readout electronics are designed to be used in both non-multiplexed and multiplexed systems, so the oscillator-demodulator boards can be reconfigured to operate 16 non-mulitplexed bolometers attached to 16 SQUID arrays. In this mode, which was used for the APEX-SZ engineering run, each oscillator-demodulator board has two daughter SQUID controllers. Multiplexed operation requires a factor of eight fewer SQUIDs, so for the SPT, 12 boards have SQUID controllers that power eight arrays and another six have SQUID controllers that power four. In non-multiplexed mode, each of the 16 chains has two outputs: a post-demodulator (AC) signal[10]; and a pre-demodulator (DC) signal low-pass filtered at frequencies much less than the carriers, which is used to monitor the SQUIDs for flux jumps. Multiplexed operation reduces the number of outputs to 16 AC channels (14 bolometers and two helpers) and two DC channels (one per SQUID array).

As with the SQUID controller, a FPGA is used to command the configurable components on the oscillator-demodulator boards. These components include the DDSes, potentiometers that attenuate the bias and nulling combs, the signal digitization chain, switchable bias and nulling gain resistors, another switchable gain for the demodulator output, and others; the FPGA also provides a mechanism for communications with the SQUID controllers. The boards communicate with the receiver control computer via a bidirectional RS485 serial interface using the Modbus[11] protocol, and commuicate with each other, the SQUID controllers, and the DIO using low-voltage differential signaling (LVDS).

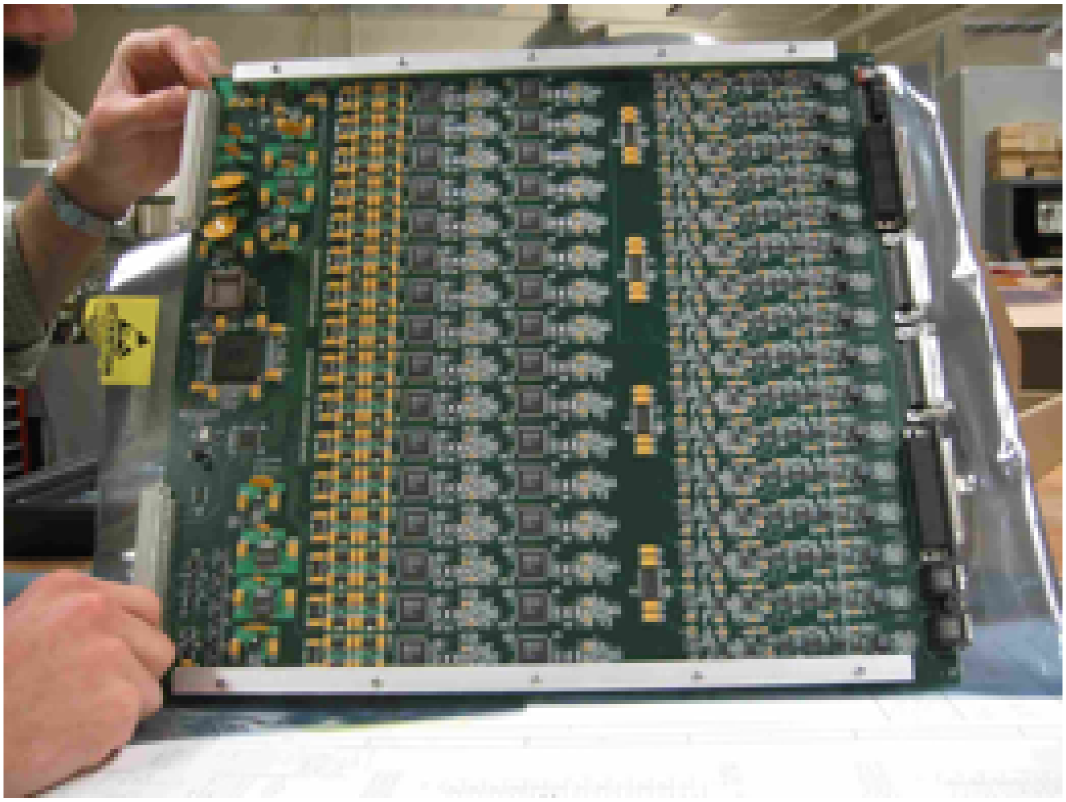

Figure 5.9. An oscillator-demodulator board. The 16 chains (14 detectors plus two helpers) run horizontally across the board.

---

[10] No provision is provided to measure the orthogonal phase of the output in non-multiplexed operation.

[11] `http://www.modbus.com`

Crates, Clocks, and Power

The oscillator-demodulator boards are housed in VME crates located in the receiver cabin, and shielded cables—two per oscillator-demodulator board and one per SQUID controller board—run from the boards up to the cryostat. Each of the three VME crates contains 20 oscillator-demodulator boards plus another board that distributes the clock signals. In total, the system dissipates about 3 kW of power during normal operation—49 W per oscillator-demodulator board, and 5 W per SQUID controller. A new all-digital generation of the fMUX electronics, developed at Berkeley and McGill University, utilizes fast ADCs and FPGAs in place of the power-hungry DDS chips. In addition to reducing power consumption by an order of magnitude, the digital fMUX has a number of operational enhancements, and is expected to be used for future SPT receivers.

In total, the warm components of the SPT readout system consist of 18 SQUID controllers and 60 oscillator-demodulator cards, which are responsible for controlling 120 SQUIDS and a maximum of 840 bolometer channels. Just in terms of the sheer number of components, the SPT receiver is a step up in complexity from previous generations of CMB instruments; the relatively intricate tuning requirements of the TES bolometers and SQUID arrays add further complications. The receiver control system described in the next chapter was designed to make these problems tractable.

Chapter 6

Receiver Control and Operation

The SPT receiver control system is responsible for monitoring and operating the SQUIDs, bolometers, sorption fridge, and readout boards. In order to efficiently manage the 960 AC readout channels (840 bolometers plus 120 helpers) and 120 DC channels (120 SQUIDs), it must be highly optimized. It also must provide a well-defined interface both to users and to the SPT telescope control system. Since it is also utilized for laboratory testing, the software must be flexible and poweful enough to handle a wide range of user demands. Finally, it must be sufficiently automated during normal operations so as to place few demands on observers.

The suite of software that handles these tasks was written over the course of several years by APEX-SZ and SPT collaborators. Its structure is straightforward: daemons written in C++ mediate all communications with the hardware, and a set of Python objects provides a scriptable interface. High-level operations are performed by scripts, while low-level tasks—as well as certain common and highly-optimized algorithms—are performed by the daemons. With the exception of timestream data transfer, all inter-process communication takes place via XML over TCP sockets. The software can be split across multiple machines, but in practice, all of it runs on a single board computer under Linux.

Its structural simplicity notwithstanding, the receiver control system is functionally complex, with various interdependent units performing a wide variety of tasks. In this chapter, I will describe these components and their interaction, and will also explain how the system was refined to improve the performance of the SPT. The technical details of the Hardware Manager Daemon, the Fridge Daemon, and their scripting interfaces—which may be of interest to future observers—are relegated to Appendix A.

6.1 Receiver Control System

6.1.1 Overview

The SPT software architecture is outlined in Figure 6.1. The telescope control system, based on software written for the Sunyaev-Zel'dovich Array (SZA), is responsible for commanding and monitoring the instrument subsystems and storing the data. Each subsystem is managed by its own software, which is responsible for executing commands from the control system and for collecting and distributing relevant data. From the telescope control system perspective, the receiver is just another subsystem, albeit a relatively complicated one.

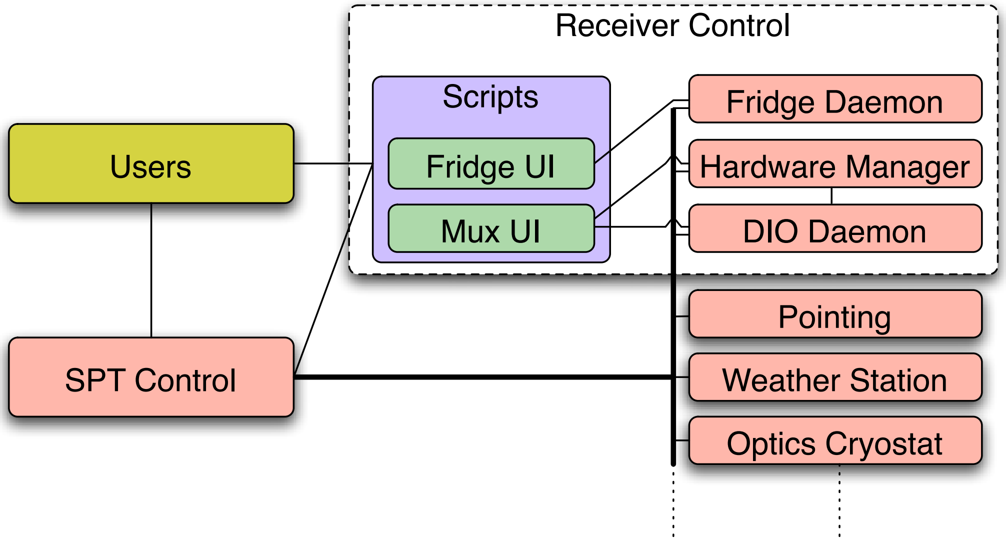

Figure 6.1. The SPT software architecture. The SPT control system maintains a link to each telescope subsystem, including the receiver. Users interact with the subsystems via the control system, and can also interact with the receiver directly via the scripting interface.

At the most basic level, the receiver control system simply issues commands to, and reads data from, the hardware: the SQUID controller and oscillator-demodulator boards, and the sorption fridge controller electronics. The sorption fridge controller receives commands via a DIO and outputs data via an analog-to-digital converter (ADC); the oscillator-demodulator boards and SQUID controllers receive commands and return data via a serial interface, and output timestream data via a seperate high-speed DIO. Though there are 60 oscillator-demodulator boards in three VME crates, and 18 SQUID controller cards, only one serial port is used for the entire readout system. The oscillator-demodulator boards are addressed over the serial line using the Modbus protocol, and the SQUID controller board communication is mediated by the oscillator-demodulator boards. We use a fast RS485 serial connection, but this link still represents a significant bottleneck in the system.

Inside the receiver control software, each piece of hardware corresponds to a C++ object of the appropriate class—a SQUID controller board corresponds to a SquidController object, a thermometer to a Thermometer object, and so on. In some cases, subcomponents of the hardware are split off into their own subclasses—each SQUID controller, for example, has eight SquidChannel objects. This structure makes the code modular and reusable, so that if one component of the hardware is changed or upgraded, only its corresponding class needs to be revised.

All of the C++ objects representing the receiver hardware are instantiated by daemons running on the receiver control computer. These daemons act as gatekeepers to the hardware—anyone needing to control the receiver, or to access receiver data, must send requests to the daemons over TCP/IP sockets. Three programs split up the job:

- the fridge daemon is responsible for the sorption fridge and the housekeeping thermometry,
- the DIO daemon is responsible for the AC and DC timestream data,
- and the hardware manager daemon is responsible for the oscillator-demodulator and SQUID controller boards.

The DIO daemon was written by Martin Lueker, and I wrote the other two. All three can operate without the presence of the telescope control system, as is necessary in the lab.

Each of the daemons has a single TCP port over which it accepts connection requests. Once a daemon has received a request, it sets up a dedicated TCP port for communications with the requesting client, over which commands and data are then sent. Most of the TCP communications take place via XML-formatted commands and responses. The exception is the DIO daemon, which moves too large a quantity of data for XML to be practical. Clients requiring timestream data initially request a data connection to the DIO daemon via an XML command, but subsequently receive the requested data in a compact binary format.

Since XML commands and responses are cumbersome for users to deal with directly, we provide a powerful scripting interface written in Python. Most of the C++ hardware objects have lightweight Python counterparts, which simply construct commands for the daemons and parse their responses. Higher-level functionality is also provided, as is a graphical user interface for use in laboratory testing. Over the years, a collection of Python and shell scripts has been developed to make use of these interfaces. Except for a handful of routines that were implemented in C++ for optimization, most of the day-to-day receiver control logic is implemented at this level. Offloading this logic into scripts ensures that the daemons need not be recompiled and restarted every time the receiver tuning process changes.

6.1.2 Daemons

Hardware Addressing

One of the most fundamental tasks that the receiver software must handle is the identification and addressing of the receiver hardware resources. Each bolometer has a serial number, a focal plane location, a readout chain, and a SQUID associated with it; and some mechanism must be provided for users to configure and command all of these components. The addressing scheme used in the SPT receiver is outlined in Figure 6.2. Within the Hardware Manager daemon, three sorts of identifiers are stored—serial numbers, physical locations, and logical readout addresses—and commands are available to translate between them.

The serial numbers of the bolometers, SQUIDS, and readout boards are all stored in XML configuration files. The numbering schemes for the SQUIDs and readout boards are straightforward. The bolometer serial numbers encode information about the wedge and the pixel location: each wedge has an identifying string (X1, for example), each chain of eight detectors is identified by a letter (A-T), each detector is assigned a number within its chain (1-8), and the serial number is constructed from these components (for example, X1(A1)). Since the layout of the bolometers is fixed from wedge to wedge, detectors with the same letter and number (e.g. A1) are always at the same physical location relative to the center of the wedge. An XML file called WedgeMap_SPT records the correspondence between the pixel locations and names.

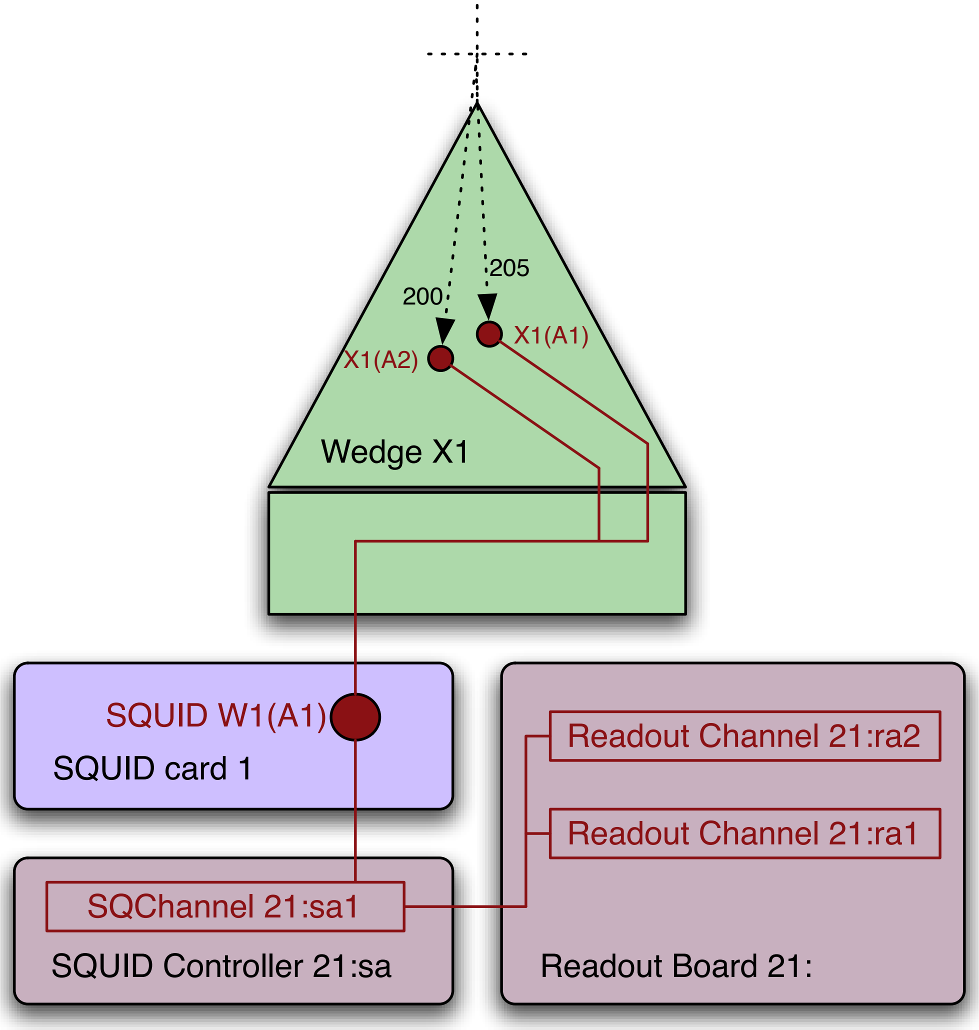

Figure 6.2. Resource addressing in SPT. Each pixel location on the focal plane has a number associated with it, and each bolometer has a serial number. The readout components have addresses associated with them, and the correspondences between pixels, bolometers, and readout components are handled by the Hardware Manager.

A second set of configuration files, one per wedge (Wedge-X1, for example), specifies the resonant frequencies corresponding to each bolometer. The same file also specifies the physical position of the wedge on the focal plane, allowing a correspondence to be made between bolometer serial numbers and focal plane position. The possible bolometer locations on the focal plane each have an integer (0-959) associated with them, and timestream and configuration data are indexed by this integer in the archive.

The correspondence between bolometers and readout hardware is determined by yet a third configuration file, this one called HardwareMap. Within this file, and throughout the rest of the software, the readout hardware resources are identified by strings in the form *modbus address:channel address*. The modbus addresses are two-digit hexidecimal numbers—one per oscillator-demodulator board—and the channel addresses specify a specific readout channel or SQUID controller channel associated with the board. An oscillator-demodulator board has two sets of eight readout channels (ra1-ra8, rb1-rb8) and communicates with up to two SQUID controllers managing up to 8 SQUIDS each (sa1-sa8, sb1-sb8). As an example, in order to issue a command to the third SQUID managed by controller A attached to oscillator-demodulator board 0x21, one would use the address *21:sa3*.

Data Management

Other than the timestream data, each value that finds its way to the data archive is represented by the telescope control system as a "register." The FPGAs on the oscillator-demodulator boards actually do have registers (for gain settings and the like), but in other pieces of hardware, the notion is purely abstract. The low-level objects in the receiver control system provide this layer of abstraction by associating register addresses with all values that can be set or read out, and by providing a GetAllRegisters method that returns a list of these addresses and values. The telescope control system periodically issues this command and stores the response in the data archive.

Most of the registers in the receiver control system change only rarely, and communication with the hardware is slow and can introduce noise into the timestreams. Register values are therefore cached by the daemons where possible. In the special case of the fridge controller thermometry values, the daemon maintains a cache that updates periodically in the background.

In the scripting interface, users need not keep track of register addresses or obscure hardware byte codes, as the Python objects have usefully-named data members that can be refreshed and interpreted on command. Similarly, among the first steps in all of the various data archive readers is the conversion of register values to sensible units and of register addresses to useful names.

Conflict Resolution

In principle, multiple users can simultaneously send commands to the same readout hardware address, introducing the potential for resource conflicts. The serial communication line is protected by a mutex in order to prevent collisions at a low level, and a locking mechanism gives users exclusive access to specific resources. Since resource conflicts seldom occur once the receiver is installed on the telescope, the locking mechanism is disabled for convenience in the version of the software running at the South Pole.

Commands and Algorithms

Most of the communication between clients and the hardware manager and fridge daemons comes in the form of commands and responses. In keeping with the philosophy that runtime logic should be implemented in scripts, these commands are very low level: set or get a register value, power up a component, reset a board, etc. Internally, commands are represented as minimalistic objects that are instantiated for each connection, and that define a method that is executed upon request. All of the command classes inherit from a single command base class with helper functions to deal with argument parsing and the like, so implementing a new command is relatively straightforward. A list of hardware manager and fridge daemon commands is provided in Appendix A.

The hardware manager daemon also accepts requests to run more complicated sets of code, which are referred to internally as algorithms. Like commands, all algorithms inherit from a single base class, and each algorithm defines a startup, execute, and cleanup method. The execute method often consists of high-level code that would ordinarily be implemented in scripts, but that can be run more efficiently from within the daemons. Typical examples include network analyses and bolometer I-V curves performed in parallel on multiple channels.

6.1.3 Scripting Interface

The scripting layer of the receiver control system consists of two libraries of Python objects, a set of Python scripts that use these objects to perform certain tasks, and a handful of “wrapper” shell scripts.

Libraries

The Python library that provides the interface objects for the readout system is called MuxUI, and the simpler interface to the sorption fridge and receiver housekeeping is called FridgeClient. In the former, interface classes are provided for the entire readout system (implementing global commands), the oscillator-demodulator boards, the SQUID channels, the readout channels, and vectors of channels; the fridge scripting library provides just one object corresponding to the controller box. Since the scripting layer operates at a higher level of abstraction, the object heirarchy is simpler and less comprehensive than in the daemons. Vectorized objects are offered because they simplify coding, and because they reduce the amount of network traffic by bundling multiple commands into one block of XML. A set of utility functions is also provided to automate common tasks.

The readout and fridge objects contain both data members and methods. When an object is instantiated, the data members are not filled automatically; neither are the data members updated when the hardware values change. Users must explicitly call the object’s fetch_values method in order to initiate the necessary data transfer. This is done in order to avoid unnecessary hardware access, and to ensure that the daemons do not get bogged down attempting to communicate with unresponsive clients. Most of the methods in the scripting library objects have a one-to-one correspondence with commands and algorithms implemented in the daemons, but the readout objects also have the capacity to contact the DIO and obtain (usually small) chunks of timestream data.

Scripts

The readout and fridge scripts range from simple (e.g. lookup_addr gets the readout address corresponding to a bolometer ID number) to complex (cycle_season3 sets up the receiver in preparation for observations, using the logic developed for the 2009 focal plane). Most are written in Python, but a handful require extensive file manipulation and are therefore implemented as shell scripts. The graphical user interfaces for the readout system, and the text-based command interface for the sorption fridge and housekeeping, are in principle no different from the other scripts. Most of the scripts start by creating the necessary set of objects and fetching the required values from the daemons. They then perform their task, and write any output to the console and to a data log directory.

Execution

Though the scripts may be called directly by users logged into the control computer (as is done in the lab), the preferred method is to initiate them through the telescope control system via a secure shell (ssh) session. This allows the script name, the time stamp, and any errors or output to be stored in the main system logs. A simple protocol is used to transmit error, status, and output messages back to the control system for logging: the messages are written to the standard error stream along with header information, and the telescope control software uses the headers to redirect the messages to appropriate log files. A list of commonly-used scripts and a description of the receiver-control system protocol are provided in Appendix A.

6.2 Operating the SPT Receiver

Most of the readout and fridge scripts are used exclusively for debugging, testing, and characterizing the receiver. Only a handful are necessary during normal operation, and most of these are straightforward (e.g. change the demodulator gain setting, fine tune the carrier nulling, and so on). The exception is the receiver setup script, which is responsible for cycling the fridge, tuning the SQUIDs, biasing the bolometers, and preparing for observations. The details of this setup routine have a significant impact on the duty cycle and performance of the receiver.

6.2.1 Receiver Setup

The receiver setup routine is outlined in Figure 6.3. Once the sorption fridge 3He cycle ends and the cold stage temperature starts rising, the observer parks the telescope at a $\sim 45^\circ$ elevation angle and launches the receiver setup script. It begins by executing fridge commands that initiate the sorption fridge 4He cycle. While the 4He cycle is in progress, the script proceeds with the receiver setup. During the first stage of this process, the oscillators and first stage amplifiers are turned off and the flux-locked loop is opened—all of the readout hardware is essentially deactivated so that there is no flux running through the SQUID input coil. The SQUIDs are then heated to remove trapped flux, and are given ~ 15 minutes to return to base temperature. Once this time has elapsed, the first stage amplifiers are powered back on and the SQUIDs are tuned.

The SQUID tuning algorithm begins by applying a nominal current bias to the SQUIDS, measuring the V-Φ response, and picking out the points that correspond to $n\Phi_0$ and $n\Phi_0/2$.

Once these flux bias points have been identified, the SQUID I-V response is measured at both points, and the current bias is set to the level at which the difference between the I-V response curves is the greatest. Another V-Φ response measurement is used to pick out the optimum flux bias (near $3\Phi_0/4$). In order to speed the tuning process, the response curves are measured simultaneously on all SQUIDs, so that the voltages can be measured concurrently. Once the SQUID current and flux bias levels are set, the amplifier offsets are zeroed and the flux-locked loops are closed.

After the SQUIDs are set up, biases are applied to the bolometers in order to keep them in the normal regime once the focal plane cools to base temperature. Since the SQUID dynamic range would be exceeded by seven un-nulled carriers, this step can be only partially parallelized. The bolometers are divided into eight groups based on the last digit of their readout addresses, so that a maximum of one detector per readout chain is in each group. The first group is then biased and nulled in parallel, followed by the second group, and so on.

During the SQUID tuning and biasing, the script periodically checks to see if the 4He cycle is complete. If it is, the tuning process is aborted and restarted once the 3He cycle has begun. This ensures that the 3He pumps are never left hot for a long period of time while the 4He cycle is complete, which could compromise the 3He hold time. Fortunately, the SQUID tuning and biasing routines are fast enough that they consistently are able to finish during a typical 4He cycle.

After the bolometers are biased, the setup script waits for the 4He cycle to end, at which point the 3He pumps are cooled and the cold stages are allowed to drop to base temperature. Due to the heat capacity of the focal plane, this process takes about two hours.

Once the base temperature is reached, the telescope is moved to an elevation angle near that at which observing will take place. The thermal and optical loading conditions can change depending on the receiver cabin temperature, the elevation angle, and atmospheric conditions; consequently, the detector operating points are re-determined each day under the appropriate loading conditions. This is done by measuring the bolometer I-V response up to the point where the desired R/R_n (a proxy for bolometer loop gain) is achieved. The same parallelization scheme used in biasing the bolometers normal is implemented at this step, and the carriers are re-nulled after each group has been biased. When the biasing is complete, the demodulator gains are set to a higher level. This ensures that the digitization step does not result in any loss of information, at the expense of reducing the range of currents that can be read out. The carrier nulling is then fine-tuned to bring the demodulator outputs away from the rails, and any ill-behaved readout chains are disabled. At this point, the receiver is ready to begin observing.

6.2.2 Normal Observing

During normal observing, the receiver requires little intervention: the carrier nulling is fine-tuned on approximately an hourly basis, and the detectors and temperatures are monitored for problematic behavior. If any bolometer drops below its transition and begins superconducting, its entire readout chain is disabled, as the slews and oscillations in a low-impedance loop can lead to elevated noise in other readout chains. In rare cases, changes in loading conditions can necessitate the re-biasing of the bolometers. If the fridge temperatures begin to rise before the 3He cycle ends, it is usually a sign that a power event has occurred and that intervention by the observer is required.

A set of automatic data processing tools is used to monitor receiver performance from cycle to cycle. These tools create web pages which provide an overview of detector "liveness," fridge temperatures, and so on, so that observers can watch for trends in performance. For example, the slow buildup of contamination in the pulse tube cooler can lead to a rise in main plate temperatures over a period of many weeks, requiring the pulse tube cold head to be purged and refilled on rare occasions. With the exception of such occurrances, the performance of the system has remained remarkably stable through the 2008 and 2009 seasons.

6.2.3 Refinement and Optimization

In order to achieve this operational stability, we made a number of improvements to the receiver control system as originally designed. The lessons that we learned in the refinement and optimization process have led to gains in recieiver performance, and have informed the development of the readout electronics that will be used for future SPT receivers.

I/Q Output

Since the bolometer bias voltages are AC, the output currents have both in-phase (I) and out-of-phase (Q) components. During the design stage of the fMUX electronics, it was believed that phase shifts in the system would be small, and so the boards were only given the capacity to read out the I component of the demodulated signals. Our belief turned out to be mistaken for two reasons. First, the phase shifts due to the warm electronics and to cold stray inductances are larger than expected. Second, the bias voltage at a given detector's resonant frequency also sends small but non-negligible currents through the other resonators in the readout chain, which are off-resonance and thus mostly reactive. The combination of these two effects results in phase shifts that depend on both the carrier frequencies and the operating resistances of the bolometers.

Two techniques were developed to deal with this issue. In the first, two oscillators on a given board are locked 90° out of phase with each other, allowing the corresponding demodulator channels to recover both the I and Q outputs. This technique is useful only when the stage temperature is above T_c, since the phase locking process requires that the bias voltage briefly be turned off. If the cold stage is below T_c, the pause in the bias will often allow the bolometer in question to enter its superconducting state. Since no power can be applied to an $R = 0$ bolometer, a large optical load or a burst of heat must be applied to the detector in order to bring it back into its transition. The SPT system has no provision for reliably providing the former, and the latter is far too time-consuming to be practical.

The second technique does not allow both components to be recovered, but instead provides a way to measure the amplitude ($\sqrt{I^2 + Q^2}$), which is often the most relevant quantity. The amplitude of the signal on a given bolometer can be determined by operating a second DDS at ~ 0 amplitude[1], and at a frequency $f + \Delta f$ slightly offset from the carrier frequency

---

[1] Some small amplitude must be set in order to fire the demodulator, but with the appropriate settings, the resulting voltage across the bolometer can be made negligible.

f. The beating of the two frequencies will produce a signal in the second demodulator output at frequency Δf with an amplitude corresponding to the bolometer current. Since this technique does not require phase locking, it can be used even when the focal plane is at base temperature.

We find that measurements of the I and Q components—or at least of the amplitude—are necessary to determine the resonance frequencies, to interpret the bolometer I-V curves, and to null the carriers at an acceptable level. Unfortunately, both of our techniques require a second "helper" oscillator-demodulator channel, which restricts each 16-channel oscillator-demodulator board to operating 14 detectors and two helpers. In principle, this reduces the maximum number of pixels on the SPT focal plane by a factor of 7/8—from 960 to 840. The cost is somewhat lower in practice, since few wedges have perfect detector yield. Nevertheless, the the next generation of the fMUX readout electronics was designed with the ability to measure both components without sacrificing potentially useable detectors.

Carrier Frequencies

The phase shifts and leakage currents in the system also introduce some ambiguity into the choice of bolometer bias frequencies. First, care must be taken in order to find the frequency that is on resonance for a given bolometer RLC resonator, as leakage currents through adjacent channels can shift the peaks in the network analysis. Second, a balance must be struck between putting the carrier directly on resonance—which maximizes the amplitude of the current and tunes out the cold phase shifts—versus putting the carrier at the frequency that maximizes the demodulator response. Until recently, we generally opted for the former, since the bolometers have the truest voltage bias directly on resonance; current biased TES bolometers are unstable because they are under positive feedback, and introducing even a small component of current bias can negatively impact detector stability. The higher time constants of the 2008 and 2009 detectors offer us the chance to compromise on this point, and efforts are underway to find the optimum balance.

Nuller Leakage Current

Another subtlety in the fMUX system involves the nulling comb. The nuller currents for a given set of detectors are fed directly into the SQUID input coil, but have two parallel paths to ground: through the input coil, or through the bolometers and bias resistor. If the input impedance of the SQUID were truly zero under shunt feedback, all of the current would follow the former path. In reality, the SQUIDs have some small input impedence (since the loop gain of the flux-locked loop is finite), and the currents are divided between both paths. Consequently, the carrier nulling reduces the bolometer bias powers by feeding current through the resonators that are 180° out of phase with the carriers.

This presented a serious problem for the 2007 detectors, which were only stable and responsive over a narrow range of bias powers. We increased the SQUID loop gain as much as possible, but eventually the gain at high frequencies—where the phase shift is large—approached one, resulting in oscillations that required that the loop gain be cut back down. The bolometers therefore had to be biased slightly above the desired operating point so that they behaved properly after nulling. This issue became essentially moot once we deployed detectors that were stable over a wider range of bias powers, but this effect must nevertheless be taken into account if the detector operating points are to be determined precisely.

Bias Schedules

Since TES bolometers are highly responsive over a narrow range of temperatures, the amount of bias voltage applied to the detectors must be chosen wisely to maximize responsivity, stability, and dynamic range. We had originally hoped that the detectors could be biased to the same voltage after every fridge cycle and left to operate at that bias throughout the observing day. Instead, we find it necessary to re-measure the I-V characteristics of the bolometers after every cycle. These measurements allow us to choose biases that situate the detectors near a specified value of R/R_n, which we find to be a good proxy for the loop gain. In 2007, this was necessary because even small changes in loading could move some detectors into an unstable regime. Subsequent detectors were more stable, but were also more responsive—due to their lower G values, small changes in loading translated into larger changes in operating temperature. The bias schedule for a given observing day is therefore determined using measurements under actual loading conditions.

Detector properties tend to be relatively constant across a given wedge, so we assign a default operating point—usually around $0.8R_n$—to each bolometer based upon its wedge. We then iterate on a list of exceptions to these default values, increasing the fraction of R_n for unstable detectors and decreasing it for less-responsive detectors. The level of voltage required to hold each bolometer in its normal regime is handled similarly. During the receiver setup process, the setup script consults the lists of exceptions to formulate normal and operating bias schedules. The fine-tuning of these schedules led to significant gains in detector yield and responsivity in 2007 (see Section 4.3.1), and incremental gains in 2008 and 2009.

Receiver Setup Optimization

Since our bolometers and SQUIDs must be re-characterized during every round of receiver setup, the measurement process must be optimized in order to maximize the receiver duty cycle. The SQUID I-V and V-Φ curves are all measured in parallel, which saves time by simultaneously sampling from the DIO for all channels. This speeds up the SQUID tuning process enough that it can be completed during the relatively brief 4He cycle, which would have otherwise been dead time for the receiver. Since most readout chains have only a single helper channel to assist in bolometer I-V curves and carrier nulling determinations, the bolometers cannot all be set up in parallel, but must instead be broken up into at least seven groups. Even this partial parallelization yields a significant increase in speed.

A useful figure of merit for the setup process is the amount of time taken up by SQUID and bolometer tuning that could otherwise have been spent observing. Our optimizations reduced this time from about 2.5 hours in early 2007, to about 0.5 hours in 2009. Upgrades to the receiver cryogenics—including the switch from the PT410 to the PT415 pulse tube cooler—have also increased the hold time of the sorption fridge from $\sim$ 24 hours in 2007 to $\sim$ 36 in 2008 and 2009. The cumulative improvements in duty cycle and hold time have increased the observing efficiency of the SPT by nearly a factor of two.

6.2.4 Status

In this chapter and the three preceeding it, I have described the design, implementation, and operation of the South Pole Telescope and its SZ receiver. By the end of the 2009 observing season, the instrument will have been used to survey over 800 $\deg^2$ to 18μK r.m.s. (or better) per arcminute pixel at 150 GHz. The survey fields have also been mapped to variable depths at 95 GHz and 220 GHz. The first four of what will be many serendipitously-detected galaxy clusters have been published in Staniszewski et al. [2009]. The receiver now consists of ~ 700 stable, sensitive detectors operating in three bands, and will continue to be improved as the SZ survey continues.

In the next chapter, I will discuss a series of targeted cluster observations that complement the survey data, and that can be used to study both cosmology and cluster physics.

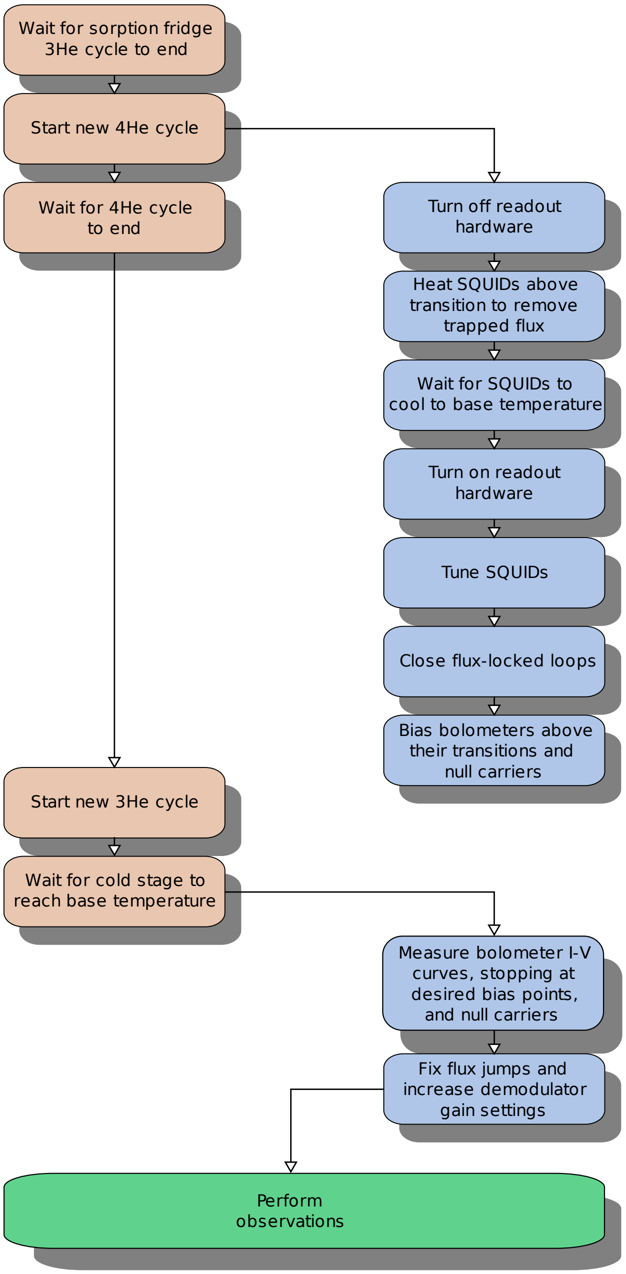

Figure 6.3. Outline of the receiver setup process.

Chapter 7

Cluster Observations

As discussed in Chapter 2, galaxy clusters are the largest known gravitationally collapsed objects. They are believed to have taken nearly a Hubble time to form, and their abundance as a function of redshift is crucially dependent on the composition and expansion history of the universe. A sufficiently large and well-understood sample of galaxy clusters can therefore be used to constrain cosmological models. Several survey campaigns using a variety of techniques are currently underway. Precision measurements of individual clusters can be used to study the mass-observable relations of these surveys, as well as to study the structure of the intra-cluster medium (ICM).

In this chapter, we describe a set of deep SZ cluster observations at 150 and 220 GHz undertaken with the South Pole Telescope (SPT) during the austral winter of 2008. Data from the 150 GHz band are used to measure the thermal SZ signal, and concurrent data from the 220 GHz band—which is near the thermal SZ null—are used to reduce the effect of astrophysical contamination. The 220 GHz data are too noisy to allow a detection of the kinetic SZ effect, so in this analysis we focus exclusively on the thermal SZ effect.

Of the 13 highest-luminosity REFLEX clusters [Böhringer et al., 2004] in the range of elevation angles accessible to the SPT, 11 make up the primary sample for this work; a supplemental sample of four additional clusters is also included. Both samples are listed in Table 7.1. Taking advantage of the SPT's wide field imaging capabilities, we make a model independent estimate of the radial profiles of each cluster and place constraints on the integrated pressure out to large radius. We also fit the profiles both to the $\beta-$model and to the generalized NFW model proposed by Nagai et al. [2007] (hereafter the GNFW model). Using a stacked analysis, we estimate the slope of the pressure profile in the cluster outskirts. Finally, we estimate the integrated y parameters for each cluster and compare to X-ray results.

7.1 Observations, and Data Reduction

7.1.1 Observations

The clusters discussed in this work were observed using constant-elevation scans, which entail sweeping the telescope at constant angular velocity in azimuth across the field and back, stepping in elevation, and repeating. This observing strategy is similar to that described in Staniszewski et al. [2009], but over a much smaller field—approximately 1 deg^2. The azimuthal scan speed is set such that $\sim 0.25°$ on the sky is scanned in one second, and each elevation step is 0.005°. A complete set of scans across the entire region, which we refer to as one observation, takes approximately 55 minutes to complete. The observations are then combined to produce a single map in each band for each field. The inner region of each 150 GHz map, approximately 0.5° by 0.5° on the sky, has even coverage to within 10%. Coverage is less uniform at 220 GHz due to the spatial distribution of the detectors on the focal plane.

One of the clusters in the primary sample, AS 0520, overlaps with the survey field described in Staniszewski et al. [2009]. We reprocessed the 2008 150 GHz and 220 GHz survey data with filtering equivalent to that described in Section 7.1.2, and split the survey data into subsets, each with a weight per pixel equal to that of the targeted observations. This allows the survey data to be treated in a similar manner to the data from the targeted observations for the purposes of calculating noise estimates. Adding the survey data effectively doubles the number of targeted observations of this cluster.

Between individual observations, we perform a series of short calibration measurements described in more detail in Carlstrom et al. [2009]. These include measurements of a chopped thermal source, $\sim 2°$ elevation nods, and scans across the galactic HII regions RCW38 and MAT5a. This series of regular measurements allows us to identify detectors with good performance, assess relative detector gains, and monitor atmospheric opacity.

Table 7.1. Summary of cluster sample.

ID	R.A.^{a}	decl.^{a}	z	REFLEX L_X (10^{44} erg/s)	T_e (keV)	$M_{\rm gas}$ ($10^{14} M_\odot$)	Ref.^{b}
Primary Sample							
A 2744	$0^h14^m18.6^s$	$-30°23'15.4''$	0.307	12.92	10.1 ± 0.3	1.0 ± 0.2	Zhang et al. [2006]
RXCJ0217.2-5244	$2^h17^m12.6^s$	$-52°44'49.2''$	0.343	12.03	10.9^c	-	Böhringer et al. [2004]
RXCJ0232.2-4420	$2^h32^m18.8^s$	$-44°20'51.9''$	0.284	9.65	7.0 ± 0.3	0.9 ± 0.2	Zhang et al. [2006]
AS 0520	$5^h16^m35.2^s$	$-54°30'36.8''$	0.294	13.87	7.5 ± 0.3	0.8 ± 0.2	Zhang et al. [2006]
RXCJ0528.9-3927	$5^h28^m52.5^s$	$-39°28'16.7''$	0.284	13.12	7.2 ± 0.4	0.9 ± 0.1	Zhang et al. [2006]
AS 0592	$6^h38^m46.5^s$	$-53°58'18.0''$	0.222	10.62	8.0 ± 0.4	-	Hughes et al. [2009]
A 3404	$6^h45^m30.0^s$	$-54°13'42.1''$	0.164	7.36	8.1 ± 0.3	0.9 ± 0.1	Zhang et al. [2008]
1ES 0657-56	$6^h58^m30.2^s$	$-55°56'33.7''$	0.297	23.03	10.6 ± 0.2	1.8 ± 0.3	Zhang et al. [2006]
RXCJ2031.8-4037	$20^h31^m51.5^s$	$-40°37'14.0''$	0.342	12.04	10.9^c	-	Böhringer et al. [2004]
A 3888	$22^h34^m27.1^s$	$-37°44'7.5''$	0.151	7.31	7.8 ± 0.4	0.8 ± 0.1	Zhang et al. [2008]
AS 1063	$22^h48^m44.9^s$	$-44°31'44.4''$	0.346	30.79	11.1 ± 1.1	1.2 ± 0.1	Maughan et al. [2008]
Supplemental Sample							
RXCJ0336.3-4037	$3^h36^m18.7^s$	$-40°37'20.0''$	0.173	2.53	7.2^c	-	Böhringer et al. [2004]
RXCJ0532.9-3701	$5^h32^m55.9^s$	$-37°1'34.5''$	0.275	6.94	9.5 ± 0.4	0.6 ± 0.1	Zhang et al. [2006]
MACSJ0553.4-3342	$5^h53^m27.2^s$	$-33°42'53.0''$	0.407	-	13.1 ± 3.2	-	Cavagnolo et al. [2008]
A 3856	$22^h18^m39.9^s$	$-38°53'43.6''$	0.141	3.78	6.7 ± 0.2	0.5 ± 0.1	Zhang et al. [2008]

[a] R.A. and decl. are the right ascension and declination angles of the cluster X-ray centroid.

[b] R.A., decl., redshift, and electron temperature T_e are taken from these papers and references therein. REFLEX luminosities are from Böhringer et al. [2004].

[c] For the clusters without published X-ray temperatures, T_e was estimated using a scaling relation from luminosity [Markevitch et al., 1998].

Table 7.2. Summary of SPT cluster maps.

ID	R.A.[a]	decl.[a]	Observing time (hours)	150 GHz Depth[b] (μK_{CMB})	220 GHz Depth[b] (μK_{CMB})
Primary Sample					
A 2744	$0^h14^m16.8^s$	$-30°23'22.2''$	6.83	12.3	36.2
RXCJ0217.2-5244	$2^h17^m13.3^s$	$-52°44'49.5''$	8.32	11.5	40.8
RXCJ0232.2-4420	$2^h32^m16.5^s$	$-44°21'15.5''$	10.46	9.2	32.6
AS 0520	$5^h16^m35.4^s$	$-54°30'19.3''$	18.48[c]	10.3	17.4
RXCJ0528.9-3927	$5^h28^m52.0^s$	$-39°27'57.6''$	5.23	14.1	39.4
AS 0592	$6^h38^m46.1^s$	$-53°58'31.3''$	8.32	18.9	70.7
A 3404	$6^h45^m29.3^s$	$-54°13'20.0''$	5.54	14.5	46.5
1ES 0657-56	$6^h58^m29.7^s$	$-55°56'38.2''$	12.59	7.9	22.5
RXCJ2031.8-4037	$20^h31^m51.1^s$	$-40°37'23.2''$	5.23	16.3	49.7
A 3888	$22^h34^m26.6^s$	$-37°44'57.9''$	5.23	15.4	42.6
AS 1063	$22^h48^m44.9^s$	$-44°31'43.1''$	12.21	10.3	29.7
Supplemental Sample					
RXCJ0336.3-4037	$3^h36^m16.5^s$	$-40°37'26.6''$	5.23	13.1	48.1
RXCJ0532.9-3701	$5^h32^m55.1^s$	$-37°1'40.8''$	10.46	12.8	38.1
MACSJ0553.4-3342	$5^h53^m24.5^s$	$-33°42'35.4''$	5.82	15.4	51.0
A 3856	$22^h18^m37.6^s$	$-38°53'54.8''$	8.72	11.0	34.9

[a] R.A. and decl. are the right ascension and declination angles where the average SZ decrement within a $1'$ radius is the largest.

[b] Depth is determined by the standard deviation of the jackknife maps smoothed with a Gaussian with FWHM=$1'$.

[c] AS 0520 maps include data from the 2008 5^h30^m survey, which effectively doubles the amount of targeted observing time. This value includes the factor of ~ 2.

7.1.2 Data reduction

The data reduction process used for this analysis is similar to the preliminary survey pipeline described in Staniszewski et al. [2009], with some minor differences noted below.

Data selection and filtering

The first step in the processing pipeline is to identify the data that will be included in each single-observation map. For every observation, a set of well-performing detectors is identified by applying a set of noise and sensitivity criteria. On average, 302 detectors at 150 GHz and 165 at 220 GHz pass this initial cut. The data are then divided into individual azimuth scans. 0.7% of scans have large instantaneous pointing offsets or data acquisition problems, and are omitted from further processing. A further set of selection criteria is then applied to detectors on a scan-by-scan basis (excluding, for example, data contaminated by cosmic rays). Data from detectors passing these cuts, an average of 291 detectors at 150 GHz and 162 at 220 GHz for each scan, are included in the final maps.

The receiver exhibits some sensitivity to the pulse-tube cooler used to cool it to ~ 4 K, resulting in occasional lines in the detector noise power spectra, so a small amount of bandwidth ($< 0.4\%$) is notch filtered out of the detector timestreams. The timestreams are further processed by deconvolving the effect of the detector time constants. We also low-pass filter at 25 Hz, well above the signal bandwidth.

For every scan, each detector's timestream is then fit simultaneously to a number of template functions, and the best fit to each template is subtracted out. This time-domain filter reduces the effect of low-frequency noise in the detector timestreams due to readout noise or to atmospheric fluctuations. For the analysis presented here, we use as our templates a second-order Legendre polynomial and a common mode constructed from the wedge-averaged timestreams, resulting in a characteristic filter scale of roughly one half degree. This light filtering is sufficient to remove much of the low-frequency noise, due in part to the outstanding atmospheric conditions at the South Pole.

The common mode template is constructed from the mean across all of the well-performing detectors in a given wedge using a nominal relative calibration. In Staniszewski et al. [2009], by contrast, the common mode template was constructed from the mean across the entire array for each band. Since the 2008 SPT receiver contains three 150 GHz and two 220 GHz wedges, the detectors in the two bands have significantly different distributions on the focal plane; thus the array common mode removes signals on different spatial scales for each band. Since the common mode templates for individual wedges are relatively similar to one another, the wedge common mode preserves signals on similar spatial scales for each band, simplifying comparisons between the 150 GHz and 220 GHz maps.

Calibration and beams

We take advantage of the superb WMAP5 absolute calibration and calibrate the SPT data through a direct comparison of 150 GHz SPT maps with WMAP5 V and W-band maps [Hinshaw et al., 2009]. The SPT performed dedicated calibration scans of five large fields totaling 1250 deg^2 of sky during 2008. The WMAP5 maps were then resampled with the SPT pointing information, and the resulting timestreams were passed through a simulated

SPT analysis pipeline to capture the filtering applied during the SPT map-making algorithm. The ratio of the cross-spectra of the SPT maps and the filtered WMAP maps after correcting for the instrumental beams provides an estimate of the relative calibration factor between the two experiments. This procedure, similar to that used for the analysis of ACBAR data and detailed in Reichardt et al. [2009], results in an absolute calibration accurate to 3.6% at 150 GHz.

The 150 GHz calibration is transferred to 220 GHz by making use of the overlapping coverage on SPT's high signal-to-noise maps of CMB fluctuations in large survey fields. We calculate the ratio of the cross-spectra of the map at each frequency band to the auto-spectra of the CMB-dominated 150 GHz map after correcting for the beam and filtering differences. The calibration uncertainty of the 220 GHz maps is found to be 7.2%. Because the thermal SZ signal in the 220 GHz map is small, the higher calibration uncertainty only marginally increases the errors on the cluster profiles discussed in this chapter.

The 2008 SPT beams were measured by observing bright sources and averaging the response for all detectors in a given band. The sidelobes of the beam were estimated from observations of planets, and—since the detectors show signs of nonlinearity when pointed directly at planets—the main lobes were estimated from observations of quasars. The main lobes are reasonably approximated by 2D elliptical Gaussians with average full widths at half maximum (FWHM) of 1.2 and 1.1 arcminutes for 150 and 220 GHz. These are larger than would be naively calculated from the aperture diameter and observing wavelength due to the combination of an underilluminated primary (to reduce spillover) and telescope pointing uncertainty; see Padin et al. [2008] for details. The sidelobes fall off from ~ -30dB at a radius of $5'$ to < -45dB at $30'$, and account for about 15% of the degree-scale beam response. Errors in this beam estimate contribute to the overall calibration uncertainty, and also add small additional uncertainties to the best-fit model parameters.

We model the response of the instrument to an astronomical source by constructing a simulated map of a point source, convolving it with the beam, constructing simulated timestreams using telescope pointing information, and then running the timestreams through our processing pipeline. The output map normalized to the input signal is referred to as the transfer function, and is used to subtract bright point sources from the cluster maps. Representative transfer functions are shown in Figure 7.1. The negative stripe at constant elevation is due to the polynomial template subtraction, and results in temperature increments to the east and west of the cluster SZ decrements. This effect can be ameliorated by masking the cluster before applying the time domain filtering (see Figure 7.2), but doing so reduces the effectiveness of the atmospheric noise removal. Since we account for the effects of the time domain filtering on the profiles as described in Section 7.3.1, we avoid degrading the signal-to-noise of our results by analyzing the unmasked data.

Mapmaking and astrophysical background cleaning

For every observation, a map is made for each observing frequency using the processed data for all detectors in that band. Pointing information (R.A. and decl.) is calculated for each detector using focal-plane offsets measured in observations of the galactic HII regions, and boresight pointing calculated using data from the telescope pointing readout system, with a set of corrections described in Staniszewski et al. [2009] that result in a pointing

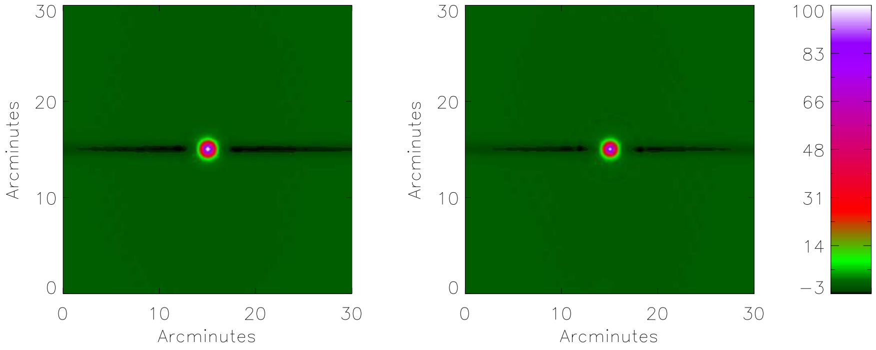

Figure 7.1. Point source transfer functions at 150 GHz (left) and 220 GHz (right). Units are percent of maximum. The stripe through the center of the maps is the result of the polynomial template removal.

RMS of $7''$. These coordinates are then converted to pixel number using a Sanson-Flamsteed projection [Calabretta and Greisen, 2002] with 0.25-arcminute pixels. All measurements of a given pixel's brightness are averaged using inverse-variance weighting based on the mean of each detector's processed and relative-gain-scaled power spectrum between 1 and 3 Hz, which for our scan speed is a frequency range well-matched to the scale of SZ cluster signals.

All of the single observation maps for a given cluster in a given band are then coadded to produce a set of single-band maps, which we denote as M^{150} and M^{220} for the 150 GHz and 220 GHz bands. Each single-band map consists of signals from several astrophysical sources: the SZ effect, which is at arcminute scales and is much stronger at 150 GHz; the primary CMB anisotropy, which dominates at large spatial scales and is the same in both bands; and a background of typically faint dusty point sources, which are at small angular scales and are stronger at 220 GHz. We wish to produce a "band subtracted map" M^{sub}, in which the 220 GHz map is used to remove a fraction of the CMB and point source background while leaving the SZ signal intact. Since the 2008 SPT receiver was less sensitive to CMB fluctuations at 220 GHz than at 150 GHz, and since the atmospheric noise is worse in the higher frequency band, this background removal must be handled carefully to avoid introducing excess noise into the band subtracted map.

Using our knowledge of the spatial scales of the CMB and point source signals, we apply a matched spatial filter ψ to the 220 GHz map, which we construct by requiring that the variance in the band subtracted map be minimized [Haehnelt and Tegmark, 1996, Herranz et al., 2002a,b, Melin et al., 2006]. Since the signal and noise are more easily characterized in the spatial frequency domain, we adopt the flat sky approximation and construct the filter as a function of multipole moment $\boldsymbol{\ell}$. Denoting the Fourier transform of X as $\tilde{X}$, we can express the value of the band subtracted map at a given multipole moment as:

$$\tilde{M}^{sub}_{\boldsymbol{\ell}} = \tilde{M}^{150}_{\boldsymbol{\ell}} - \psi_{\boldsymbol{\ell}} \tilde{M}^{220}_{\boldsymbol{\ell}}. \tag{7.1}$$

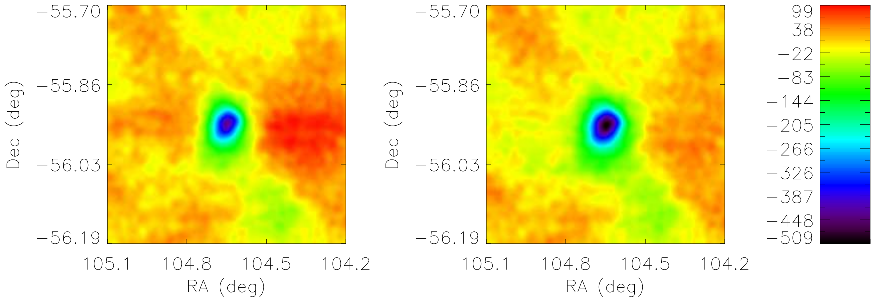

Figure 7.2. Maps of 1ES 0657-56 at 150 GHz, with the cluster region unmasked (left) and masked (right) for time domain filtering. Units are μK_{CMB}. In the masked map, data from a circular region $8'$ in radius centered on the cluster is not included in the polynomial and wedge common mode construction. This map gives a clear picture of the shape and amplitude of the SZ emission, but has slightly higher noise. The artifacts of the time domain filtering in the unmasked map are taken into account in the cluster profiles by the algorithm described in Section 7.3.1.

The variance at a given $\boldsymbol{\ell}$, $V_{\boldsymbol{\ell}}$, is then given by

$$V_{\boldsymbol{\ell}} = \begin{pmatrix} 1 & -\psi_{\boldsymbol{\ell}} \end{pmatrix} \begin{pmatrix} \tilde{S}^{\mathrm{CMB}}_{\boldsymbol{\ell}} + \tilde{S}^{\mathrm{PS}}_{\boldsymbol{\ell}} + \tilde{N}^{150}_{\boldsymbol{\ell}} & \tilde{S}^{\mathrm{CMB}}_{\boldsymbol{\ell}} + \alpha \tilde{S}^{\mathrm{PS}}_{\boldsymbol{\ell}} \\ \tilde{S}^{\mathrm{CMB}}_{\boldsymbol{\ell}} + \alpha \tilde{S}^{\mathrm{PS}}_{\boldsymbol{\ell}} & \tilde{S}^{\mathrm{CMB}}_{\boldsymbol{\ell}} + \alpha^2 \tilde{S}^{\mathrm{PS}}_{\boldsymbol{\ell}} + \tilde{N}^{220}_{\boldsymbol{\ell}} \end{pmatrix} \begin{pmatrix} 1 \\ -\psi_{\boldsymbol{\ell}} \end{pmatrix} \tag{7.2}$$

where $\tilde{S}^{\mathrm{CMB}}_{\boldsymbol{\ell}}$ is the CMB signal, $\tilde{S}^{\mathrm{PS}}_{\boldsymbol{\ell}}$ is the point source signal, $\tilde{N}^{X}_{\boldsymbol{\ell}}$ is the noise in band X, and α is a factor corresponding to the spectral index of the point sources. The filter that minimizes this variance is given by

$$\psi_{\boldsymbol{\ell}} = \frac{\tilde{S}^{\mathrm{CMB}}_{\boldsymbol{\ell}} + \alpha \tilde{S}^{\mathrm{PS}}_{\boldsymbol{\ell}}}{\tilde{S}^{\mathrm{CMB}}_{\boldsymbol{\ell}} + \alpha^2 \tilde{S}^{\mathrm{PS}}_{\boldsymbol{\ell}} + \tilde{N}^{220}_{\boldsymbol{\ell}}}. \tag{7.3}$$

Note that both the signal and the noise terms are anisotropic with respect to azimuth and elevation due to the scan strategy employed in these observations, necessitating a 2D filter function. Errors in either the signal or noise terms will result in a slightly sub-optimal filter, and will thus increase the errors in the results, but will not lead to systematic mis-estimations of the profiles or cluster parameters.

The signal covariances of the primary CMB anisotropies and undetected point sources are estimated using simulations based on the best-fit WMAP5 CMB power spectrum [Nolta et al., 2009] and the Borys et al. [2003] model for dusty point sources. We assume that the point sources are Poisson distributed and have a spectral index of 2.7. The power spectrum of the source count distribution is computed using the formalism in White and Majumdar [2004], and is inflated by a factor of 40% to account for lensing by our massive cluster

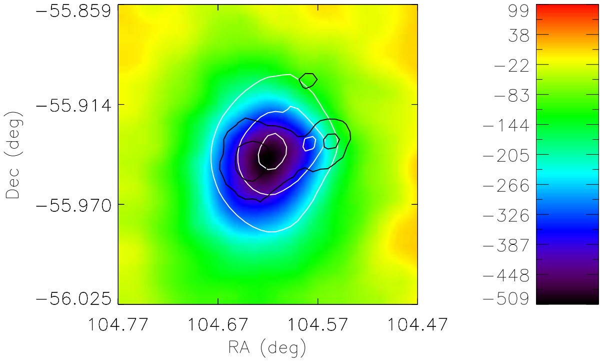

Figure 7.3. 150 GHz 1ES 0657-56 masked map with X-ray plasma density (white) and weak lensing surface mass density (black) contours overlaid. Units are $\mu K_{\rm CMB}$. This cluster is an ongoing merger, and the electron gas is not in equilibrium within the gravitational potential well. The SZ signal tracks the X-ray plasma density more closely than the surface mass density.

targets [Lima et al., 2009]. Even with this enhancement, the dusty sources are predicted to contribute an r.m.s. of $\sim$4 μK to the band subtracted maps, well below the map noise level. We disregard contamination due to radio sources, as explicit simulations demonstrate [Sehgal et al., 2009] that they are not likely to significantly fill in the 150 GHz SZ decrements of massive $z \lesssim 0.4$ clusters. For both the CMB and the dusty point sources, we generate 300 simulated maps and apply the same time domain filtering that was applied to the SPT maps. We find $\tilde{S}^{\mathrm{CMB}}_{\boldsymbol{\ell}}$ and $\tilde{S}^{\mathrm{PS}}_{\boldsymbol{\ell}}$ by taking the mean of the 2D spatial power spectra over the simulated maps.

The instrumental and atmospheric noise properties of the maps are estimated using the two-dimensional power spectra of noise maps [Sayers et al., 2009, Halverson et al., 2008]. Under the assumption of stationarity in the map basis, the noise covariance matrix in band X, $\tilde{N}^{\mathrm{X}}_{\mathrm{noise}}$, is diagonal in the spatial frequency domain and equal to the noise power spectrum. For each observation, we produce one map using only data from the left-going scans, and one map using only data from the right-going scans. We then multiply one half of the $2n$ maps by -1 and coadd to produce a jackknife noise map. We repeat this process for $m >> n$ combinations of observations, computing the 2d spatial power spectrum for each individual jackknife map. The average of these power spectra is our estimate of $\tilde{N}^{\mathrm{X}}_{\mathrm{noise}}$.

Sayers et al. [2009] and Halverson et al. [2008] use this noise estimate to construct a covariance matrix and to fit models directly to their cluster maps. However, since we have relatively few independent observations of each cluster, our noise estimate is less well-constrained. We cannot combine data from different clusters to improve the noise estimate due to the fact that the noise is non-stationary between the observations. The amplitude of the atmospheric noise varies with time and as a function of elevation angle, and the clusters in this sample are at a wide range of elevation angles. We circumvent this limitation by computing the projected radial profiles of the clusters, for which the covariance matrix has fewer degrees of freedom and is thus better constrained by our data.

7.2 Sample selection and cluster maps

During the austral winter of 2008, the SPT observed 11 of the 13 highest-luminosity clusters in the REFLEX survey within the range of declination angles observable by the SPT ($-30^\circ \gtrsim$ decl. $\gtrsim -70^\circ$). These clusters form the primary sample used in this work. One of the two REFLEX clusters that were omitted, RXCJ1253.6-3931, is associated with a radio bright PMN source that would have been difficult to remove from the SZ maps. The other, RXCJ1234.2-3856, was omitted due to time constraints. Of the next three brightest REFLEX clusters, RXCJ0532.9-3927 is a part of the supplemental sample; RXCJ2011.3-4037, was found by Maughan et al. [2008] to have an electron temperature of just 3.8 keV, and was not detected at greater than 3σ by the SPT; and RXCJ1317.1-3821 is associated with a bright radio source. From the remaining 2008 SPT targeted cluster observations, four additional clusters were selected to form our supplemental sample. These clusters were chosen because of the availability of archived X-ray satellite data, which will be relevant for future work. They also contribute to our understanding of pressure profiles, and demonstrate the ability of the SPT to make high signal-to-noise maps of clusters with lower X-ray luminosities.

The positions and depths of the final coadded maps are listed in Table 7.2, and the images can be found in Appendix B. Four maps are shown for each cluster: the 150 and 220 GHz single-band maps, the band subtracted map, and a jackknife band subtracted map computed by multiplying half of the observations by -1 before coadding. Each map is smoothed by a Gaussian with a full width at half maximum (FWHM) of $1'$. All clusters are detected with high significance. Since the maps each have distinct noise properties, we do not expect the detection significance to provide quantitative information about cluster parameters.

As discussed in Section 7.1.2, the time domain processing creates large-scale distortions in the maps visible as temperature increments to the east and west of the clusters. No mask has been applied to the data used to construct the maps in Appendix B. Figure 7.3 shows the 1ES 0657-56 SZ map constructed from data with the cluster masked before time domain filtering. Shown as contours in Figure 7.3 are publicly-available X-ray plasma surface density and weak lensing surface density data[1]. As expected, once the effects of the beam and time domain filtering are mitigated, the SZ signal closely tracks the electron plasma density.

7.2.1 Source contamination

A point source within $10''$ of quasar J001341.2-300926 was detected at $> 5\sigma$ significance in the map for A 2744, $16.5'$ from the cluster center, and has been removed from the maps by subtracting the point source transfer function scaled to the best-fit amplitude. The SPT measured fluxes for this source are 17.7 mJy at 150 GHz and 27.8 mJy at 220 GHz. In the AS 0592 map, a point source was removed at an R.A. of $06^{\mathrm{h}}38^{\mathrm{m}}19^{\mathrm{s}}$ and a decl. of $-53°57'29''$. The fluxes at 150 GHz and 220 GHz were 21.8 mJy and 13.4 mJy, respectively. This source is $6.8'$ from the cluster center, and has not been previously identified by surveys.

Wilson et al. [2008] report a dusty point source approximately $1'$ to the east of 1ES 0657-56, with flux density of 13.5 ± 0.5 mJy at 270 GHz. Assuming a spectral index of 2.7, we would expect to see 7.8 and 2.8 mJy in the 220 and 150 GHz SPT maps. The SPT does not make a significant detection of a source at these coordinates in either band. We measure a temperature increment of 34 ± 33 $\mu\mathrm{K}_{\mathrm{CMB}}$ in our 220 GHz map (smoothed by a $1'$ FWHM Gaussian). By finding a best-fit amplitude for our point source transfer function, we infer a 220 GHz flux density of 4.2 ± 4.5 mJy. At 150 GHz, the strong SZ decrement near the source position prevents us from determining the source flux. We find from simulations that a source with the predicted fluxes at these coordinates would have a $< 5\%$ effect on the corresponding bins in the band subtracted cluster profile.

7.3 Projected radial profiles

7.3.1 Profile computation

To proceed with measurements of global cluster properties from the maps, it is useful to approximate the clusters as azimuthally symmetric and to calculate their projected radial profiles, which are expected to take a universal form [Arnaud et al., 2009]. We do so by computing transfer functions for a set of concentric annuli with inner and outer radii set to the boundaries of the radial bins for which we wish to estimate an average SZ decrement.

---

[1] http://flamingos.astro.ufl.edu/1e0657/public.html

These transfer functions are then used to compute a profile transfer function matrix, which is inverted and applied to the maps in order to account for the effects of the beam and the time domain filtering. This technique also allows us to characterize the correlated errors between bins.

The cluster center coordinates must be determined in order to generate radial profiles. We define the center position by fitting a β-model with $\beta = 0.86$ to the map with the center R.A. and decl., central temperature decrement, and core radius free to vary. We then marginalize over the central decrement and core radius to determine the cluster center. The fit uncertanties on the center position vary from $1''$ to $4''$, indicating very high signal-to-noise detections, and the results are consistent when the generalized NFW model is used in place of the $\beta-$model. The difference between the X-ray centroid (which depends primarily on density) and the SZ center position (which depends on integrated pressure) is small for most clusters, but reaches $40 - 50''$ for RXCJ0232.2-4420, MACSJ0553.4-3342, and A 3888. An X-ray-derived pressure map for RXCJ0232.2-4420 is shown in Finoguenov et al. [2005], and the SPT centroid falls within the elongated central high-pressure region.

For each band subtracted cluster map $M^{\rm sub}$, we divide the 0.5° by 0.5° region surrounding the center position into radial bins b_i. The bin spacing is defined so as to measure the profile of the cluster center with beam-scale resolution, and to keep the number of bins small enough so that the noise properties can be well-constrained. Each bin is then assigned a radius r_i by finding the average radius over all pixels within the bin. For bin b_i and band X, we define T_i to be the mean SZ temperature decrement on the sky within the bin. We construct a set of simulated maps corresponding to each bin in each band, in which the "temperature" for map i is set to 1 inside bin b_i and 0 elsewhere. These maps are then convolved with the appropriate beam. To account for the effect of the time domain filtering, we construct simulated timestreams from these maps using the telescope pointing data from each observation, and apply to them the same polynomial and common mode filtering that was applied to the data. We then produce from these filtered timestreams a set of $n_{\rm bins}$ processed maps—the annular transfer function maps $F_i^{\rm sub}$ (see Figure 7.4 for an example)—which show the response of the instrument at each pixel location to an annulus of constant temperature corresponding to bin b_i. Finally, these maps are Hanning apodized, Fourier transformed, and represented as vectors $\tilde{F}_i^{\rm sub}$ of length $n_{\rm pixels}$. From these vectors, we construct an $n_{\rm pixels} \times n_{\rm bins}$ matrix

$$\tilde{B}_{ji}^{\rm sub} = (\tilde{F}_i^{\rm sub})_j, \tag{7.4}$$

the annular transfer function matrix, where $\tilde{B}_{ji}^{\rm sub}$ gives the response in the jth Fourier mode of the band subtracted map to an impulse in bin b_i.

Using this formalism, we can write a set of equations relating the Fourier transform of the Hanning apodized measured SPT map $\tilde{M}_j^{\rm sub}$ to the sky temperatures T_i:

$$\tilde{M}_j^{\rm sub} = \tilde{B}_{ji}^{\rm sub} T_i. \tag{7.5}$$

Since there are many more map pixels than radial bins, this is an overconstrained system of linear equations, for which the least-squares solution is given by

$$T = (\tilde{B}^T \tilde{W} \tilde{B})^{-1} \tilde{B}^T \tilde{W} \tilde{M}, \tag{7.6}$$

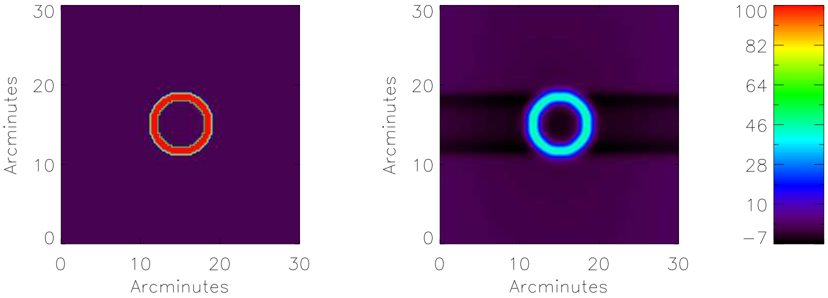

Figure 7.4. Bin b_3 (left) and its 150 GHz annular transfer function map (right). Units are percent of maximum. The annular transfer function map represents the response of the SPT to a corresponding annulus of constant temperature, taking into account the beam and the time domain filtering.

where we have supressed the superscript denoting band subtracted quantities and where $\tilde{W}$ is the weight matrix. The weights are given by $\tilde{W} = 1/(\tilde{N} + \tilde{S}^{\mathrm{CMB}} + \tilde{S}^{\mathrm{PS}})$, where $\tilde{N}$ is the detector and atmospheric noise and $\tilde{S}^{\mathrm{CMB}}$ and $\tilde{S}^{\mathrm{PS}}$ are the CMB and dusty point source signals. These terms are all computed for the band subtracted map using the method described in Section 7.1.2. Weighting the Fourier modes by their noise reduces the profile errors by 20-30% compared with uniform weights. The covariance matrix for the profile is given by $(\tilde{B}^T W \tilde{B})^{-1}$, plus small additional terms to account for calibration and beam uncertainties. Figure 7.5 shows the importance of this procedure: the amplitudes and shapes of the profiles are badly mis-estimated if the beams and time domain filtering are not taken into account.

Since the SPT measures temperature differences, the cluster maps have arbitrary constant offsets. These manifest themselves as offsets in the profiles, and could bias the model fits if they were not taken into account. We include a constant offset as a parameter in our model fitting, and marginalize over this parameter in order to determine the quoted central decrements and angular scale radii. The profiles shown in Appendix B are plotted with the offset fixed such that the temperature decrement in the outermost radial bin is zero.

7.3.2 Model fitting

We make use of the cluster profiles and their noise covariance matrices to perform maximum likelihood fits to proposed models of the ICM. Our likelihood function is given by

$$\mathcal{L}(T|\mathcal{M}) = \frac{1}{\sqrt{(2\pi)^n \det(N_{\mathrm{noise}})}} \exp\left(-\frac{\chi^2}{2}\right), \tag{7.7}$$

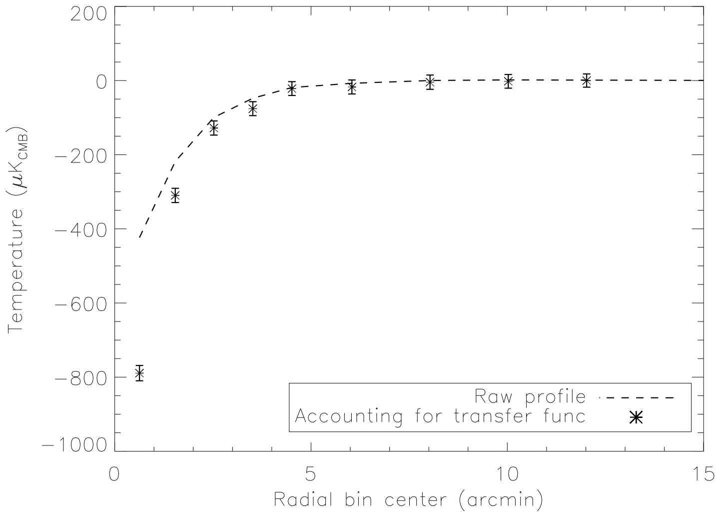

Figure 7.5. AS 1063 profile with and without beam and time domain filtering correction. The uncorrected profile is computed by averaging the pixels in the band subtracted map within the radial bins, and the corrected profile is computed as described in Section 7.3.1.

where $n = 10$ is the number of radial bins, T is the measured profile, $\mathcal{M}$ is the proposed model, and χ^2 is given by

$$\chi^2 = (\mathcal{M} - T)^T (N_{\text{noise}})^{-1} (\mathcal{M} - T). \tag{7.8}$$

We will consider two models: the β-model and the GNFW model.

The $\beta-$model for thermal SZ cluster signals is motivated by the widely used $\beta-$model parameterization of the 3-dimensional electron number density:

$$n_e(\boldsymbol{r}) = n_{\text{e}_0} \left(1 + \frac{r^2}{r_{\text{core}}^2}\right)^{-3\beta/2}, \tag{7.9}$$

where n_{e} is the electron number density, n_{e_0} is the number density at the cluster center, r is the radius from the cluster center, r_{core} is the core radius of the gas distribution, and β is the power law index at large radii. Using this density function and assuming isothermality, Equation 2.21 can be integrated along the line of sight through the cluster to give a simple analytic formula for the SZ decrement:

$$\Delta T_{\text{SZ}} = \Delta T_0 \left(1 + \frac{\theta^2}{\theta_{\text{core}}^2}\right)^{(1-3\beta)/2}, \tag{7.10}$$

where θ is the angular distance from the cluster center, given by $\theta = r/D_A$ where D_A is the angular diameter distance (computed assuming that $(\Omega_M, \Omega_\Lambda, h) = (0.3, 0.7, 0.7)$), ΔT_0 is the central temperature decrement, and θ_{core} is the angle corresponding to r_{core}. Although we do not necessarily expect the clusters in our sample to be isothermal, we nevertheless adopt Equation 7.10 as a convenient parameterization of the SZ signal.

Two of the β−model parameters, β and $r_{\rm core}$, are highly degenerate and difficult to constrain with SZ data alone [Grego et al., 2001]. We fix β at 0.86, the overall best-fit value for our sample (see Section 7.4.2). Typical X-ray cluster analyses yield values of β between about 0.6 and 0.8 [LaRoque et al., 2006, and citations therein], but while the X-ray surface brightness is relatively insensitive to ICM temperature [Mohr et al., 1999], the SZ signal is proportional to the integrated pressure of the ICM. Therefore, any radial trend in temperature would lead to systematic differences between X-ray and SZ profiles. Our finding of $\beta \sim 0.86$ suggests that the ICM temperature tends to decrease with increasing radius, in qualitative agreement with direct measurements of cluster temperature profiles [e.g. Pratt et al., 2007] and with hydrodynamical cluster simulations. Hallman et al. [2007] find that β values for SZ profiles are systematically higher than X-ray β values by a factor of 1.21, consistent with the SPT results.

We also fit to the GNFW model, which parameterizes the 3-dimensional electron pressure as

$$P_{\rm e}(\boldsymbol{r}) = \frac{P_{\rm e_0}}{(r/r_{\rm s})^{\gamma_{\rm n}}\left(1 + (r/r_{\rm s})^{\alpha_{\rm n}}\right)^{(\beta_{\rm n}-\gamma_{\rm n})/\alpha_{\rm n}}}, \tag{7.11}$$

where P_{e_0} is the pressure at the cluster center; r is the radius from the cluster center; $r_s = r_{500}/c_{500}$ is a scaling radius set by r_{500}, the radius within which the average cluster density falls to 500 times the critical density of the universe at the cluster redshift, and c_{500}, a parameter characterizing the gas concentration; and $\alpha_{\rm n}$, $\beta_{\rm n}$, and $\gamma_{\rm n}$ set the slope at intermediate ($r \sim r_{\rm s}$), large ($r > r_{\rm s}$), and small ($r < r_{\rm s}$) radii, respectively. We fix $(\alpha_{\rm n}, \beta_{\rm n}, \gamma_{\rm n}, c_{500})$ to $(1.0, 5.5, 0.5, 1.0)$, the parameters found to be the best fit to our stacked cluster profile (see Section 7.4.2). These values are very similar to those found by Nagai et al. [2007] when fitting to *Chandra* data, $(\alpha_{\rm n}, \beta_{\rm n}, \gamma_{\rm n}, c_{500}) = (0.9, 5.0, 0.4, 1.3)$[2]. As the SZ effect is directly proportional to integrated pressure, we calculate $\Delta T_{\rm SZ}$ given the pressure profile by numerically integrating the above function along the line of sight. As before, we define $\theta_s = r_s/D_A$. Note that fitting for r_s with c_{500} fixed is equivalent to fitting for r_{500}. However, because the quality of the GNFW fit varies across our sample, we will later make use of a scaling relation to estimate r_{500}.

Both models thus contain two free parameters: a central temperature decrement, and a scaling radius ($\theta_{\rm core}$ for the β−model and θ_s for the GNFW model). As discussed in Section 7.3.1, an offset parameter is also included.

7.3.3 The effect of CMB and atmospheric noise

The model fitting technique described in Section 7.3.2 makes use of the full profile noise covariance matrices, including off-diagonal terms that describe correlations. This is important because the noise in the SPT maps can introduce spurious structure in the profiles that is highly correlated between bins. Most of these correlations arise from primary CMB anisotropies and atmospheric noise, the combination of which dominates the uncertainties in the profiles.

---

[2] These values are taken from Mroczkowski et al. [2009], and are updated from the results in Nagai et al. [2007].

The large angular scale confusion due to primary CMB anisotropies represents a fundamental limitation for single-band measurements of SZ radial profiles. The SPT 220 GHz data allow us to reduce the level of confusion; however, the 220 GHz maps have significantly more atmospheric noise than do the 150 GHz maps. Timestream filtering can help to mitigate atmospheric noise, but filtering too heavily will remove CMB signal. We chose our level of time domian filtering by balancing these two effects, in order to maximize the CMB signal-to-noise at 220 GHz.

The matched spatial filter described in Section 7.1.2 is constructed to downweight noise-contaminated modes in the 220 GHz maps, and thus to increase the effectiveness of the CMB subtraction. Other spatial filters can be applied to the 220 GHz maps in order to change the balance between CMB and atmospheric confusion in the band subtracted map. We constructed several alternative filters which improved the CMB subtraction at the expense of introducing atmospheric noise. In all cases, the resulting profiles and fits were found to be consistent but the errors were increased: by construction, the matched filter yields the best signal-to-noise in the band subtracted maps. Optimal band subtraction reduces the large angular scale confusion by a factor of two or more, depending on the depth of the 220 GHz map.

Nevertheless, large scale correlated noise due to atmospheric fluctuations and unsubtracted CMB remains present in the band subtracted maps. Figure 7.6 shows the effect of this confusion on one band subtracted profile with particularly low 220 GHz signal-to-noise. While this cluster is an extreme example, the same issue persists across the entire sample. As in earlier SZ works, we find that model fits are in some respects more robust indicators of global cluster properties than are the measured profiles, since the choice of a realistic model imposes sensible constraints on less well-constrained modes. We therefore make extensive use of model fitting when interpreting the SPT profiles and integrated Componizations.

7.4 Results

7.4.1 Profiles and model fits

The projected radial profiles of the band subtracted maps can be found in Appendix B. Dashed vertical lines in the profile plots denote estimates of the cluster virial radii given by $\sqrt{500/\Delta_c}r_{500}$, where Δ_c is calculated using the approximation in Bryan and Norman [1998], and where r_{500} is determined from the temperature-radius scaling relation in Vikhlinin et al. [2006]. Beyond these radii, the models are not expected to be reliable. The error bars on the profiles are determined using Monte Carlo methods, and as discussed in Section 7.3.3, are strongly correlated between bins.

The best-fit central decrement and scaling radius for each cluster are listed in Table 7.3, along with the minimum χ^2 and the logarithmic ratio of the marginal likelihoods of the GNFW and $\beta-$models:

$$R \equiv \log_{10}\left(\int \mathcal{L}_{\mathrm{GNFW}} d\theta_s d\Delta T_0 / \int \mathcal{L}_{\beta} d\theta_{\mathrm{core}} d\Delta T_0\right) \tag{7.12}$$

where $\mathcal{L}_{\mathrm{GNFW}}$ is the likelihood function for the GNFW model and $\mathcal{L}_{\beta}$ is the likelihood function for the $\beta-$model. This quantity can be interpreted as a likelihood ratio, with a

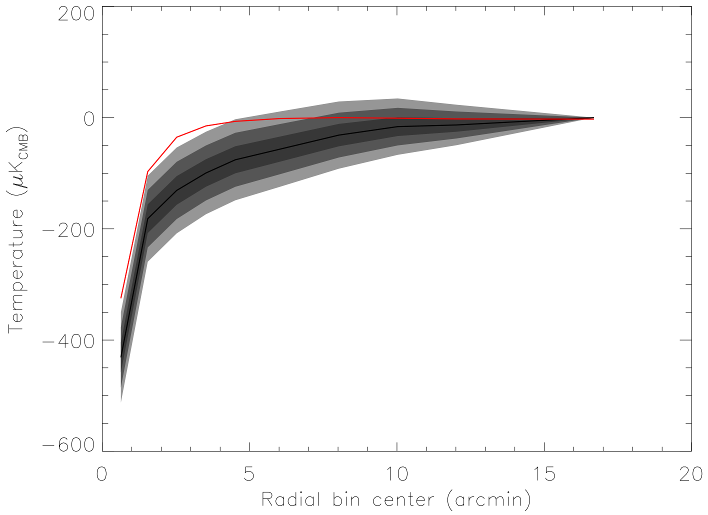

Figure 7.6. The measured profile (black) and best-fit β-model (red) for RXCJ2031.8-4037. The noise level in the 220 GHz map for this cluster is among the highest in the sample, so the noise correlations between bins are large. Shown in gray are the results of varying the first component of the measured profile by 1, 2, and 3 σ in the eigenbasis of the noise covariance matrix.

value of 10 corresponding to a 10:1 preference for the GNFW model. For the recent mergers 1ES 0657-56 and A 2744, neither model is a good fit, though the β-model is strongly favored. The $\beta-$model yields a larger marginal likelihood for over half of the sample, but the SPT data do not definitively favor one model over the other.

Table 7.3. Best-fit model parameters.

	Isothermal $\beta-$model		GNFW model				
ID	ΔT_0 (μK$_{\mathrm{CMB}}$)	θ_{core} ($'$)	ΔT_0 (μK$_{\mathrm{CMB}}$)	θ_s ($'$)	R	χ^2	PTE
Primary Sample							
A 2744	-549 ± 27	1.51 ± 0.06	-670 ± 33	7.87 ± 0.51	-50.79	19.50	0.01
RXCJ0217.2-5244	-214 ± 29	0.64 ± 0.13	-262 ± 34	3.12 ± 0.63	-0.84	5.24	0.63
RXCJ0232.2-4420	-510 ± 26	0.99 ± 0.05	-626 ± 32	5.01 ± 0.31	17.72	9.68	0.21
AS 0520	-217 ± 13	1.22 ± 0.12	-268 ± 16	6.80 ± 0.86	16.33	9.16	0.24
RXCJ0528.9-3927	-335 ± 20	1.78 ± 0.14	-412 ± 25	10.03 ± 1.24	5.53	7.46	0.38
AS 0592	-529 ± 31	0.79 ± 0.06	-658 ± 40	3.77 ± 0.29	-3.51	3.00	0.89
A 3404	-472 ± 29	0.95 ± 0.08	-588 ± 38	4.52 ± 0.43	1.20	4.09	0.77
1ES 0657-56	-932 ± 43	1.47 ± 0.03	-1133 ± 52	7.56 ± 0.22	-270.59	65.61	0.00
RXCJ2031.8-4037	-511 ± 42	0.65 ± 0.07	-616 ± 48	3.24 ± 0.35	-3.76	11.66	0.11
A 3888	-516 ± 26	1.35 ± 0.07	-634 ± 32	6.79 ± 0.49	-28.25	8.64	0.28
AS 1063	-1062 ± 50	0.86 ± 0.02	-1321 ± 62	4.14 ± 0.12	-2.54	28.61	0.00
Supplemental Sample							
RXCJ0336.3-4037	-306 ± 30	0.70 ± 0.10	-388 ± 40	3.20 ± 0.46	-5.11	28.33	0.00
RXCJ0532.9-3701	-449 ± 24	1.00 ± 0.07	-543 ± 29	5.66 ± 0.52	21.25	35.43	0.00
MACSJ0553.4-3342	-680 ± 34	0.96 ± 0.05	-849 ± 44	4.54 ± 0.26	-18.63	28.33	0.00
A 3856	-256 ± 26	0.71 ± 0.11	-313 ± 31	3.49 ± 0.55	-0.01	2.17	0.95

The β-model fit is performed with β fixed to 0.86, and the GNFW fit is performed with the parameters $(\alpha_{\mathrm{n}}, \beta_{\mathrm{n}}, \gamma_{\mathrm{n}}, c_{500})$ fixed to $(1.0, 5.5, 0.5, 1.0)$. The sixth column quantifies the relative goodness of fit in terms of the marginal likelihood ratio (see text). Positive values indicate that the GNFW model is preferred, and negative values indicate that the $\beta-$model is preferred. The seventh column is the χ^2 for the preferred model, and the eighth is the probability to exceed this value of χ^2 for seven degrees of freedom.

7.4.2 Stacked profiles

Each individual cluster profile contains too little information to place a tight constraint on the pressure behavior at large radius. We proceed by scaling the profiles to r_{500}, as determined from the temperature-radius scaling relation in Vikhlinin et al. [2006], and analyzing the data set as a whole—by constructing a stacked profile, and by fitting models to the sample. The stacked profile, shown in Figure 7.7, is determined by averaging the scaled profiles weighted by their noise. Each radial bin in the stacked profile is assigned a radius and a temperature from the average of the scaled profiles, and an uncertainty is assigned by the standard error on the mean.

We fit models to the sample by evaluating the likelihood function for each individual cluster at each point in a grid of parameter space, and then by multiplying the cluster likelihoods together to produce a joint likelihood. This allows us to determine average values for the structure parameters in our two models. For the β-model, we allow β and $r_{\rm core}/r_{500}$ to vary. We allow the central decrement and overall constant offset of each profile to vary as well, and we marginalize over these parameters. The cluster center position is held fixed, leaving six remaining degrees of freedom per cluster. We find that for the full sample, the marginalized values of β and $r_{\rm core}/r_{500}$ are 0.86 ± 0.09 and 0.20 ± 0.05. Excluding the supplemental sample from the fit does not appreciably change the results. The minimum χ^2 for the fit is 338 for 90 degrees of freedom, indicating a relatively poor fit. If β is fixed to a typical X-ray value of 2/3, the minimum χ^2 is 362. If 1ES 0657-56 is excluded from the fit, the minimum reduced χ^2 changes from $338/90 = 3.76$ to $296/84 = 3.52$, and the marginalized values of $(\beta, r_{\rm core}/r_{500})$ change to $(0.78 \pm 0.08, 0.17 \pm 0.04)$.

For the generalized NFW model, we fit for the structure parameters $\alpha_{\rm n}$, $\beta_{\rm n}$, $\gamma_{\rm n}$, and c_{500}, again fixing the center positions and marginalizing over the central decrements of all of the clusters. The likelihood-weighted mean values are $(\alpha_{\rm n}, \beta_{\rm n}, \gamma_{\rm n}, c_{500}) = (1.0, 5.5, 0.5, 1.0)$ and the marginalized values are $(1.2 \pm 0.5, 5.0 \pm 2.0, 0.7 \pm 0.3, 1.3 \pm 0.5)$. The minimum χ^2 for the fit is 468, compared to 472 for the Nagai et al. [2007] parameter values of $(\alpha_{\rm n}, \beta_{\rm n}, \gamma_{\rm n}, c_{500}) = (0.9, 5.0, 0.4, 1.3)$—the change in χ^2 is small due to strong degeneracies between the parameters. If 1ES 0657-56 is excluded from the GNFW fit, the marginalized parameter values do not change appreciably, but the minimum reduced χ^2 drops from $468/75 = 6.24$ to $318/70 = 4.54$.

In Figure 7.8, the SPT maximum likelihood GNFW model with $(\alpha_{\rm n}, \beta_{\rm n}, \gamma_{\rm n}, c_{500})$=$(1.0, 5.5, 0.5, 1.0)$ is compared to the $(0.9, 5.0, 0.4, 1.3)$ model found by Nagai et al. [2007] and the $(1.05, 5.49, 0.31, 1.18)$ model found by Arnaud et al. [2009]. Nagai et al. [2007] use a sample of nearby relaxed clusters, while Arnaud et al. [2009] use the REXCESS sample of $z < 0.2$ clusters. Two systems—A 3888 and A 3856—are in both the SPT and REXCESS samples. On average, however, the samples are quite different, with the SPT clusters tending to be hotter and more distant. The similarity between the resulting profiles is encouraging for future applications of self-similar pressure models.

The SPT best-fit β-model and GNFW model are shown in Figure 7.7. Since the models are very similar, the fits are of roughly equal quality. The logarithmic ratio of marginal likelihoods (see Equation 7.12) for the GNFW model compared to the β-model is $R = -322$, indicating a preference for the latter. This preference is due primarily to 1ES 0657-56, and to a lesser extent to A 2744. Both of these clusters are major mergers. Excluding the former

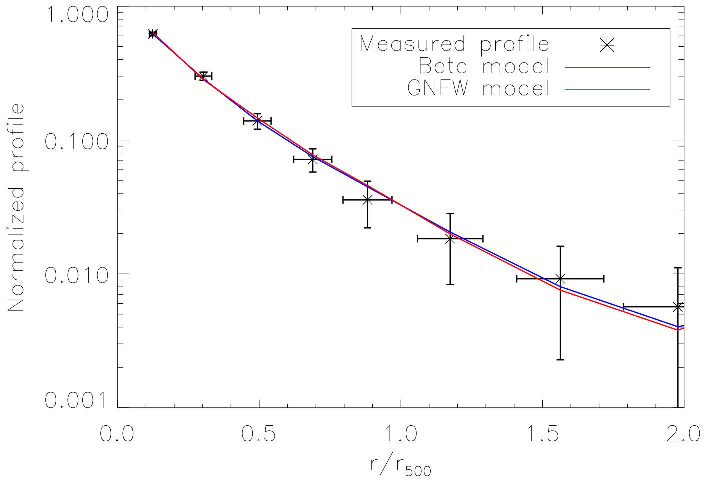

Figure 7.7. Stacked radial profile and maximum likelihood β-model and GNFW model fits. The plot extends to $2r_{500}$, which is approximately equal to the average virial radius for the sample. The best-fit model profiles are computed from simulated processed maps in the same way that the cluster profiles are computed (see Section 7.3.1), and are shown as a continuous line only for the purpose of visualization.

brings the marginal likelihood ratio to $R = -51$, and excluding both brings the ratio to $R = -0.6$.

7.4.3 Integrated y parameter and scaling relations

The integrated Compton-y parameter $Y_{\rm SZ}$ is expected to serve as a good proxy for mass, and to be related to other physical properties of clusters by scaling relations. $Y_{\rm SZ}$ can be computed either using the model fits discussed in Section 7.3.2, or using the model-independent radial profiles. Since the large angular scale noise contributes strongly to the model-independent estimate, we consider the model-dependent results to be slightly more robust. The average ratio across the sample of $Y_{\rm SZ}$ computed from the β-model fit, to $Y_{\rm SZ}$ computed from the GNFW model fit, is 1.06 ± 0.08 at r_{2500} and 1.19 ± 0.20 at r_{500}. This is due to the fact that a $\beta = 0.86$ model falls off more gradually at intermediate radius than does the GNFW model with our best-fit structure parameters. Since the β-model is slightly preferred over the GNFW model across our sample, we use the β-model fits to compute our model-dependent results.

Both the model-dependent and the model-independent estimates of the integrated Compton-y parameter are given in Table 7.4. Uncertainties are determined via Monte Carlo methods, and the apertures are again determined from the temperature-radius scaling relation. Since the slope of the temperature-radius scaling relation is relatively shallow, the aperture radii vary only by $\sim 10\%$ across our sample. We find that integrating out to a fixed radius of order 1 Mpc does not significantly increase the scatter in the scaling relations.

The β-model and model-independent estimates at r_{2500} are in relatively good agreement,

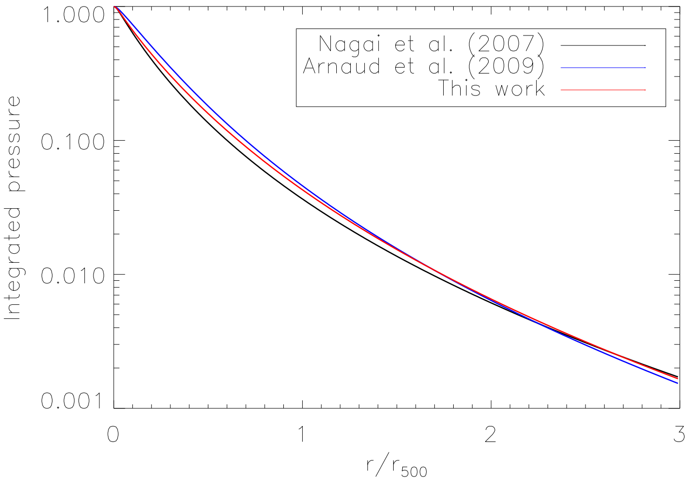

Figure 7.8. GNFW models with best-fit slope and concentration parameters from Nagai et al. [2007], Arnaud et al. [2009], and this work. Note that the samples in each work differ in characteristic redshift, morphology, and temperature. These results are indicative of the consistency between X-ray and SZ pressure measurements.

with a ratio of model-dependent to model-independent Y_{SZ} of 0.99 ± 0.22. Significant scatter is seen at r_{500}, where the ratio is 1.30 ± 0.56. The model-independent SZ signal is less well-constrained at larger radius due to its lower amplitude and to the large angular scale confusion discussed in Section 7.3.3. The model-dependent estimates are less affected by confusion, as noisier modes are down-weighted in the model fitting process. We therefore use the β-model estimates to explore scaling relations with X-ray values, which are also derived in a model-dependent manner.

Halverson et al. [2008] have recently observed 1ES 0657-56 with the APEX-SZ experiment, and have fit an ellipsoidal β-model to their 150 GHz SZ map. Since we assume azimuthal symmetry and fit models to the radial profiles rather than the maps, we cannot perform a directly comparable fit. However, we can compare our respective estimates of $Y_{\rm SZ}$. The APEX-SZ best-fit ellipsoidal model yields $(Y_{\rm SZ,2500}, Y_{\rm SZ,500}) = (30 \pm 5, 66 \pm 18) \times 10^{-11}$ sr, which is consistent at the $\sim 1\sigma$ level with both the model-dependent and model-independent SPT results.

Table 7.4. Integrated Compton $y-$parameters.

ID	r_{2500}	r_{500}	$\beta-$model		Model-independent	
	(Mpc)	(Mpc)	$Y_{\mathrm{SZ},2500}$	$Y_{\mathrm{SZ},500}$	$Y_{\mathrm{SZ},2500}$	$Y_{\mathrm{SZ},500}$
Primary Sample						
A 2744	0.63	1.40	20.3 ± 0.7	49.2 ± 2.3	19.0 ± 1.4	38.1 ± 6.8
RXCJ0217.2-5244	0.61	1.36	3.3 ± 0.4	6.3 ± 1.0	3.6 ± 0.9	4.8 ± 2.7
RXCJ0232.2-4420	0.52	1.17	11.2 ± 0.4	24.8 ± 1.1	12.9 ± 0.9	26.7 ± 4.3
AS 0520	0.54	1.21	5.7 ± 0.4	13.7 ± 1.4	4.7 ± 0.8	7.2 ± 2.7
RXCJ0528.9-3927	0.53	1.19	11.1 ± 0.7	31.0 ± 2.9	9.8 ± 0.9	22.1 ± 4.4
AS 0592	0.58	1.30	12.9 ± 0.6	24.7 ± 1.6	14.7 ± 2.0	26.0 ± 9.8
A 3404	0.60	1.35	18.2 ± 1.3	34.6 ± 3.1	13.5 ± 3.0	14.0 ± 5.4
1ES 0657-56	0.65	1.44	36.2 ± 0.6	84.9 ± 1.8	30.0 ± 1.0	45.9 ± 4.7
RXCJ2031.8-4037	0.64	1.43	8.4 ± 0.5	16.1 ± 1.4	14.3 ± 1.6	37.0 ± 8.0
A 3888	0.59	1.33	30.1 ± 1.5	60.8 ± 3.7	24.6 ± 3.8	36.1 ± 14.7
AS 1063	0.65	1.44	23.3 ± 0.4	48.3 ± 1.1	25.5 ± 1.1	44.5 ± 5.3
Supplemental Sample						
RXCJ0336.3-4037	0.56	1.26	7.5 ± 0.7	13.7 ± 1.7	11.0 ± 2.5	27.8 ± 11.8
RXCJ0532.9-3701	0.62	1.38	12.8 ± 0.7	26.6 ± 1.9	18.1 ± 1.7	42.4 ± 8.0
MACSJ0553.4-3342	0.69	1.52	15.8 ± 0.5	34.3 ± 1.5	14.7 ± 1.4	20.5 ± 5.1
A 3856	0.55	1.23	7.3 ± 0.8	13.1 ± 1.7	7.7 ± 2.9	9.8 ± 6.4

Units for Y_{SZ} are 10^{-11} sr. Both model-dependent and model-independent estimates are provided (see text). r_{2500} and r_{500} are determined from the temperature-radius scaling relation.

The β-model estimates of $Y_{\rm SZ,500}$ are plotted versus X-ray estimates of gas mass and Y_X in Figure 7.9. $Y_{\rm X} = M_{\rm gas}kT_e$ is an X-ray observable analogous to $Y_{\rm SZ}$ [Kravtsov et al., 2006], which we convert to units of steradians as in Bonamente et al. [2008]. Only clusters with published values of gas mass and electron temperature from the references in Table 7.1 are included in the plots. Several clusters have multiple published X-ray estimates of electron temperature and gas mass. For our plots in Figure 7.9, we chose to adopt the Zhang et al. [2006, 2008] results where available, since these samples had the largest overlap with our own. For different choices of published X-ray values, we find scaling relation parameters that are consistent at the 2σ level.

$Y_{\rm SZ}$ is also expected to scale with electron temperature and total mass. However, the reported errors in the X-ray estimates of electron temperature vary widely across our sample, and different analyses of the same clusters often produce inconsistent results. The X-ray total mass estimates are determined under the assumption of hydrostatic equilibrium, and the errors are quite large. For this reason, we do not include the total mass and electron temperature scaling relations in this work. In a future work, we will pursue a joint SZ and X-ray analysis which can more appropriately incorporate these uncertainties.

The $Y_{\rm SZ}$-gas mass plot is in a form readily comparable to the scaling relation given in Bonamente et al. [2008]:

$$Y_{\rm SZ}D_A^2 \propto f_{\rm gas}^{-2/3}M_{\rm gas}^{5/3}E(z)^{2/3} \tag{7.13}$$

where D_A is the angular diameter distance, $f_{\rm gas}$ is the gas mass fraction (which we assume to be constant), $E(z)$ is given by $\sqrt{\Omega_M(1+z)^3+\Omega_\Lambda}$, and $M_{\rm gas}$ is the cluster gas mass. We fit for the gas mass scaling relation in log-log space using the method described in Marrone et al. [2009], assuming a scaling in the form $Y = \alpha + \beta X$ and allowing for intrinsic scatter. We find $\alpha = -5.73 \pm 0.43$ and $\beta = 2.12 \pm 0.45$. The best-fit intrinsic scatter in this scaling relation, in terms of a percentage change in $M_{\rm gas}$ at fixed Y_{SZ}, is $14 \pm 10\%$. If we substitute $Y_{SZ,2500}$ for $Y_{SZ,500}$, we find a similar scaling relation with $M_{\rm gas,500}$: $\alpha = -5.92 \pm 0.41$, $\beta = 1.97 \pm 0.44$, and a scatter of $15 \pm 11\%$.

The gas masses of two clusters in our sample, 1ES 0657-56 and RXCJ0232.2-4420, are estimated both from *Chandra* data in Maughan et al. [2008] and from XMM data in Zhang et al. [2006]. In both cases, the Maughan et al. [2008] estimates ($2.31^{+0.01}_{-0.01} \times 10^{14} M_\odot$ for 1ES 0657-56 and $1.20^{+0.01}_{-0.02} \times 10^{14} M_\odot$ for RXCJ0232.2-4420) are larger than the Zhang et al. [2006] results we have adopted. If we instead adopt the larger values, we find $\beta = 1.85 \pm 0.43$, consistent with the self-similar expectation.

The Y_{SZ}-Y_X relation is expected to have a small scatter and to have a slope of 1.0. Our best-fit power law parameters are $\alpha = 2.42 \pm 0.87$ and $\beta = 1.56 \pm 0.21$, with an intrinsic scatter of $12 \pm 12\%$ in Y_X. Substituting $Y_{SZ,2500}$ for $Y_{SZ,500}$ gives a scaling relation of $\alpha = 1.69 \pm 0.78$, $\beta = 1.46 \pm 0.20$, and a scatter of $9 \pm 9\%$. While these slopes are inconsistent with the expected value of 1.0, the discrepancy is largely due to the three lowest signal-to-noise data points: A 3856, AS 0520, and A 3404. In the gas mass scaling relation, we found that adopting independent published values of gas mass introduced significant variations in the slope and offset. Since Y_X is computed from the same $M_{\rm gas}$ estimates, comparable systematic uncertainties and offsets are expected. We therefore hesitate to draw conclusions before performing a more uniform X-ray analysis.

We consider these Y_{SZ}-gas mass and Y_{SZ}-Y_X scaling relations to be reasonably consistent with the self-similar values, and we find no measurable scatter within the limits of our statistical and systematic errors. Previous studies [e.g., Mantz et al., 2009, Kravtsov et al., 2006] have found that $M_{\rm gas}$ and Y_X scale with the total cluster mass with low scatter, and these results indicate that Y_{SZ} as measured with the SPT should behave similarly. Future joint analyses of X-ray and SZ data will further constrain these scaling relations, and will provide better limits on any departure from self-similarity.

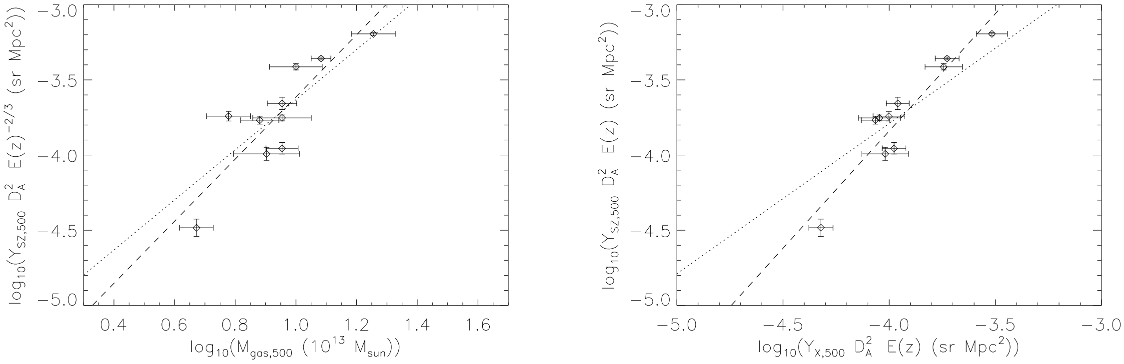

Figure 7.9. Comparisons between SZ and X-ray measurements within r_{500}: $Y_{SZ} - M_{\rm gas}$ (left) and $Y_{SZ} - Y_X$ (right). X-ray values are taken from the references in Table 7.1, and clusters without published values in these sources are omitted. SZ values are taken from the β-model estimates in Table 7.4. The dashed lines represent the best fit power laws, and the dotted lines represent the best bit powers law with the slopes fixed to the expected self-similar values of 5/3 (left) and 1 (right).

7.5 Conclusions

In this chapter, I have summarized Sunyaev-Zel'dovich observations of 15 bright galaxy clusters taken with the South Pole Telescope. The SZ signals were measured at 150 GHz, and concurrent 220 GHz measurements were used to remove astrophysical contamination. Radial profiles were computed for each cluster using a technique that accounts for the effects of the beam and the time domain filtering, and simultaneously characterizes the correlated errors due to detector and atmospheric noise.

The profiles were fit both to a $\beta-$model and to a generalized NFW model [Nagai et al., 2007]. By scaling and stacking the SPT profiles, and allowing the structure parameters of the models to vary, we obtained self-similar pressure profiles that agree closely with previous X-ray and SZ results. For the $\beta-$model, we found $\beta = 0.86 \pm 0.09$ and $r_{\rm core}/r_{500} = 0.20 \pm 0.05$. For the GNFW model, we found $(\alpha_{\rm n}, \beta_{\rm n}, \gamma_{\rm n}, c_{500})$=$(1.0, 5.5, 0.5, 1.0)$, similar to the parameters found by Nagai et al. [2007] and Arnaud et al. [2009]. The SPT data do not strongly prefer one model over the other. Our measurements show no significant difference between the stacked SZ profile and the models out to the the virial radius. This is the first SZ-measured constraint on cluster pressure profiles at such large radii.

We also estimated the integrated Compton-y parameter Y_{SZ} for each cluster using both model-dependent and model-independent techniques. The scaling relations between Y_{SZ} and the X-ray-determined M_{gas} and Y_X were found to be reasonably consistent with the self-similar values. We find no measurable scatter in the scaling relations, indicating that the intrinsic and systematic scatter are likely to be low. Previous studies have indicated that gas mass and Y_X scale with low scatter to the total cluster mass. These results indicate that Y_{SZ} as measured with the SPT should behave similarly, which is encouraging for the ongoing SPT cluster SZ survey.

The data presented in this chapter demonstrate the utility of SZ measurements for characterizing the ICM out to large radii. In future works, we will expand the SPT sample of X-ray luminous clusters, and will include 95 GHz data in addition to 150 and 220 GHz. The addition of a third frequency band will allow us to better remove astrophysical backgrounds such as the CMB, thus improving our estimates of thermal SZ signals at large radii. Future analyses will also combine SZ measurements with X-ray cluster observations in order to separately estimate the temperature and density of the ICM, and to determine the cluster gas mass fractions.

Bibliography

S. Padin, Z. Staniszewski, R. Keisler, M. Joy, A. A. Stark, P. A. R. Ade, K. A. Aird, B. A. Benson, L. E. Bleem, J. E. Carlstrom, C. L. Chang, T. M. Crawford, A. T. Crites, M. A. Dobbs, N. W. Halverson, S. Heimsath, R. E. Hills, W. L. Holzapfel, C. Lawrie, A. T. Lee, E. M. Leitch, J. Leong, W. Lu, M. Lueker, J. J. McMahon, S. S. Meyer, J. J. Mohr, T. E. Montroy, T. Plagge, C. Pryke, J. E. Ruhl, K. K. Schaffer, E. Shirokoff, H. G. Spieler, and J. D. Vieira. South pole telescope optics. *Appl. Opt.*, 47(24):4418–4428, 2008.

G. Gamow. Expanding universe and the origin of elements. *Physical Review*, 70(7-8):572–573, 1946.

A.A. Penzias and R.W. Wilson. A Measurement of Excess Antenna Temperature at 4080 Mc/s. *ApJ*, 142:419–421, July 1965.

D.P. Woody and P.L. Richards. *Phys. Rev. Lett.*, 42:925, 1979.

J.C. Mather, D.J. Fixsen, R.A. Shafer, C. Mosier, and D.T. Wilkinson. Calibrator Design for the COBE Far-Infrared Absolute Spectrophotometer (FIRAS). *ApJ*, 512:511–520, February 1999.

D.J. Fixsen, E.S. Cheng, J.M. Gales, J.C. Mather, R.A. Shafer, and E.L. Wright. The Cosmic Microwave Background Spectrum from the Full COBE FIRAS Data Set. *ApJ*, 473:576, December 1996.

G.F. Smoot et al. Structure in the COBE Differential Microwave Radiometer First-Year Maps. *ApJ*, 396:L1–L5, 1992.

S. Hanany, P. Ade, A. Balbi, J. Bock, J. Borrill, A. Boscaleri, P. de Bernardis, P.G. Ferreira, V.V. Hristov, A.H. Jaffe, A.E. Lange, A.T. Lee, P.D. Mauskopf, C.B. Netterfield, S. Oh, E. Pascale, B. Rabii, P.L. Richards, G.F. Smoot, R. Stompor, C.D. Winant, and J.H.P. Wu. Maxima-1: A measurement of the cosmic microwave background anisotropy on angular scales of 10'-5°. *ApJ*, 545:L5–L9, December 2000. astro-ph/0005123.

A.T. Lee, P. Ade, A. Balbi, J. Bock, J. Borrill, A. Boscaleri, P. de Bernardis, P.G. Ferreira, S. Hanany, V.V. Hristov, A.H. Jaffe, P.D. Mauskopf, C.B. Netterfield, E. Pascale, B. Rabii, P.L. Richards, G.F. Smoot, R. Stompor, C.D. Winant, and J.H.P. Wu. A High Spatial Resolution Analysis of the MAXIMA-1 Cosmic Microwave Background Anisotropy Data. *ApJ*, 561:L1–L5, November 2001. astro-ph/0104459.

C.B. Netterfield, P.A.R. Ade, J.J. Bock, J.R. Bond, J. Borrill, A. Boscaleri, K. Coble, C.R. Contaldi, B.P. Crill, P. de Bernardis, P. Farese, K. Ganga, M. Giacometti, E. Hivon, V.V. Hristov, A. Iacoangeli, A.H. Jaffe, W.C. Jones, A.E. Lange, L. Martinis, S. Masi, P. Mason, P.D. Mauskopf, A. Melchiorri, T. Montroy, E. Pascale, F. Piacentini, D. Pogosyan, F. Pongetti, S. Prunet, G. Romeo, J.E. Ruhl, and F. Scaramuzzi. A Measurement by BOOMERANG of Multiple Peaks in the Angular Power Spectrum of the Cosmic Microwave Background. *ApJ*, 571:604–614, June 2002. astro-ph/0104460.

N.W. Halverson, E.M. Leitch, C. Pryke, J. Kovac, J.E. Carlstrom, W.L. Holzapfel, M. Dragovan, J.K. Cartwright, B.S. Mason, S. Padin, T.J. Pearson, A.C.S. Readhead, and M.C. Shepherd. Degree Angular Scale Interferometer First Results: A Measurement of the Cosmic Microwave Background Angular Power Spectrum. *ApJ*, 568:38–45, March 2002. astro-ph/0104489.

G. Hinshaw, D.N. Spergel, L. Verde, R.S. Hill, S.S. Meyer, C. Barnes, C.L. Bennett, M. Halpern, N. Jarosik, A. Kogut, E. Komatsu, M. Limon, L. Page, G.S. Tucker, J. Weiland, E. Wollack, and E.L. Wright. First Year Wilkinson Microwave Anisotropy Probe (WMAP) Observations: Angular Power Spectrum. *ApJ submitted*, February 2003. astro-ph/0302217.

G. Hinshaw, J.L. Weiland, R.S. Hill, N. Odegard, D. Larson, C.L. Bennett, J. Dunkley, B. Gold, M.R. Greason, N. Jarosik, E. Komatsu, M.R. Nolta, L. Page, D.N. Spergel, E. Wollack, M. Halpern, A. Kogut, M. Limon, S.S. Meyer, G.S. Tucker, and E.L. Wright. Five-Year Wilkinson Microwave Anisotropy Probe Observations: Data Processing, Sky Maps, and Basic Results. *ApJS*, 180:225–245, February 2009.

C.L. Kuo, P.A.R. Ade, J.J. Bock, C. Cantalupo, M.D. Daub, J. Goldstein, W.L. Holzapfel, A.E. Lange, M. Lueker, M. Newcomb, J.B. Peterson, J. Ruhl, M.C. Runyan, and E. Torbet. High-Resolution Observations of the Cosmic Microwave Background Power Spectrum with ACBAR. *ApJ*, 600:32–51, January 2004. astro-ph/0202289.

C.L. Reichardt, P.A.R. Ade, J.J. Bock, J.R. Bond, J.A. Brevik, C.R. Contaldi, M.D. Daub, J.T. Dempsey, J.H. Goldstein, W.L. Holzapfel, C.L. Kuo, A.E. Lange, M. Lueker, M. Newcomb, J.B. Peterson, J. Ruhl, M.C. Runyan, and Z. Staniszewski. High-Resolution CMB Power Spectrum from the Complete ACBAR Data Set. *ApJ*, 694:1200–1219, April 2009.

S. Padin, J.K. Cartwright, B.S. Mason, A.C.S. Readhead, M.C. Shepherd, J. Sievers, P.S. Udomprasert, W.L. Holzapfel, S.T. Myers, J.E. Carlstrom, E.M. Leitch, M. Joy, L. Bronfman, and J. May. First intrinsic anisotropy observations with the cosmic background imager. *ApJ*, 549:L1, 2001. astro-ph/0012211.

B.S. Mason, T.J. Pearson, A.C.S. Readhead, M.C. Shepherd, J. Sievers, P.S. Udomprasert, J.K. Cartwright, A.J. Farmer, S. Padin, S.T. Myers, J.R. Bond, C.R. Contaldi, U. Pen, S. Prunet, D. Pogosyan, J.E. Carlstrom, J. Kovac, E.M. Leitch, C. Pryke, N.W. Halverson, W.L. Holzapfel, P. Altamirano, L. Bronfman, S. Casassus, J. May, and M. Joy. The Anisotropy of the Microwave Background to l = 3500: Deep Field Observations with the Cosmic Background Imager. *ApJ*, 591:540–555, July 2003.

J. M. Kovac, E. M. Leitch, C. Pryke, J. E. Carlstrom, N. W. Halverson, and W. L. Holzapfel. Detection of polarization in the cosmic microwave background using DASI. *Nature*, 420: 772, December 2002.

C. Pryke and the QUaD Collaboration. Second and third season QUaD CMB temperature and polarization power spectra. *Astrophys. J.*, 692:1247–1270, 2009.

L. Page, G. Hinshaw, E. Komatsu, M.R. Nolta, D.N. Spergel, C.L. Bennett, C. Barnes, R. Bean, O. Doré, J. Dunkley, M. Halpern, R.S. Hill, N. Jarosik, A. Kogut, M. Limon, S.S. Meyer, N. Odegard, H.V. Peiris, G.S. Tucker, L. Verde, J.L. Weiland, E. Wollack, and E.L. Wright. Three-Year Wilkinson Microwave Anisotropy Probe (WMAP) Observations: Polarization Analysis. *ApJS*, 170:335–376, June 2007.

H. C. Chiang et al. Measurement of CMB Polarization Power Spectra from Two Years of BICEP Data. 2009.

E. Hubble. A relation between distance and radial velocity among extra-galactic nebulae. *Proceedings of the National Academy of Sciences*, 15(3):168–173, 1929.

E. Komatsu, J. Dunkley, M.R. Nolta, C.L. Bennett, B. Gold, G. Hinshaw, N. Jarosik, D. Larson, M. Limon, L. Page, et al. Five-Year Wilkinson Microwave Anisotropy Probe Observations: Cosmological Interpretation. *Astrophys. J. Suppl*, 180:330–376, 2009.

A. G. Riess, A. V. Filippenko, P. Challis, A. Clocchiattia, A. Diercks, P. M. Garnavich, R. L. Gilliland, C. J. Hogan, S. Jha, R. P. Kirshner, B. Leibundgut, M. M. Phillips, D. Reiss, B. P. Schmidt, R. A. Schommer, R. C. Smith, J. Spyromilio, C. Stubbs, N. B. Suntzeff, and J. Tonry. Observational evidence from supernovae for an accelerating universe and a cosmological constant. *AJ*, 116:1009, 1998.

S. Perlmutter, G. Aldering, G. Goldhaber, R.A. Knop, P. Nugent, P.G. Castro, S. Deustua, S. Fabbro, A. Goobar, D.E. Groom, I.M. Hook, A.G. Kim, M.Y. Kim, J.C. Lee, N.J. Nunes, R. Pain, C.R. Pennypacker, R. Quimby, C. Lidman, R.S. Ellis, M. Irwin, R.G. McMahon, P. Ruiz-Lapuente, N. Walton, B. Schaefer, B.J. Boyle, A.V. Filippenko, T. Matheson, A.S. Fruchter, N. Panagia, H.J.M. Newberg, W.J. Couch, and The Supernova Cosmology Project. Measurements of omega and lambda from 42 high-redshift supernovae. *ApJ*, 517:565–586, June 1999. astro-ph/9812133.

J.F. Navarro, C.S. Frenk, and S.D.M. White. The Structure of Cold Dark Matter Halos. *ApJ*, 462:563–+, May 1996.

W.H. Press and P. Schechter. Formation of galaxies and clusters of galaxies by self-similar gravitational condensation. *ApJ*, 187:425, 1974.

R.A. Sunyaev and Y.B. Zeldovich. The Spectrum of Primordial Radiation, its Distortions and their Significance. *Comments on Astrophysics and Space Physics*, 2:66–+, March 1970a.

R.Ã. Sunyaev and Y.B̃. Zeldovich. Small-scale fluctuations of relic radiation. *Ap&SS*, 7:3, 1970b.

M. Birkinshaw. The sunyaev zel'dovich effect. *Physics Reports*, 310:97, 1999.

J.E. Carlstrom, G.P. Holder, and E.D. Reese. Cosmology with the Sunyaev-Zel'dovich Effect. *ARA&A*, 40:643–680, 2002.

N. Itoh, Y. Kawana, S. Nozawa, and Y. Kohyama. Relativistic corrections to the sunyaev-zel'dovich effect for clusters of galaxies v. multiple scattering. *ApJ*, 2000.

A. Cavaliere and R. Fusco-Femiano. X-rays from hot plasma in clusters of galaxies. *A&A*, 49:137, May 1976.

A. Cavaliere and R. Fusco-Femiano. The distribution of hot gas in clusters of galaxies. *A&A*, 70:677, 1978.

D. Rapetti, S.W. Allen, and A. Mantz. The prospects for constraining dark energy with future X-ray cluster gas mass fraction measurements. *MNRAS*, 388:1265–1278, August 2008.

L. Grego, J.E. Carlstrom, M.K. Joy, E.D. Reese, G.P. Holder, S. Patel, A.R. Cooray, and W.L. Holzapfel. The sunyaev-zeldovich effect in abell 370. *ApJ*, 539:39, August 2000.

E.D. Reese, J.E. Carlstrom, M. Joy, J.J. Mohr, L. Grego, and W.L. Holzapfel. Determining the Cosmic Distance Scale from Interferometric Measurements of the Sunyaev-Zeldovich Effect. *ApJ*, 581:53–85, December 2002.

B.A. Benson, S.E. Church, P.A.R. Ade, J.J. Bock, K.M. Ganga, C.N. Henson, and K.L. Thompson. Measurements of Sunyaev-Zel'dovich Effect Scaling Relations for Clusters of Galaxies. *ApJ*, 617:829–846, December 2004.

N.W. Halverson, T. Lanting, P.A.R. Ade, K. Basu, A.N. Bender, B.A. Benson, F. Bertoldi, H.-. Cho, G. Chon, J. Clarke, M. Dobbs, D. Ferrusca, R. Guesten, W.L. Holzapfel, A. Kovacs, J. Kennedy, Z. Kermish, R. Kneissl, A.T. Lee, M. Lueker, J. Mehl, K.M. Menten, D. Muders, M. Nord, F. Pacaud, T. Plagge, C. Reichardt, P.L. Richards, R. Schaaf, P. Schilke, F. Schuller, D. Schwan, H. Spieler, C. Tucker, A. Weiss, and O. Zahn. Sunyaev-Zel'dovich Effect Observations of the Bullet Cluster (1E 0657-56) with APEX-SZ. *ApJ*, submitted, July 2008. arXiv.0807.4208.

A. Vikhlinin, M. Markevitch, S.S. Murray, C. Jones, W. Forman, and L. Van Speybroeck. Chandra Temperature Profiles for a Sample of Nearby Relaxed Galaxy Clusters. *ApJ*, 628:655–672, August 2005.

R. Piffaretti, P. Jetzer, J.S. Kaastra, and T. Tamura. Temperature and entropy profiles of nearby cooling flow clusters observed with XMM-Newton. *A&A*, 433:101–111, April 2005.

D. Nagai, A.V. Kravtsov, and A. Vikhlinin. Effects of Galaxy Formation on Thermodynamics of the Intracluster Medium. *ApJ*, 668:1–14, October 2007.

T. Mroczkowski, M. Bonamente, J.E. Carlstrom, T.L. Culverhouse, C. Greer, D. Hawkins, R. Hennessy, M. Joy, J.W. Lamb, E.M. Leitch, M. Loh, B. Maughan, D.P. Marrone, A. Miller, S. Muchovej, D. Nagai, C. Pryke, M. Sharp, and D. Woody. Application of a Self-Similar Pressure Profile to Sunyaev-Zel'Dovich Effect Data from Galaxy Clusters. *ApJ*, 694:1034–1044, April 2009.

Joseph J Mohr. Cluster Survey Studies of the Dark Energy. 2004.

A.J.C. da Silva. SZ scaling relations in Galaxy Clusters: Results from hydrodynamical N-body simulations. *Ap&SS*, 290:167–176, February 2004.

D. Nagai. The Impact of Galaxy Formation on the Sunyaev-Zel'dovich Effect of Galaxy Clusters. *ApJ*, 650:538–549, October 2006.

P.M. Motl, E.J. Hallman, J.O. Burns, and M.L. Norman. The Integrated Sunyaev-Zeldovich Effect as a Superior Method for Measuring the Mass of Clusters of Galaxies. *ApJ*, 623: L63–L66, April 2005.

A.V. Kravtsov, A. Vikhlinin, and D. Nagai. A New Robust Low-Scatter X-Ray Mass Indicator for Clusters of Galaxies. *ApJ*, 650:128–136, October 2006.

G.P. Holder, I.G. McCarthy, and A. Babul. The Sunyaev-Zeldovich background. *MNRAS*, 382:1697–1706, December 2007.

J.E. Carlstrom, P.A.R. Ade, K.A. Aird, B.A. Benson, L.E. Bleem, S. Busetti, C.L. Chang, E. Chauvin, H.-M. Cho, T.M. Crawford, A.T. Crites, M.A. Dobbs, N.W. Halverson, S. Heimsath, R.E. Hills, W.L. Holzapfel, M. Joy, R. Keisler, T.M. Lanting, A.T. Lee, E.M. Leitch, J. Leong, W. Lu, M. Lueker, J.J. McMahon, S.S. Meyer, J.J. Mohr, T.E. Montroy, S. Padin, T. Plagge, C. Pryke, J.E. Ruhl, K.K. Schaffer, D. Schwan, E. Shirokoff, H.G. Spieler, Z. Staniszewski, A.A. Stark, and J.D. Vieira. The South Pole Telescope. *PASP*, submitted, 2009.

A.P. Lane. Submillimeter transmission at South Pole. In G. Novak and R.H. Landsberg, editors, *Astrophysics from Antarctica*, volume 141 of *ASP Conf. Ser. 141*, page 289, San Francisco, 1998. ASP.

M.J. Griffin, J.J. Bock, and W.K. Gear. Relative performance of filled and feedhorn-coupled focal-plane architectures. *Appl. Opt.*, 41:6543–6554, November 2002. astro-ph/0205264.

J.W. Lamb. Miscellaneous data on materials for millimetre and submillimetre optics. *International Journal of Infrared and Millimeter Waves*, 17:1997–2034, December 1996.

J. J. Mehl. *Cosmological Studies of the Sunyaev-Zel'dovich Effect with the APEX-SZ Instrument.* PhD thesis, University of California, Berkeley, 2009.

J.R. Pardo, J. Cernicharo, and E. Serabyn. Atmospheric transmission at microwaves (ATM): an improved model for millimeter/submillimeter applications. *IEEE Transactions on Antennas and Propagation*, 49:1683–1694, December 2001.

R.S. Bhatia, S.T. Chase, S.F. Edgington, J. Glenn, W.C. Jones, A.E. Lange, B. Maffei, A.K. Mainzer, P.D. Mauskopf, B.J. Philhour, et al. A three-stage helium sorption refrigerator for cooling of infrared detectors to 280 mK. *Cryogenics*, 40(11):685–691, 2000.

M.C. Runyan, P.A.R. Ade, R.S. Bhatia, J.J. Bock, M.D. Daub, J.H. Goldstein, C.V. Haynes, W.L. Holzapfel, C.L. Kuo, A.E. Lange, J. Leong, M. Lueker, M. Newcomb, J.B. Peterson, C. Reichardt, J. Ruhl, G. Sirbi, E. Torbet, C. Tucker, A.D. Turner, and D. Woolsey. ACBAR: The Arcminute Cosmology Bolometer Array Receiver. *ApJS*, 149:265–287, December 2003.

P.L. Richards. Bolometers for infrared and millimeter waves. *Journal of Applied Physics*, 76:1–24, July 1994.

S. Lee, J.M. Gildemeister, W. Holmes, A.T. Lee, and P.L. Richards. Voltage-Biased Superconducting Transition-Edge Bolometer with Strong Electrothermal Feedback Operated at 370 mK. *Appl. Opt.*, 37:3391–3397, June 1998.

J.C. Mather. Bolometer noise: nonequilibrium thoery. *Appl. Opt.*, 21:1125–1129, March 1982.

K.D. Irwin, G.C. Hilton, D.A. Wollman, and J.M. Martinis. Thermal-response time of superconducting transition-edge microcalorimeters. *Journal of Applied Physics*, 83:3978–3985, April 1998.

M. Lueker, B.A. Benson, C.L. Chang, H.-M. Cho, M. Dobbs, W.L. Holzapfel, T. Lanting, A.T. Lee, J. Mehl, T. Plagge, E. Shirokoff, H.G. Spieler, and J.D. Vieira. Thermal Design and Characterization of Transition-Edge Sensor (TES) Bolometers for Frequency-Domain Multiplexing. *IEEE Transactions on Applied Superconductivity*, 19:496–500, June 2009.

J.M. Gildemeister, A.T. Lee, and P.L. Richards. Model for Excess Noise in Voltage-biased Superconducting Bolometers. *Appl. Opt.*, 40:6229–6235, December 2001.

R.S. Bussmann, W.L. Holzapfel, and C.L. Kuo. Millimeter Wavelength Brightness Fluctuations of the Atmosphere above the South Pole. *ApJ*, 622:1343–1355, April 2005.

Z. Staniszewski, P.A.R. Ade, K.A. Aird, B.A. Benson, L.E. Bleem, J.E. Carlstrom, C.L. Chang, H.-M. Cho, T.M. Crawford, A.T. Crites, T. de Haan, M.A. Dobbs, N.W. Halverson, G.P. Holder, W.L. Holzapfel, J.D. Hrubes, M. Joy, R. Keisler, T.M. Lanting, A.T. Lee, E.M. Leitch, A. Loehr, M. Lueker, J.J. McMahon, J. Mehl, S.S. Meyer, J.J. Mohr, T.E. Montroy, C.-C. Ngeow, S. Padin, T. Plagge, C. Pryke, C.L. Reichardt, J.E. Ruhl, K.K. Schaffer, L. Shaw, E. Shirokoff, H.G. Spieler, B. Stalder, A.A. Stark, K. Vanderlinde, J.D. Vieira, O. Zahn, and A. Zenteno. Galaxy Clusters Discovered with a Sunyaev-Zel'dovich Effect Survey. *ApJ*, 701:32–41, August 2009.

T.M. Lanting. *Multiplexed readout of superconducting bolometers for cosmological observations*. PhD thesis, University of California, Berkeley, 2006.

B.D. Josephson. Possible new effects in superconductive tunnelling. *Physics Letters*, 1: 251–253, July 1962.

T. Van Duzer and C.W. Turner. Principles of superconductive devices and circuits. 1998.

J.A. Chervenak, K.D. Irwin, E.N. Grossman, J.M. Martinis, C.D. Reintsema, and M.E. Huber. Superconducting Multiplexer for Arrays of Transition Edge Sensors. *Applied Physics Letters*, 74:4043–4045, June 1999.

J. Yoon, J. Clarke, J.M. Gildemeister, A.T. Lee, M.J. Myers, P.L. Richards, and J.T. Skidmore. Single Superconducting Quantum Interference Device Multiplexer for Arrays of Low-Temperature Sensors . *Applied Physics Letters*, 78:371–373, January 2001.

H. Böhringer, P. Schuecker, L. Guzzo, C.A. Collins, W. Voges, R.G. Cruddace, A. Ortiz-Gil, G. Chincarini, S. De Grandi, A.C. Edge, H.T. MacGillivray, D.M. Neumann, S. Schindler, and P. Shaver. The ROSAT-ESO Flux Limited X-ray (REFLEX) Galaxy cluster survey. V. The cluster catalogue. *A&A*, 425:367–383, October 2004.

Y.-Y. Zhang, H. Böhringer, A. Finoguenov, Y. Ikebe, K. Matsushita, P. Schuecker, L. Guzzo, and C.A. Collins. X-ray properties in massive galaxy clusters: XMM-Newton observations of the REFLEX-DXL sample. *A&A*, 456:55–74, September 2006.

J.P. Hughes, F. Menanteau, N. Sehgal, L. Infante, and F. Barrientos. X-ray Clusters in the ACT Strip. In *Bulletin of the American Astronomical Society*, volume 41 of *Bulletin of the American Astronomical Society*, pages 336–+, January 2009.

Y.-Y. Zhang, A. Finoguenov, H. Bohringer, JP Kneib, GP Smith, R. Kneissl, N. Okabe, and H. Dahle. Locuss: comparison of observed x-ray and lensing galaxy cluster scaling relations with simulations. *Astronomy and Astrophysics*, 482(2):451–472, 2008.

B.J. Maughan, C. Jones, W. Forman, and L. Van Speybroeck. Images, Structural Properties, and Metal Abundances of Galaxy Clusters Observed with Chandra ACIS-I at 0.1¡z¡1.3. *ApJS*, 174:117–135, January 2008.

K.W. Cavagnolo, M. Donahue, G.M. Voit, and M. Sun. Bandpass Dependence of X-Ray Temperatures in Galaxy Clusters. *The Astrophysical Journal*, 682(2):821–834, 2008.

M. Markevitch, W. R. Forman, C. L. Sarazin, and A. Vikhlinin. The temperature structure of 30 nearby clusters observed with asca: Similarity of temperature profiles. *ApJ*, 503:77, August 1998.

M.R. Calabretta and E.W. Greisen. Representations of celestial coordinates in FITS. *A&A*, 395:1077–1122, December 2002.

M. G. Haehnelt and M. Tegmark. Using the Kinematic Sunyaev-Zeldovich effect to determine the peculiar velocities of clusters of galaxies. *MNRAS*, 279:545+, March 1996.

D. Herranz, J.L. Sanz, R.B. Barreiro, and E. Martínez-González. Scale-adaptive Filters for the Detection/Separation of Compact Sources. *ApJ*, 580:610–625, November 2002a.

D. Herranz, J.L. Sanz, M.P. Hobson, R.B. Barreiro, J.M. Diego, E. Martínez-González, and A.N. Lasenby. Filtering techniques for the detection of Sunyaev-Zel'dovich clusters in multifrequency maps. *MNRAS*, 336:1057–1068, November 2002b.

J.-B. Melin, J.G. Bartlett, and J. Delabrouille. Catalog extraction in SZ cluster surveys: a matched filter approach. *A&A*, 459:341–352, November 2006.

M.R. Nolta, J. Dunkley, R.S. Hill, G. Hinshaw, E. Komatsu, D. Larson, L. Page, D.N. Spergel, C.L. Bennett, B. Gold, N. Jarosik, N. Odegard, J.L. Weiland, E. Wollack, M. Halpern, A. Kogut, M. Limon, S.S. Meyer, G.S. Tucker, and E.L. Wright. Five-Year Wilkinson Microwave Anisotropy Probe Observations: Angular Power Spectra. *ApJS*, 180: 296–305, February 2009.

C. Borys, S. Chapman, M. Halpern, and D. Scott. The Hubble Deep Field North SCUBA Super-map - I. Submillimetre maps, sources and number counts. *MNRAS*, 344:385–398, September 2003.

M. White and S. Majumdar. Point Sources in the Context of Future SZ Surveys. *ApJ*, 602: 565–570, February 2004.

M. Lima, B. Jain, and M. Devlin. Lensing Magnification: Implications for Counts of Submillimeter Galaxies and SZ Clusters. *ArXiv e-prints*, July 2009.

N. Sehgal, P. Bode, S. Das, C. Hernandez-Monteagudo, K. Huffenberger, Y.-T. Lin, J.P. Ostriker, and H. Trac. Simulations of the Microwave Sky. *ArXiv e-prints*, August 2009.

J. Sayers, S.R. Golwala, P. Rossinot, P.A.R. Ade, J.E. Aguirre, J.J. Bock, S.F. Edgington, J. Glenn, A. Goldin, D. Haig, A.E. Lange, G.T. Laurent, P.D. Mauskopf, and H.T. Nguyen. A Search for Cosmic Microwave Background Anisotropies on Arcminute Scales with Bolocam. *ApJ*, 690:1597–1620, January 2009.

G.W. Wilson, D.H. Hughes, I. Aretxaga, H. Ezawa, J.E. Austermann, S. Doyle, D. Ferrusca, I. Hernández-Curiel, R. Kawabe, T. Kitayama, K. Kohno, A. Kuboi, H. Matsuo, P.D. Mauskopf, Y. Murakoshi, A. Montaña, P. Natarajan, T. Oshima, N. Ota, T.A. Perera, J. Rand, K.S. Scott, K. Tanaka, M. Tsuboi, C.C. Williams, N. Yamaguchi, and M.S. Yun. A bright, dust-obscured, millimetre-selected galaxy beyond the Bullet Cluster (1E0657-56). *MNRAS*, 390:1061–1070, November 2008.

M. Arnaud, G.W. Pratt, R. Piffaretti, H. Boehringer, J.H. Croston, and E. Pointecouteau. The universal galaxy cluster pressure profile from a representative sample of nearby systems (REXCESS) and the Y_SZ-M_500 relation. *ArXiv e-prints*, October 2009.

A. Finoguenov, H. Böhringer, and Y.-Y. Zhang. XMM-Newton study of the two-dimensional structure of the REFLEX-DXL galaxy clusters. *A&A*, 442:827–839, November 2005.

L. Grego, J.E. Carlstrom, E.D. Reese, G.P. Holder, W.L. Holzapfel, M.K. Joy, J.J. Mohr, and S. Patel. Galaxy Cluster Gas Mass Fractions from Sunyaev-Zeldovich Effect Measurements: Constraints on Ω_M. *ApJ*, 552:2–14, May 2001.

S.J. LaRoque, M. Bonamente, J.E. Carlstrom, M.K. Joy, D. Nagai, E.D. Reese, and K.S. Dawson. X-Ray and Sunyaev-Zel'dovich Effect Measurements of the Gas Mass Fraction in Galaxy Clusters. *ApJ*, 652:917–936, December 2006.

J.J. Mohr, B. Mathiesen, and A.E. Evrard. Properties of the intracluster medium in an ensemble of nearby galaxy clusters. *ApJ*, 517:627–649, June 1999.

G.W. Pratt, H. Böhringer, J.H. Croston, M. Arnaud, S. Borgani, A. Finoguenov, and R.F. Temple. Temperature profiles of a representative sample of nearby X-ray galaxy clusters. *A&A*, 461:71–80, January 2007.

E.J. Hallman, J.O. Burns, P.M. Motl, and M.L. Norman. The β-Model Problem: The Incompatibility of X-Ray and Sunyaev-Zeldovich Effect Model Fitting for Galaxy Clusters. *ApJ*, 665:911–920, August 2007.

G.L. Bryan and M.L. Norman. Statistical properties of x-ray clusters: Analytic and numerical comparisons. *ApJ*, 495:80, 1998.

A. Vikhlinin, A. Kravtsov, W. Forman, C. Jones, M. Markevitch, S.S. Murray, and L. Van Speybroeck. Chandra Sample of Nearby Relaxed Galaxy Clusters: Mass, Gas Fraction, and Mass-Temperature Relation. *ApJ*, 640:691–709, April 2006.

M. Bonamente, M. Joy, S.J. LaRoque, J.E. Carlstrom, D. Nagai, and D.P. Marrone. Scaling Relations from Sunyaev-Zel'dovich Effect and Chandra X-Ray Measurements of High-Redshift Galaxy Clusters. *ApJ*, 675:106–114, March 2008.

D.P. Marrone, G.P. Smith, J. Richard, M. Joy, M. Bonamente, N. Hasler, V. Hamilton-Morris, J.-P. Kneib, T. Culverhouse, J.E. Carlstrom, C. Greer, D. Hawkins, R. Hennessy, J.W. Lamb, E.M. Leitch, M. Loh, A. Miller, T. Mroczkowski, S. Muchovej, C. Pryke, M.K. Sharp, and D. Woody. LoCuSS: A Comparison of Sunyaev-Zel'dovich Effect and Gravitational-Lensing Measurements of Galaxy Clusters. *ApJ*, 701:L114–L118, August 2009.

A. Mantz, S.W. Allen, H. Ebeling, D. Rapetti, and A. Drlica-Wagner. The Observed Growth of Massive Galaxy Clusters II: X-ray Scaling Relations. *ArXiv e-prints*, September 2009.

Appendix A

Hardware Manager and Fridge Daemon Documentation

The hardware manager and fridge daemons are two of the major components of the receiver control system described in Chapter 6. Both are multithreaded applications written in C++, and both can be run either with or without the presence of the telescope control system. The fridge daemon is the simpler of the two, but both programs are similar in their design and implementation.

A.1 Fridge Daemon

The fridge daemon application runs on the receiver control computer, and communicates with controller hardware originally designed for the ACBAR experiment. It is responsible for operating the sorption fridge and associated housekeeping thermometry. Two PCI boards are required to interface with the controller: an analog-digital converter (ADC), model PCI-DAS6402/16 from Measurement Computing; and a digital input-output (DIO), model PCI-7248 from ADLink.

All of the fridge software is stored in a CVS archive called *fridge*. The required Comedi device interface software[1] is included in the *software* subdirectory of the repository, and a custom DIO driver written by Martin Lueker can be found in the *heater_driver* subdirectory. The low-level fridge hardware access code, much of which was written by former Berkeley undergraduate Billy Mallard, is in the *inc* and *src* subdirectories. The configuration and calibration files are in *info*, and the high-level daemon and scripting code discussed here can be found in *tools*.

Upon startup, the fridge daemon process launches two threads: an *updater* thread and a *listener* thread. The *updater* thread queries the ADC card for thermometry information every n seconds, where $n = 3$ by default[2]. If necessary, it also issues commands over the DIO card to adjust the gains of the GRT readout circuits. The *listener* thread accepts TCP connections on port 57128, and upon receiving a request, launches a *connection* thread

---

[1] `http://www.comedi.org`

[2] The update interval can be changed by overriding the default value of *updatetime* in the FridgeManager constructor; the FridgeManager is a helper object instantiated in the main() function of FridgeDaemon.cpp.

with its own dedicated TCP connection. Many *connection* threads can exist simultaneously. Each of these threads creates a set of commands, which clients can execute by sending an appropriate block of XML over the TCP socket. XML command blocks take the following form:
<Cmd type="container">
<Name type="string"> *command name* </Name>
<*parameter1* type="*parameter1 type*"> *parameter1 value* </*parameter1*>
<*parameter2* type="*parameter2 type*"> *parameter2 value* </*parameter2*>
...
</Cmd>
If *command name* matches the identification string of any of the connection's command objects, then the execute method of that command object called, and is passed a copy of the XML block to be parsed for parameter values.

Three types of hardware resources are handled by the daemon: thermometers, which may be either diodes or germanium resistance thermometers (GRTs); heaters; and gas gap heat switches. The hardware is capable of controlling 12 diode thermometers, four GRT thermometers, and 8 heaters; a switch counts as one diode thermometer and one heater. Each resource has a name associated with it, and the daemon maintains a mapping between the name strings and the physical hardware addresses. This mapping, along with the calibration files for the thermometers, is specified in the *info/FridgeConfig_default.xml* configuration file. In the name strings, we refer to the 3He cold head as the UC (ultra cooler) and the 3He buffer head as the IC (inter cooler). The SPT fridge controller resources are listed in Table A.1. Some heaters and thermometers have the same name, but this does not introduce ambiguity into any of the commands.

It is not expected that users will ever need to interact directly with the fridge daemon, so the XML commands are not enumerated here. Instead, I describe the Python scripting library used to send and interpret the commands. The fridge Python library consists of a class called FridgeClient used for writing scripts and interfaces. A command line interface (*manual_controller.py*) and a curses-based monitoring program (*monitor.py*) are also provided, along with a number of scripts. The command line interface contains an online help mechanism, and the monitoring program is not interactive.

The script *tools/auto_cycle.py*, which runs a complete sorption fridge cycle without pausing for any SQUID or bolometer tuning, is an instructive example of how to use the FridgeClient class. Other useful scripts, including *logger.py*, *bring_uchead_abovetc.py* and *bring_uchead_tobasetemp.py*, can also be found in the *tools* subdirectory of the CVS repository. Note that since the SPT telescope control system handles the data archiving on the telescope, the fridge daemon itself does not store a record of temperatures; in laboratory testing, the *logger.py* script is used to generate flat text log files.

The FridgeClient class provides the following methods:

IsAlive() Pings the daemon to see if it is running.

AllThermos(), AllHeaters(), AllSwitches() Gets lists of the resource names present in the system.

GetTemp(name,raw=False) Get the most recently-read temperature measured by ther-

Table A.1. Hardware resources managed by the SPT fridge controller.

Name	Description	ADC line	DIO line
ICHEAD	3He buffer head GRT	AdcGRT0	DioGRT0
UCHEAD	3He cold head GRT	AdcGRT1	DioGRT1
ICSTAGE	3He buffer stage GRT	AdcGRT2	DioGRT2
UCSTAGE	3He cold stage GRT	AdcGRT3	DioGRT3
UCPUMP	3He cold pump diode	AdcDiode0	
4HEPUMP	4He pump diode	AdcDiode1	
ICSW	3He buffer pump switch diode	AdcDiode2	
DIODEB1	Auxiliary diode	AdcDiode3	
DIODEB2	Auxiliary diode	AdcDiode4	
DIODEB3	Auxiliary diode	AdcDiode5	
ICPUMP	3He buffer pump diode	AdcDiode6	
HEX	Heat exchanger diode	AdcDiode7	
4HESW	4He pump switch diode	AdcDiode8	
DIODEB4	Auxiliary diode	AdcDiode9	
MAINPLATE	Main plate diode	AdcDiode10	
UCSW	3He cold pump switch diode	AdcDiode11	
UCPUMP	3He cold pump heater	AdcHeater0	DioHeater0
ICPUMP	3He buffer pump heater	AdcHeater1	DioHeater2
4HEPUMP	3He buffer pump heater	AdcHeater2	DioHeater1
UCSW	3He cold pump switch heater	AdcHeater3	DioHeater3
ICSW	3He buffer pump switch heater	AdcHeater4	DioHeater4
4HESW	4He pump switch heater	AdcHeater5	DioHeater6
4KHEATER	Main plate heater	AdcHeater6	DioHeater5
STAGEHEATER	3He cold stage heater	AdcHeater7	DioHeater7

mometer *name*. By default, the calibrated temperature in Kelvin is returned. If the *raw* parameter is set to True, the function will instead return the diode voltage in Volts or the GRT resistance in Ohms.

GetHeater(name) and SetHeater(name,value) Get and set the current through heater *name* in milliamps.

GetSwitch(name) and SetSwitch(name,value) Get and set the state of heat switch *name* to conducting (True) or non-conducting (False).

GetExcitation(name) and SetExcitation(name, value) Get and set the excitation level of GRT *name*. The excitation settings (0,1,2,3) correspond to (3 mV, 1 mV, 0.3 mV, 0.1 mV).

SetAutorange(name) Set GRT *name* to automatic ranging. This is the default behavior, but it can be overridden by the SetGain command.

GetGain(name) and SetGain(name,value) Get and set the gain level of GRT *name*. The gain settings (0,1,2,3) correspond to GRT resistance ranges of (1-10 Ω, 10-200 Ω, 200-4000 Ω, 4-80 kΩ). Normally, the software automatically selects the appropriate gain setting; SetGain will override this behavior.

Calibrate() Forces the daemon to re-read the thermometer calibration files specified in *FridgeConfig_default.xml*.

FetchValues() Calls the *GetAllRegisters* XML command used by the SPT control system, and returns the XML response. Useful for debugging only.

FetchDict() Fetches a Python dictionary of values corresponding to the temperatures, heater currents, and so on. Used by the monitoring program.

These methods provide access to all of the fridge controller functionality.

A.2 Hardware Manager Daemon

The hardware manager daemon too is a multi-threaded application, with a *listener* thread to accept TCP connections (on port 5207), and separate *connection* threads for each client. Another thread maintains a queue of commands to be sent to the hardware over the serial connection, issues them in the order in which they were enqueued. Like the fridge daemon, the hardware manager daemon implements a number of low-level commands, a set of which is associated with each *connection* thread. In addition, the hardware manager daemon also has the ability to run certain higher-level algorithms, each of which runs in its own thread. A TCP connection is maintained to the daemon controlling the high-speed DIO card, so that commands and algorithms have the ability to acquire timestream data if necessary.

The source code for the hardware manager and DIO daemons is stored in a CVS repository called *MuxReadoutSoftware*. The *ReadoutHardware* subdirectory in the repository contains the low-level hardware objects and the hardware manager itself, and the code for the algorithms and commands is in the *Algorithms* and *Commands* subdirectories. *MultiThread* and *DIOUtils* contain the DIO daemon and interfaces, which were written by Martin Lueker. *Config* contains files that specify the addressing and configuration of resources within the readout system, as described in Chapter 6. The remaining subdirectories contain various utilities and drivers. Since the readout Python interface is relatively complex, it is broken out into its own CVS repository called *MuxUI*. As before, I will defer discussion of the XML command and algorithm framework in favor of the Python interface.

A number of Python objects are provided by *MuxUI*, most of which inherit from a base *ReadoutObject* base class. This class, along with the *MuxTCPClient* and *CommandFactory* helper classes, handles the XML communication with the daemon over TCP. Each *ReadoutObject* has a readout address (see Chapter 6), a TCP socket, and a client identifier string associated with it; the client identifier is used for resource locking, which is disabled in the SPT version of the fMUX software.

The classes derived from *ReadoutObject* are:

ReadoutSystem This object implements functions and algorithms that can be applied to subsets of the readout system (such as *mnetanal*, which takes a network analysis on many channels in parallel) or to the system as a whole (such as *get_all_registers*). It also includes address resolution methods (such as *get_addr_from_bolo_id*), that scripts can use to figure out which other *ReadoutObject*s to instantiate.

ReadoutBoard This object is used to directly set or get register values on the oscillator-demodulator boards. It can also be used to power up or down any attached SQUID controller boards.

ReadoutChannel This is the most frequently-used object in the *MuxUI* library. It is used to get and set values associated with the bias, signal demodulation, and carrier nulling of the detectors. Short bursts of AC and DC timestream data can be obtained from *ReadoutChannel* objects and used for tuning or monitoring. A few simple algorithms like I-V curves are also implemented as member functions.

SquidChannel Analogous to the correspondence between detectors and *ReadoutChannel* objects, *SquidChannel* objects provide control and monitoring of the SQUID amplifiers. These objects can be used to set or get biases, heater voltages, amplifier offsets, and flux-locked loop states, and so on; member functions also provide access to simple algorithms like V-Phi curves.

ReadoutChannelVec and SquidChannelVec These classes are vectorized versions of the previous two classes, and are used to set or get the same value from several channels in parallel.

Graphical user interface objects are provided for the *ReadoutSystem*, *ReadoutBoard*, *ReadoutChannel*, and *SquidChannel* classes. These objects can be packaged together to create useful control and monitoring interfaces such as *MuxReadoutUI.py*, which are often used in laboratory testing. The graphical user interfaces notwithstanding, most interaction with the readout system takes place via scripts, which can be run from the receiver computer command line or from the telescope control system. Most of these scripts take as an argument a list of readout addresses (defined in Chapter 6). The address parsing is done using a common helper routine, so all scripts understand a variety of shortcuts and wildcards:

- *61:ra1 61:ra2* specifies two readout channels.
- *61:ra* specifies a chain of eight readout channels.
- *61:* specifies all 16 readout channels on board 61.
- *61-64:ra8* specifies channel a8 on four readout boards.
- *61:r?8* specifies channels *61:ra8* and *61:rb8*.
- *-f ChannelList* specifies a file containing a list of channels.

Scripts with significant amounts of input and output store their data in timestamped log directories. If a script is executed from the telescope control system, its output also propagates into the telescope log files via the redirection of the standard output and error streams. Each script ends by writing a status message to standard error in the form
%%%BEGIN_STATUS
SUCCESS *success*
%%%END_STATUS
where *success* is 1 when the script completes successfully, and 0 otherwise. If any errors or messages are to be propagated to the main log file, a similar protocol is used over standard error, with ERROR or MESSAGE in the place of STATUS, and with arbitrary strings in the place of the SUCCESS field. Finally, the standard output stream is redirected to its own log file.

Some useful readout scripts include:

summary.py This often-used script outputs a human-readable summary of a set of readout channels, including oscillator-demodulator parameters and AC and DC output levels.

set_oscdemod_parameter.py This script uses *ReadoutChannelVec* to set oscillator-demodulator parameters for a set of readout channels. The parameters include gain settings, oscillator amplitudes and frequencies, and carrier and nuller potentiometer levels.

set_squidctrl_parameter.py Similarly, this script sets SQUID channel parameters using vectorized commands.

offset_boloiv.py This script takes a bolometer I-V curve for a single channel using an offset channel to measure the current amplitude. The I-V curve can be set to stop at a given potentiometer value or a given fraction of R_n.

tune_squids_parallel.py The SQUID tuning algorithm is executed via this script, and the output is stored in a format that can be examined using *show_tuning.py*.

biasup_bolos.py This script biases a set of bolometers in the normal regime. Exceptions to the default bias levels can be specified on the command line, or in *exceptions* files—tab-separated text files containing lists of readout addresses and their desired amplitude or potentiometer settings.

operate_bolos.py Similarly, this script biases a set of bolometers into their transitions. The transitions are identified by taking bolometer I-V curves in parallel for eight groups of detectors, where each channel is assigned a group based on the last digit of its readout address. The default values can again be overridden on the command line or in *exceptions* files.

netanal.py Network analyses can be taken in parallel using this script.

fix_flux_jumps_cold.py SQUIDs that have jumped to stable but sub-optimal operating points can be recovered using this script.

null_bolos.py and null_fine.py These scripts perform coarse and fine carrier nulling routines on sets of readout channels.

While the existing library of scripts is sufficient to set up and operate the receiver during normal operations, users are encouraged to write their own routines for testing and debugging in the lab. The *operate_bolos.py* script is particularly useful as a model, since it takes advantage of many (if not most) of the readout scripting library features.

Appendix B

Cluster Maps and Profiles

Shown below are the SPT maps and profiles for each of the clusters in this sample. Four maps are shown for each cluster: the 150 GHz map (upper left), the 220 GHz map (upper right), the band subtracted map (lower left), and a jackknife band subtracted map (lower right). The pixel size is $0.25'$, and each map is smoothed with a Gaussian with a full width at half maximum of $1'$. The 220 GHz maps contain more noise than the 150 GHz maps due to lower sensitivity and higher-amplitude atmospheric fluctuations in the 220 GHz band. The band subtracted map is calculated by applying a matched filter to the 220 GHz map and subtracting the result from the 150 GHz map. The jackknife band subtracted map is calculated by multiplying half of the single observation maps by -1 before coadding. The locations of bright point sources that were removed are marked by crosses. The visible structure to the east and west of the brighter clusters is due to the timestream polynomial subtraction (see text), and is accounted for in the radial profiles.

The profiles are computed from the band subtracted maps using our knowledge of the SPT beams and time domain filtering. Each profile point represents the average SZ temperature decrement within a given radial bin. The dashed vertical line is an estimate of the cluster virial radius given by $\sqrt{500/\Delta_c} r_{500}$, where Δ_c is calculated using the approximation in Bryan and Norman [1998]. For the lowest-redshift clusters, this radius is larger than $15'$. The algorithm used to derive the profiles is described in Section 7.3.1.

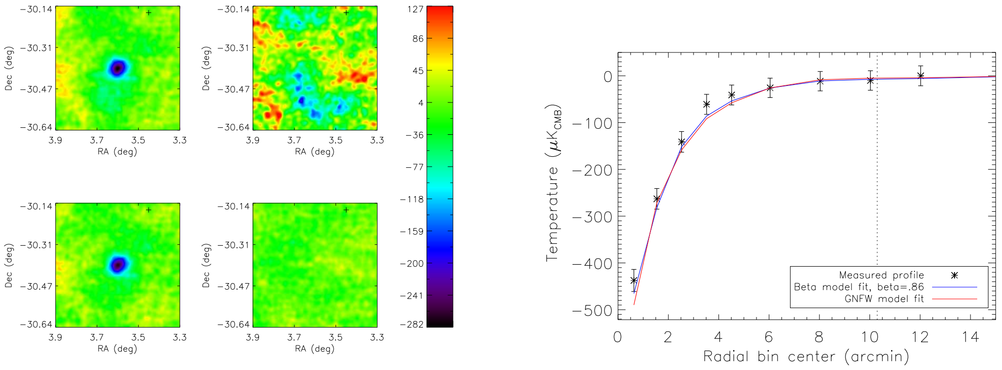

Figure B.1. A 2744 maps (left) and profile (right). The four maps are 150 GHz (upper left), 220 GHz (upper right), band subtracted (lower left), and jackknife (lower right). Units are μK_{CMB}.

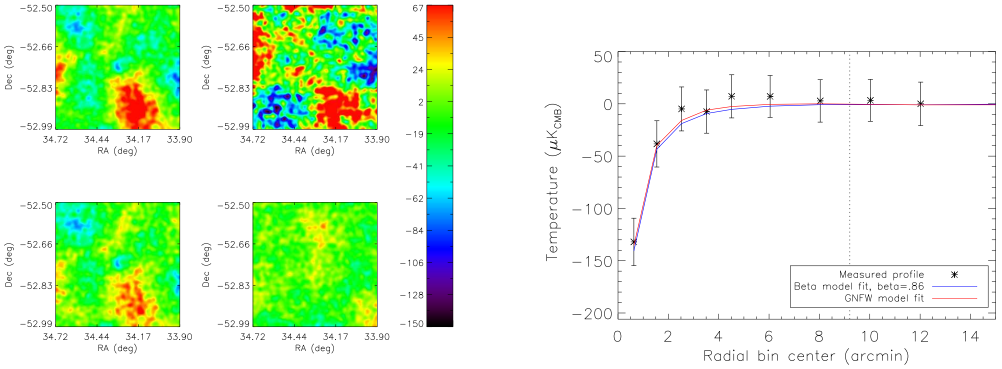

Figure B.2. RXCJ0217.2-5244 maps (left) and profile (right). Units are μK_{CMB}.

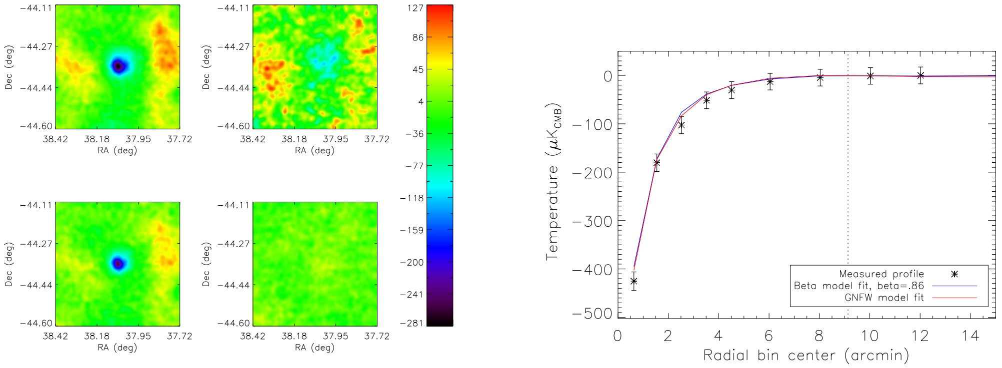

Figure B.3. RXCJ0232.2-4420 maps (left) and profile (right). Units are μK_{CMB}.

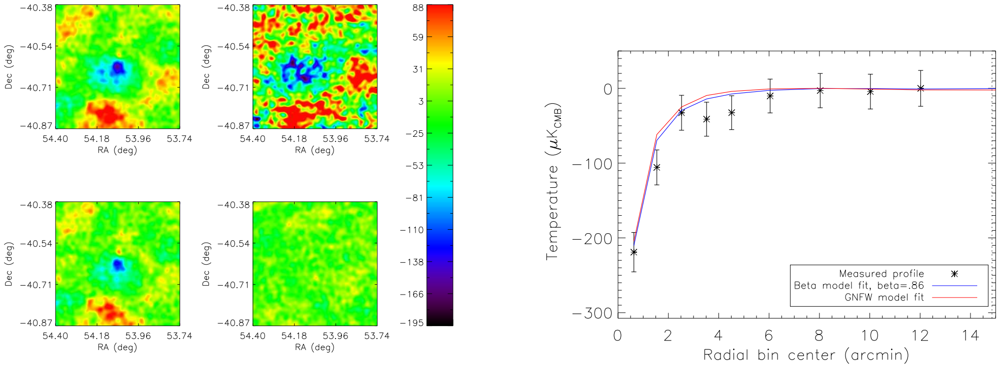

Figure B.4. RXCJ0336.3-4037 maps (left) and profile (right). Units are μK_{CMB}.

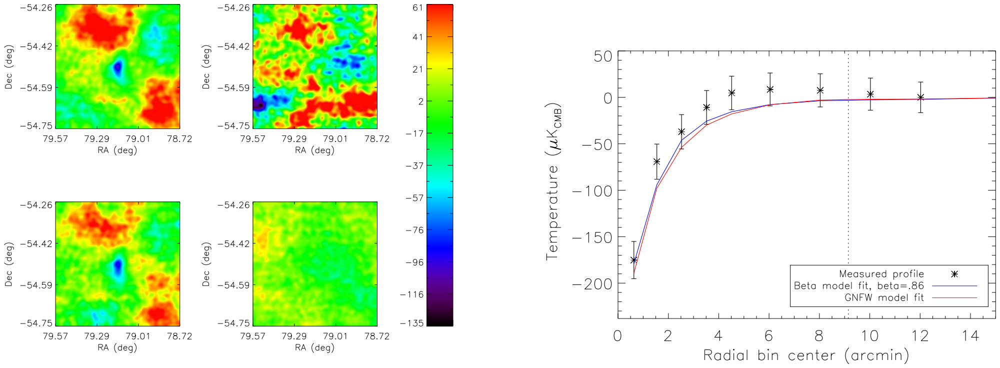

Figure B.5. AS 0520 maps (left) and profile (right). Units are μK_{CMB}.

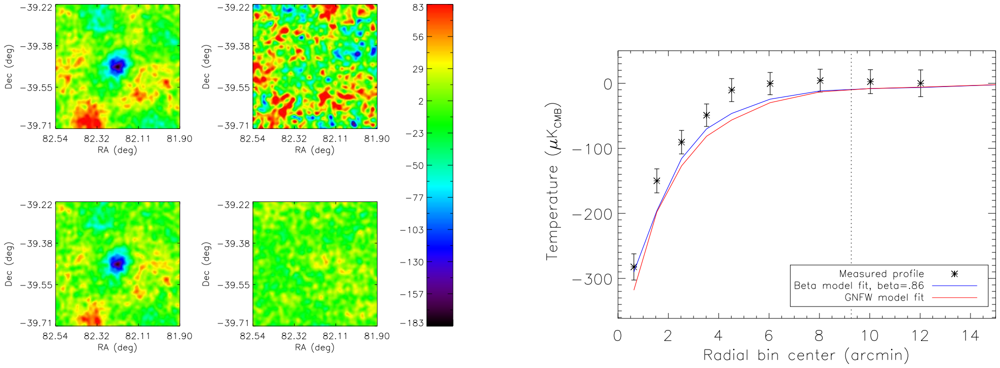

Figure B.6. RXCJ0528.9-3927 maps (left) and profile (right). Units are μK_{CMB}.

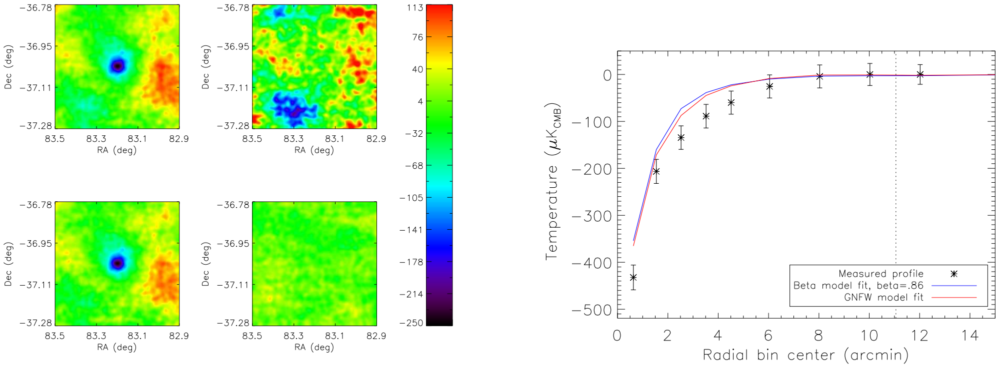

Figure B.7. RXCJ0532.9-3701 maps (left) and profile (right). Units are μK_{CMB}.

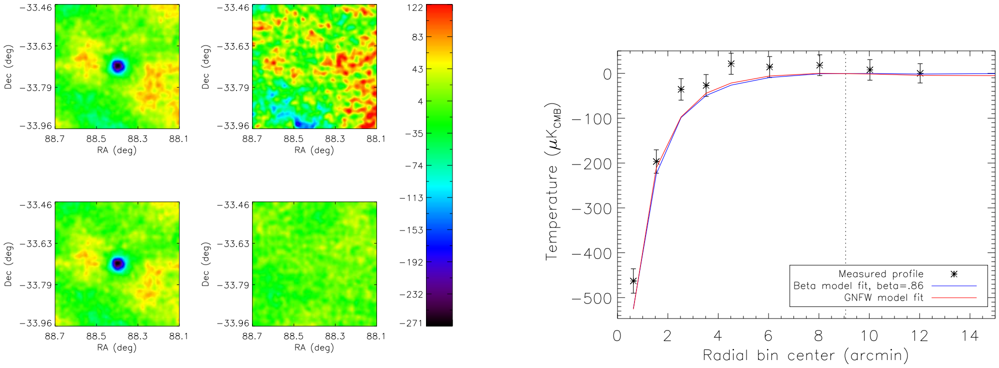

Figure B.8. MACSJ0553.4-3342 maps (left) and profile (right). Units are μK_{CMB}.

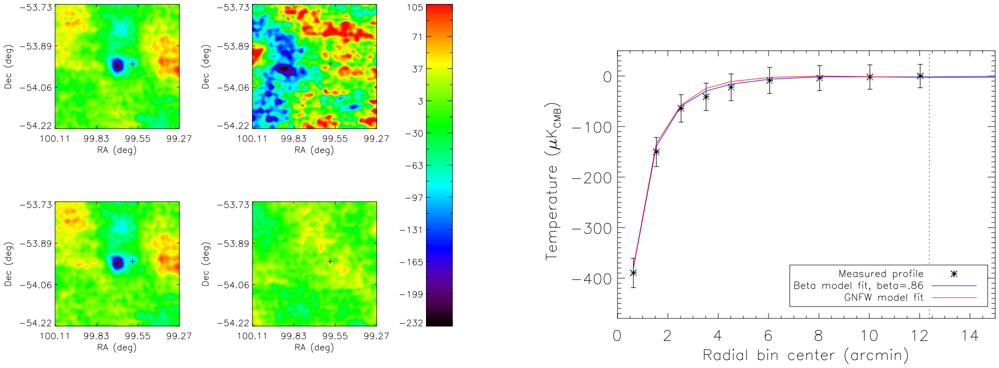

Figure B.9. AS 0592 maps (left) and profile (right). Units are μK_{CMB}.

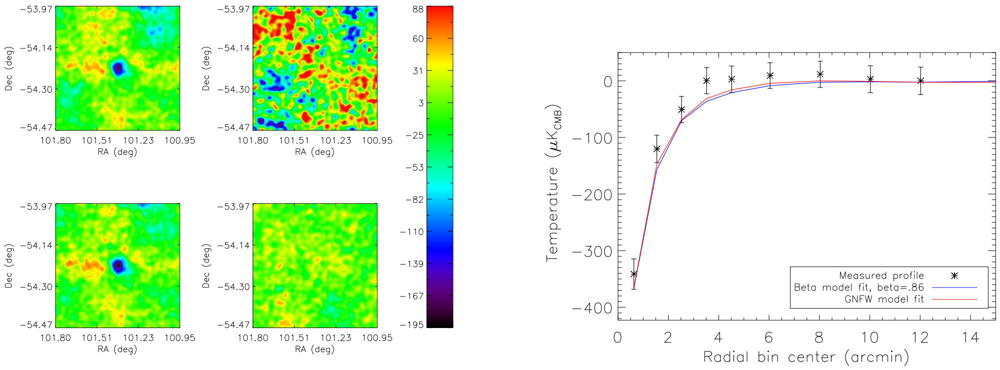

Figure B.10. A 3404 maps (left) and profile (right). Units are $\mu K_{\rm CMB}$.

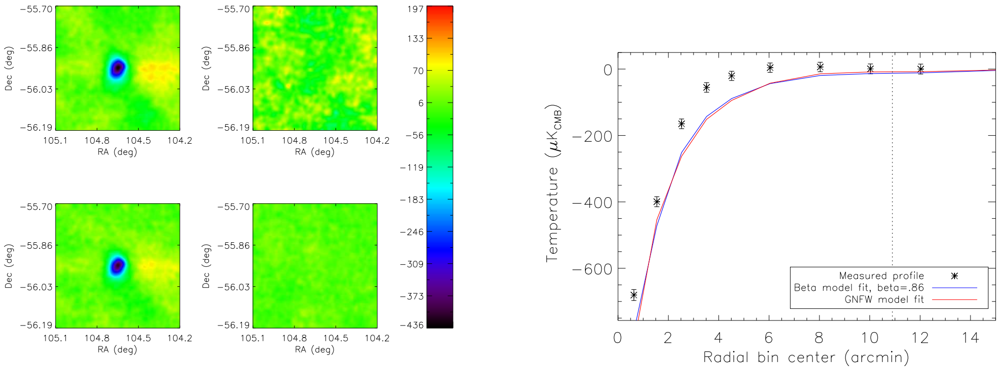

Figure B.11. 1ES 0657-56 maps (left) and profile (right). Units are $\mu K_{\rm CMB}$.

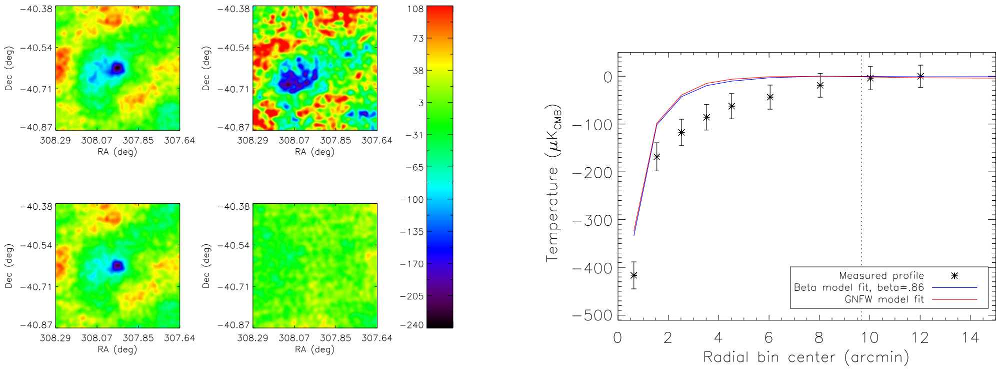

Figure B.12. RXCJ2031.8-4037 maps (left) and profile (right). Units are $\mu K_{\rm CMB}$.

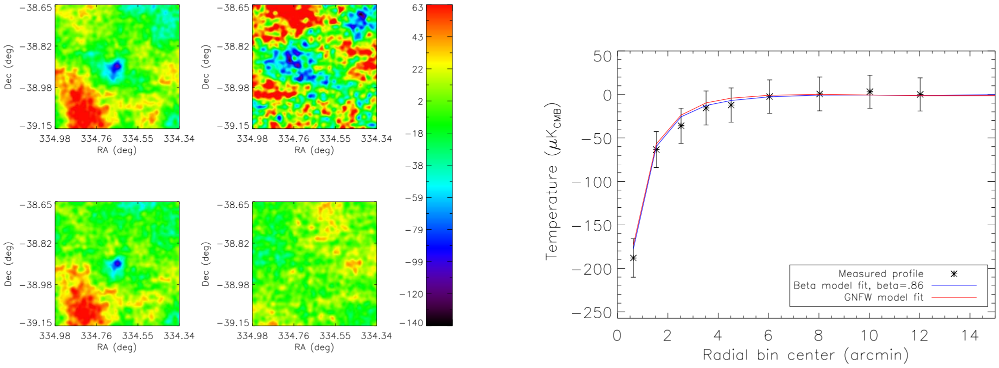

Figure B.13. A 3856 maps (left) and profile (right). Units are μK_{CMB}.

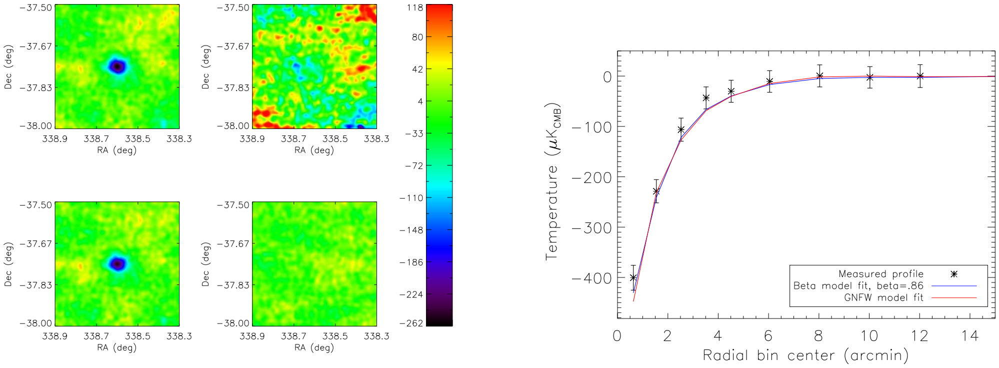

Figure B.14. A 3888 maps (left) and profile (right). Units are μK_{CMB}.

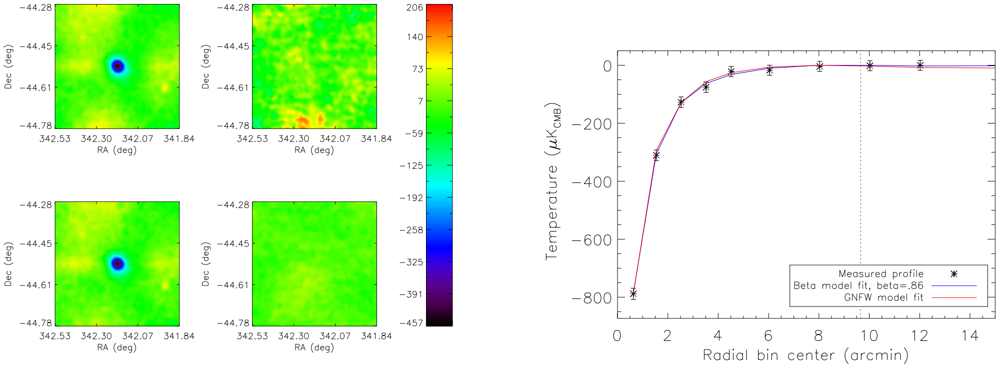

Figure B.15. AS 1063 maps (left) and profile (right). Units are μK_{CMB}.